Check for updates

Strategies of structural and defect engineering for high-performance rechargeable aqueous zinc-ion batteries

Min Du,†[a] Zhenyu Miao,†[a] Houzhen Li,[a] Yuanhua Sang, [iD][a] Hong Liu [iD]*[ab] and Shuhua Wang [iD]*[a]

Aqueous zinc-ion batteries (ZIBs) have been increasingly studied in recent years due to their low cost and high safety and the high abundance of natural zinc resources. However, the practical application of ZIBs has been restricted due to some challenges, including the low electrochemical activity of their cathodes, sluggish diffusion kinetics of Zn^{2+}, structural instability during long-term cycling, formation of dendrites and occurrence of side reactions on zinc anodes. Structural and defect engineering has been developed to address these challenges. Herein, recent progress regarding the structural and defect engineering of aqueous ZIBs is summarized, mainly focusing on introducing interlayer ions/molecules and vacancies/defects into the cathode crystal structure, designing amorphous structures and/or heterostructures of cathodes, decorating an inorganic/organic coating on cathodes, creating an artificial interfacial layer on anodes and constructing nanostructured anodes. Additionally, advanced techniques in structural and defect engineering that are used for aqueous ZIBs are further summarized. Furthermore, the existing challenges and future prospects of the structural and defect engineering of ZIBs are discussed.

1. Introduction

In response to the current energy and environmental crises, the demand for new green energy sources, such as solar energy, geothermal energy, wind energy, and other renewable energy sources, is increasing.[1–5] Currently, renewable energy is generally transported and stored in the form of electricity.[6] Therefore, the development of reliable and stable power conversion and energy storage technologies is critical to enable the efficient use of renewable energy.[7–9] Batteries, which are energy storage devices that convert chemical energy into electrical energy, have been increasingly studied and have undergone several developments since their invention.[10,11] Currently, lithium-ion batteries (LIBs) are widely used as commercial batteries, and their high energy density (150–265 W h kg^{-1}; 400–770 W h L^{-1}) and long cycle life have become a research topic in the international energy storage field in recent years.[12,13] Nevertheless, the development of LIB technology is constrained

[a]*State Key Laboratory of Crystal Materials, Shandong University, Jinan 250100, P. R. China. E-mail: hongliu@sdu.edu.cn; wangshuhua2019@sdu.edu.cn*

[b]*Institute for Advanced Interdisciplinary Research (iAIR), University of Jinan, Jinan, 250022, PR China*

† These authors contributed equally.

Min Du obtained his B.S. degree from Qingdao University in China in 2017. She has been a Ph.D candidate in Prof. Hong Liu's group at the State Key Laboratory of Crystal Materials, Shandong University, China since September 2017. Her research interests are aqueous zinc batteries.

Zhenyu Miao has been a doctoral student in Prof. Hong Liu's group at the State Key Laboratory of Crystal Materials, Shandong University, China since September 2017. His research interests are anode materials for aqueous zinc batteries.

This journal is © The Royal Society of Chemistry 2021

J. Mater. Chem. A, 2021, **9**, 19245–19281 | **19245**

by potential safety hazards due to the flammable nature of their liquid electrolytes and the economic challenges of obtaining the scarce resources that are required.[14,15] In this era of the emergence of a "smart society", there is an urgent need for rechargeable secondary batteries with high energy density, low cost, good cycling performance, safety and environmental friendliness.

Aqueous rechargeable batteries based on multivalent metal cations such as zinc,[16] aluminum,[17] and magnesium ions[18] have attracted considerable attention owing to their environmental friendliness, low cost, high safety, and high energy density. Among them, aqueous zinc ion batteries (ZIBs), consisting of cathode materials, separators, zinc anodes and electrolytes, are considered ideal green battery systems. When ZIBs are in operation, zinc ions transfer in an insertion/extraction mechanism on the cathode, while relevant zinc deposition/stripping occurs on the anode.[19] Owing to the two-electron transfer in the redox reaction, ZIBs can provide high capacity and energy density.[20] In addition, mild or slightly acidic aqueous electrolytes are less harmful to the human body and environment. However, many critical issues remain to be resolved. First, the poor intrinsic electrical conductivity of the cathode material limits electron and charge transport during the redox reaction.[21] A higher electrical conductivity will certainly endow the cathode with superior reaction kinetics. Second, divalent zinc ions have strong electrostatic interactions with the cathode material, which limits the diffusion of zinc ions and its reversibility.[22] Third, most cathode materials, such as vanadium-based materials (VO_2[23] and V_2O_5 (ref. 24)) and manganese-based materials[25] (Mn_2O_3 and MnO_2), usually inevitably dissolve in the electrolyte, potentially resulting in irreversible capacity loss and decreased stability. Additionally, poor stability arises from the phase transition of the cathode during cycling, which results in a large volumetric change and structural collapse.[26] Apart from the challenges associated with cathodes, the zinc anode suffers from the growth of Zn dendrites and side reactions.[7,9] Owing to the irregular electric field and "tip effect", Zn ions spontaneously diffuse and accumulate at preferential nucleation sites and form dendrites on the anode side, leading to ZIBs experiencing internal shorting failure. Moreover, due to the influence of active water molecules, side reactions including hydrogen evolution and Zn corrosion take place on the surface of the anode, leading to ZIBs demonstrating unsatisfactory stability and poor reversibility.[14]

Houzhen Li has been a master's student in Prof. Hong Liu's group at the State Key Laboratory of Crystal Materials, Shandong University, China since September 2020. His research interests are lithium metal anode batteries.

Prof. Dr Hong Liu is a professor at the State Key Laboratory of Crystal Materials, Shandong University. He received his Ph.D degree in 2001 from Shandong University (China). His current research is mainly focused on the chemical processing of nanomaterials for energy related applications including photocatalysis and tissue engineering, especially the interaction between stem cells and the nanostructure of biomaterials, as well as nonlinear optical crystals.

Prof. Dr Yuanhua Sang obtained his B.S. degree from Shandong University in China in 2007 and received his Ph.D degree from Shandong University in July 2012. Now, he works as an associate professor at the State Key Laboratory of Crystal Materials, Shandong University, China. His research interests are the structure and property investigation of inorganic crystal materials with neutron and X-ray diffraction, functional materials, and nano-materials for solar light conversion, especially for photocatalysis and photo-thermal applications.

Prof. Dr Shuhua Wang is a professor at the State Key Laboratory of Crystal Materials, Shandong University. She received her Ph.D degree in 2016 from the Beijing Institute of Nanoenergy and Nanosystems, Chinese Academy of Sciences. Her current research is mainly focused on rechargeable batteries, nanogenerators, and the application of nano-materials in regulating the fate of stem cells and/or immune cells.

19246 | *J. Mater. Chem. A*, 2021, **9**, 19245–19281

This journal is © The Royal Society of Chemistry 2021

Based on the above observations, extensive efforts have been made to alleviate these problems, and considerable advancements have been made. Structural and defect engineering has been recognized as an effective strategy and has been widely adopted in the realm of ZIBs. Recently, some excellent reviews have been reported on aqueous zinc-ion batteries from different perspectives,[27–29] but a comprehensive review of structural and defect engineering for aqueous zinc-ion batteries has not yet been systematically reported. Hence, this study fills the above gap by focusing on the structural and defect engineering of high-performance rechargeable aqueous ZIBs. We first introduce the intercalation of ions and/or molecules in cathode materials and describe the function of ions and/or molecules in the crystal structure or interlayer. Then, the strategies and effects of defect engineering are discussed. Third, recent progress in structural and defect engineering for cathode materials, including amorphous structures, heterostructures, and surface coatings, is systematically summarized. Next, we summarize and discuss concerns about the Zn anode, including the formation of Zn dendrites and water-induced side reactions (hydrogen evolution and Zn metal corrosion). Then from a structural engineering point of view, we proposed possible solutions. In addition, some advanced characterization techniques used for the investigation of ZIBs are summarized. Finally, we propose our perspectives on new directions for the structural and defect engineering of zinc anodes, which may lead to the future development of high-performance aqueous ZIBs.

2. Structural and defect engineering of cathode materials

Although various kinds of materials have been reported as cathodes for aqueous ZIBs, their sluggish kinetics, poor electronic conductivity, structural collapse, and dissolution restrict the further development of ZIBs.[30,31] Thus, a suitable design of the cathode material is crucial for improving the electrochemical performance of aqueous ZIBs. In this section, structural and defect engineering strategies to modulate the properties of cathode materials and improve their performance are presented in detail.

2.1 Ion/molecule intercalation

The introduction of interlayer ions (e.g., Li^+, Na^+, K^+, Mg^{2+}, Ca^{2+}, Ba^{2+}, Zn^{2+}, Fe^{2+}, Cu^{2+}, Mn^{2+}, Al^{3+}, Ag^+, La^{3+}, NH_4^+, and $N(CH_3)_4^+$) can effectively tune the crystal structure of cathode materials,[32–44] which is beneficial for promoting zinc ion diffusion during the discharge–charge process. In addition, the introduced ions can act as pillars to prevent the collapse of the layered structure after Zn^{2+} (de)intercalation, thereby improving the stability of the cathode during long-term cycling.[45] The reported preintercalated metal ions are summarized in a periodic table (Fig. 1a). Molecules have also been introduced into layered cathode materials. For example, structural water molecules have been verified to play a key role in weakening electrostatic interactions with the oxide framework, thus facilitating the

reaction kinetics during the electrochemical process.[46,47] Additionally, organic molecules have been demonstrated to reduce electrostatic interactions between zinc ions and oxides, enhancing the reversibility of Zn^{2+} (de)intercalation.[48,49]

2.1.1 Introduction of single ions. Intercalated divalent zinc ions usually exhibit stronger electrostatic interactions with the host framework than monovalent Li^+ ions,[50,51] which hinders reversible zinc ion insertion/extraction and causes capacity fading. The preintroduction of ions has proven to be a positive strategy to solve the capacity fading problem of V-based cathodes during long-term cycling.[52] The capacity retention could be improved by the pinning effect from the introduced metal ions, as the pillars stabilize the layered structure.[53] The strong bonding between preintercalated metal ions and guest ions effectively prevents structural collapse during repeated Zn^{2+}-ion (de)intercalation storage.[36] For instance, V_3O_8 layers with sodium ions ($NaV_3O_8 \cdot 1.5H_2O$, NVO) as the cathode for aqueous ZIBs were reported to exhibit a capacity retention of 82% over 1000 cycles and the mass loading was 2 mg cm^{-2}.[54] The preintroduced sodium ions in the interlayers of NVO work as pillars to stabilize the crystal structure and prevent structural collapse upon zinc ion insertion/extraction. Divalent ions possess stronger ionic bonding with oxygen atoms in the VO framework than alkali metal ions,[36] contributing to its superior structural durability. Nazar's group investigated $Zn_{0.25}V_2O_5 \cdot nH_2O$ (ZVO) as a cathode for ZIBs,[38] in which the V_2O_5 layers were pinned by ZnO_6 octahedra, as shown in Fig. 1b. Zinc ions act as pillars in the interlayers of ZVO, which are conducive to stabilizing the crystal structure during cycling, thereby causing a reversible phase transformation process and reversible Zn^{2+} insertion/extraction. Similarly, divalent calcium ions were also introduced into the V_2O_5 layers ($Ca_{0.25}V_2O_5 \cdot nH_2O$, CVO) as the cathode for aqueous ZIBs.[36] The Ca–O bonds (2.38–2.57 Å) are much longer than the Zn–O bonds (2.03–2.13 Å); thus, CVO exhibits a larger interlayer spacing than ZVO (Fig. 1c). Besides, compared with the chemical bonding of Zn–O (284.1 kJ mol^{-1}),[55] Ca atoms are deemed to possess larger chemical bonds with O atoms (464 kJ mol^{-1}); thus, Ca can serve as much stronger "pillars" between the VO layers to improve the structural stability of the cathode material for reversible Zn^{2+} migration. Given the superior pinning effect, a small number of calcium ions have been reported to stabilize the V_2O_5 framework *via* a simple chemical pre-intercalation,[56] demonstrating that the capacity does not decay even after 3000 cycles at 10 A g^{-1}. Apart from the aforementioned metal ions, other metal ions such as K^+, Ag^+, Mn^{2+}, Co^{2+}, and Ba^{2+} have also been reported to work as pillars between two VO layers,[34,37,43,57,58] preventing the crystal structure from being damaged. NH_4^+ ions have also been preintercalated into vanadium oxide to stabilize the layered framework during cycling because of its pillaring effect.[59]

This strategy is also suitable for manganese oxide cathodes. To date, (α-, β-, γ-, ε-, and δ-) MnO_2, Mn_2O_3, and Mn_3O_4 have been used as cathodes for aqueous ZIBs.[60–62] However, manganese oxides undergo structural transformation and collapse during cycling, resulting in poor stability.[63,64] Preintercalated metal ions can effectively solve the above problem by acting as
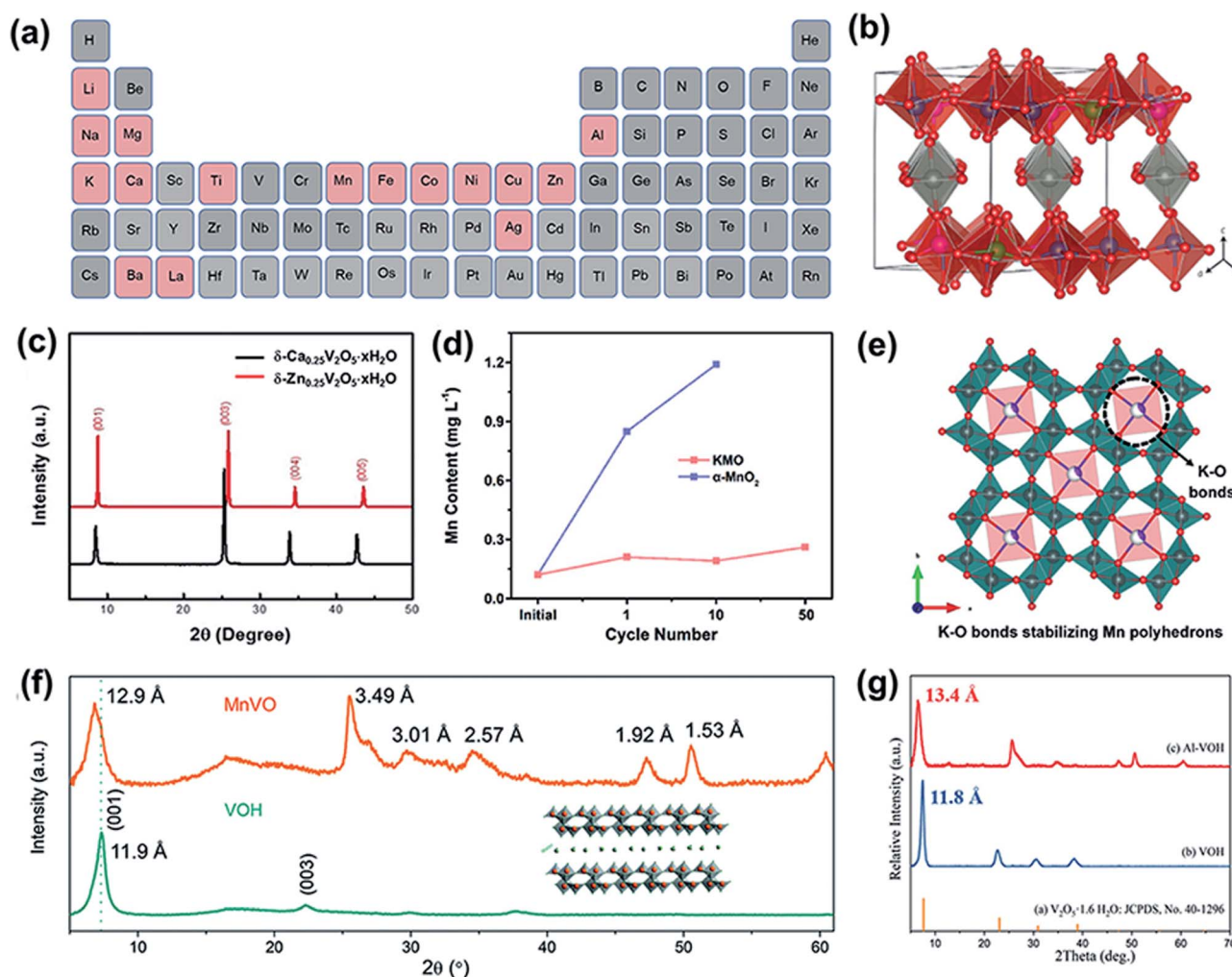
This journal is © The Royal Society of Chemistry 2021

J. Mater. Chem. A, 2021, **9**, 19245–19281 | **19247**

Fig. 1   (a) Periodic table of cations (marked with pink color) that have been introduced into cathode materials. (b) Crystal structure of $Zn_{0.25}$-$V_2O_5 \cdot nH_2O$. Reproduced with permission.[38] Copyright 2016, Springer Nature. (c) XRD pattern of $Ca_{0.25}V_2O_5 \cdot nH_2O$. Reproduced with permission.[36] Copyright 2018, Wiley-VCH. (d) Element content of dissolved Mn^{2+} in a 2 M $ZnSO_4$ aqueous electrolyte during the cycling of KMO and α-MnO_2. (e) Schematic of the incorporation of K^+ ions stabilizing the Mn polyhedrons. (d and e) Reproduced with permission.[68] Copyright 2019, Wiley-VCH. (f) XRD patterns of MnVO and VOH. Reproduced with permission.[69] Copyright 2019, Royal Society of Chemistry. (g) XRD patterns of Al–VOH and VOH. Reproduced with permission.[40] Copyright 2020, Elsevier.

pillars that stabilize the framework. For example, a layered framework of MnO_2 nanospheres with zinc-ion pillars as the cathode for ZIBs was prepared *via* a facile chemical reaction,[65] which exhibited a high capacity of 124 mA h g^{-1} at a current density of 3 A g^{-1} and an outstandingly long lifespan of over 2000 cycles. Similarly, Ca ions were also verified to stabilize layered δ-MnO_2 ($Ca_{0.28}MnO_2 \cdot 0.5H_2O$).[66] Benefiting from the pinning effect of Ca^{2+} ions, the structural stability was strengthened. Thus, the cathode delivered a much higher capacity of 135 mA h g^{-1} at 1.5 A g^{-1} after 300 cycles than the δ-MnO_2 cathode (54.9 mA h g^{-1}) and manifested a significantly long cycle life of over 5000 cycles. Cu^{2+}-intercalated layered MnO_2 also exhibited long-term cycling stability for over 6000 cycles.[67] The high reversibility and durability of the cathode during cycling can be ascribed to the redox reaction of the intercalated Cu^{2+}. Cu^{2+} was reduced to Cu during the discharge process, which decreased the charge transfer resistance (R_{ct})

during the redox reaction and ensured that δ-MnO_2 underwent a reversible phase transition from the dissolved state ($Mn(OH)_2$) to the initial state upon charging. In addition, preintercalated metal ions (K^+) were also deemed to play a critical role in alleviating manganese dissolution and preventing structural degradation.[68] Liang and coworkers found that the dissolution of Mn in Mn_8O_{16} incorporated with K^+ ions was effectively suppressed even after 50 cycles (Fig. 1d). As shown in Fig. 1e, the intercalated K^+ ions bonded with oxygen atoms in the MnO_6 polyhedrons, which strengthened the stability of the tunnel structure and suppressed Mn dissolution.

In addition to the pinning effect, the inserted metal ions could also enlarge the interlayer spacing of V-based oxides, providing more active sites for zinc ion storage. Because of the (de)intercalation-type storage mechanism of ZIBs, an abundance of zinc-ion storage spaces is a crucial factor for endowing active materials with excellent electrochemical performance.

19248 | *J. Mater. Chem. A*, 2021, 9, 19245–19281

This journal is © The Royal Society of Chemistry 2021

Moreover, an expanded interlayer distance reduces the strong interaction between the intercalated Zn^{2+} ions and host materials, thereby promoting zinc-ion diffusion. For example, Li^+ was intercalated into the interlayer of $V_2O_5 \cdot nH_2O$ (LVO-250),[32] increasing the d-spacing of (001) from 12.00 to 13.77 Å. The expanded lattice spacing was conducive to Zn^{2+} insertion and extraction, facilitating Zn^{2+} diffusion and enhancing structural stability. Thus, the LVO-250 cathode delivered a high capacity of 192 mA h g^{-1} at 10 A g^{-1} after 1000 cycles, while the cathode without Li^+ intercalation exhibited inferior long-term cycling performance. Preinserted Mn^{2+} in hydrated vanadium pentoxide (MnVO) expands its lattice spacing.[69] Hydrated vanadium pentoxide has an interlayer spacing of 11.9 Å (Fig. 1f), which enlarges to 12.9 Å after introducing Mn^{2+}. Similarly, the X-ray diffraction (XRD) peaks of $V_2O_5 \cdot nH_2O$ preinserted with Al^{3+} (Al–VOH) also shifted toward a lower degree (Fig. 1g),[40] suggesting the expansion of the interlayer spacing, which was calculated to be 13.4 Å. Although Al^{3+} and Mn^{2+} have similar ionic radii of 53.5 and 58 pm, respectively, the interlayer spacing of Al–VOH is much larger than that of MnVO. This can be ascribed to Al^{3+} exhibiting a higher valence than Mn^{2+}; thus, Al^{3+} exhibits stronger electrostatic repulsion with V^{5+} in the VO framework. Benefiting from the widened interlayer spacing, Al–VOH delivers an obviously enhanced durability without any capacity fading during long term cycling for over 3000 cycles at 4 A g^{-1}. In addition, the interlayer spacing was enlarged by 5.68 Å after the preintercalation of Cu^{2+} ions into the interlayer of V_2O_5 (CuVO-300).[39] The zinc ion diffusion coefficient of CuVO-300 was demonstrated to increase by one order of magnitude compared to that of VO-300. Apart from Cu^{2+}, other transition metal ion (Fe^{2+}, Co^{2+}, Ni^{2+}, Mn^{2+}, and Zn^{2+}) intercalated V_2O_5 delivered higher zinc-ion diffusion coefficients than VO-300. The enhanced electrochemical performance of the cathode with intercalated metal ions was related to the enlarged interlayer spacing, which promoted ion migration during the zinc ion storage process.

The introduced metal ions also increase the electrical conductivity of the electrode to sufficiently improve electrochemical performance. For example, compared with $Zn_{0.25}V_2O_5 \cdot nH_2O$,[38] Ca^{2+}-inserted V_2O_5 ($Ca_{0.24}V_2O_5 \cdot 0.83H_2O$) exhibited a fourfold higher electrical conductivity,[36] which is conducive to electron transfer in electrochemical reactions and improves electrochemical performance. Transition metal ions have also been reported to optimize the electrochemical energy storage of cathodes for ZIBs, mainly because of their unique electronic structures. As shown in Fig. 2a and b, the calculated band structure shows that the indirect bandgap of V_2O_5 doped with Mn^{2+} ions is 0.90 eV,[57] which is smaller than that of pure V_2O_5 (2.28 eV). This bandgap can boost the transfer of charge carriers to the conduction band and improve conductivity. The calculated projected density of states (PDOS) verified that the major 3d orbitals of vanadium and the minor 2(s + p) state of oxygen contribute together to the conduction and valence bands. In particular, a new energy level appears near the Fermi level after the introduction of Mn, which leads to a 40% decrease in the bandgap. Moreover, the charge distribution of layered V_2O_5 after Mn^{2+} intercalation was tuned, as shown in Fig. 2c.

Specifically, electrons accumulated in the yellow region and depleted in the blue region. Thus, the electronic conductivity of layered V_2O_5 was significantly improved after doping with Mn^{2+}. In addition, a multivalence cobalt-doped Mn_3O_4 (Co–Mn_3O_4) cathode has been reported for high-performance ZIBs,[70] and the different chemical states of doped cobalt ions play different roles. Co^{2+} doping into the interlayer of [MnO_6] octahedra acts as a pillar to strengthen the layered structure of δ-MnO_2. The Co^{4+} ions located on the layers enhance the conductivity of Mn^{4+} in the [MnO_6] octahedron. The calculated exfoliation energies (E_{ads}) show that the doped Co^{2+} on δ-MnO_2 has a larger E_{ads} (1.28 eV) than the typical δ-MnO_2 (0.19 eV), suggesting that the stability of the layered structure is strengthened after doping with Co^{2+}. As shown in Fig. 2d, the density of states (DOS) results reveal that δ-MnO_2 doped Co^{4+} shows a band gap of 1.04 eV, which is smaller than that of δ-MnO_2 (1.16 eV). This result is related to the lower energy band gap of the layer-doped Co^{4+}, which improves the conductivity. More importantly, the doped Co ions (Co^{2+} and Co^{3+}) can effectively inhibit the Jahn–Teller effect of the discharge products. The Mn^{3+} derived from species ($ZnMnO_x$ or MnOOH) generated in the discharge state led to Mn(III) dissolution in the aqueous electrolyte. The crystal orbital Hamilton population (COHP) value of the MnOOH-doped Co ions (Co^{2+} and Co^{3+}) is higher than that of MnOOH (Fig. 2e). That is, the bonding state increased, and the anti-bonding state decreased. Thus, the dissolution of Mn ions was effectively alleviated and the stability of the layered structure was enhanced.

Other interesting advancements have been reported after doping with metal ions in host materials. For instance, the voltage of the host cathode is improved after doping guest ions. Zhi's group found that cobalt ion-doped V_2O_5 ($Co_{0.247}V_2O_5 \cdot 0.944H_2O$) as a cathode for ZIBs delivered a higher operational voltage of 1.7 V than that of the $Zn/V_2O_5 \cdot nH_2O$ battery (lower than 1 V).[58] On the one hand, the increased voltage was caused by the unique electronic structure of $Co_{0.247}V_2O_5 \cdot 0.944H_2O$. The interaction between the Co 3d and V 3d orbitals shifted the redox potential of V^{5+}/V^{4+} to a higher level based on electronic structure analyses (Fig. 2f), thus increasing the operational voltage of the cathode. On the other hand, the high voltage is related to the increased absorption energy of Zn^{2+}. As displayed in Fig. 2g and h, the adsorption energy for the Zn atom in $V_2O_5 \cdot nH_2O$ is 1.85 eV, which increases to 2.24 eV after doping with cobalt ions. Besides, the diffusion energy barrier significantly decreases from 0.58 eV to 0.15 eV after preintercalating Co ions into V_2O_5 (Fig. 2i), suggesting that $Co_{0.247}V_2O_5 \cdot 0.944H_2O$ is more suitable for fast Zn-ion diffusion. Thus, Co-doped V_2O_5 exhibits a capacity of 432 mA h g^{-1} at 0.1 A g^{-1} and the capacity above 1.0 V is 227 mA h g^{-1} (52.54% of its total capacity). In contrast, the capacity of the Zn/vanadium oxide system above 1.0 V is usually less than 19% of the total capacity, which is less than 70 mA h g^{-1}. Apart from providing a high voltage, it has also been reported that the guest ions participate in the electrochemical reaction to boost the capacity of the cathode. For example, the redox reaction between Co^{3+} and Co^{4+} in cobalt-ion-doped Mn_3O_4 can contribute to additional capacity.[70] Thus, the multiple electrochemical reactions for Zn
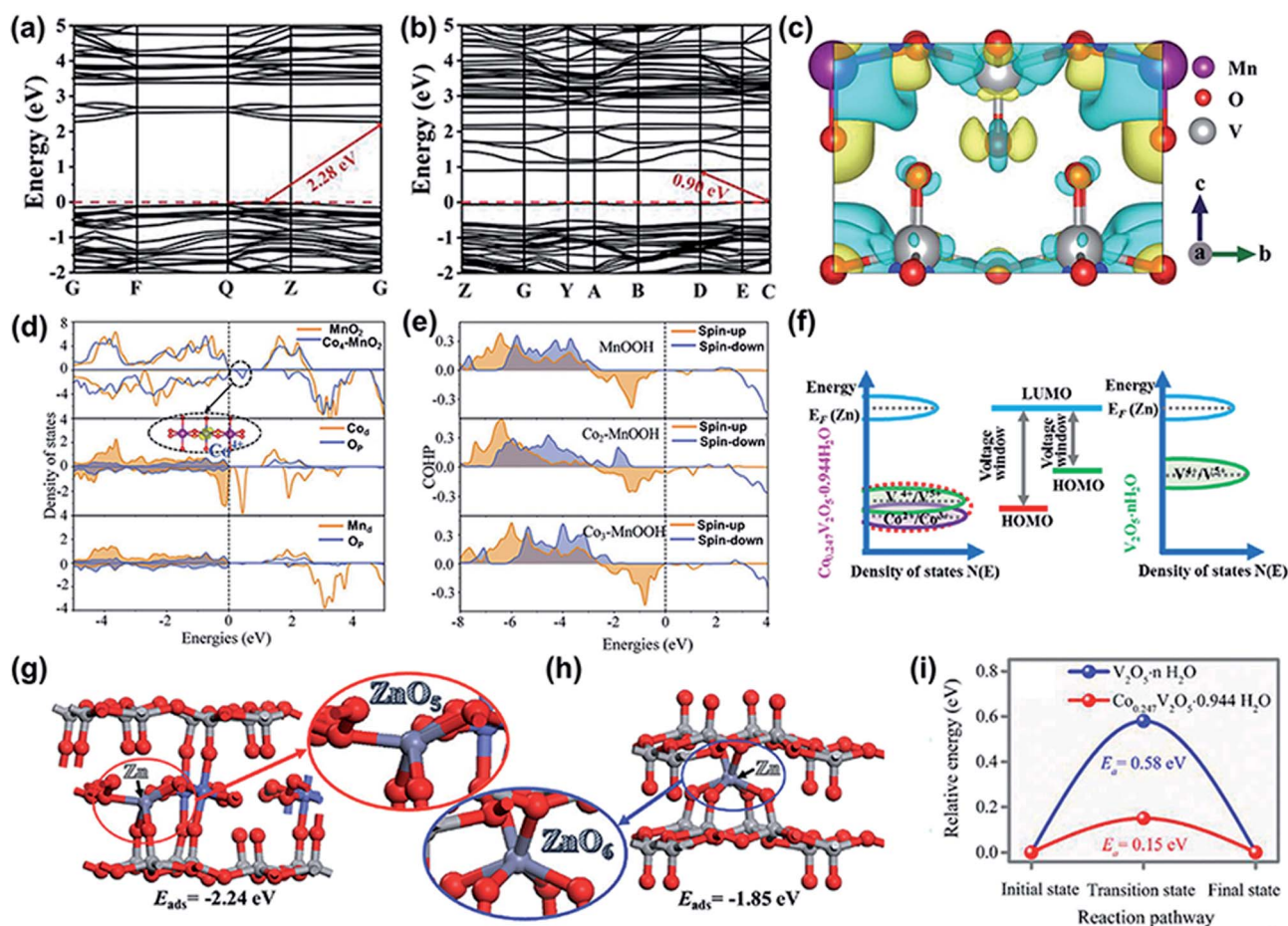
Fig. 2 (a and b) Calculated total band structures and electron density difference of pure V_2O_5 and Mn^{2+}-doped V_2O_5. (c) Electron density difference of Mn^{2+}-doped V_2O_5. (a–c) Reproduced with permission.[57] Copyright 2019, Wiley-VCH. (d) DOS of MnO_2 and $Co^{4+}-\delta$-MnO_2. (e) COHP of MnO_6 (the c-axis) at different positions of MnOOH. (d and e) Reproduced with permission.[70] Copyright 2020, Wiley-VCH. (f) Schematic illustration of the energy $versus$ DOS in $Co_{0.247}V_2O_5\cdot0.944H_2O$ and $V_2O_5\cdot nH_2O$ cathodes. (g and h) The optimized configuration of Zn-adsorbed $Co_{0.247}V_2O_5\cdot0.944H_2O$ and $V_2O_5\cdot nH_2O$ frameworks, respectively, and their corresponding adsorption energies. The gray spheres represent adsorbed Zn atoms, and Co atoms are depicted as blue spheres. (i) The diffusion energy barrier profiles of $Co_{0.247}V_2O_5\cdot0.944H_2O$ and $V_2O_5\cdot nH_2O$. (f-i) Reproduced with permission.[58] Copyright 2019, Wiley-VCH.

ion storage endow the cathode with a high capacity. A novel layered iron vanadate ($Fe_5V_{15}O_{39}(OH)_9\cdot9H_2O$) cathode was prepared as for aqueous ZIBs,[71] in which Fe and V were both subjected to oxidation–reduction reactions during the zinc-ion storage process and contributed to a high capacity of 385 mA h g^{-1} at 0.1 A g^{-1}.

2.1.2 Introduction of single molecules. As a high-performance cathode material for aqueous ZIBs, it is generally believed that the crystal water in the cathode framework significantly affects its electrochemical performance. Specifically, crystal water plays a crucial role in facilitating zinc-ion migration, mainly owing to its "water-lubricating" effect and enlarged interlayer spacing (Fig. 3a).[47] Structural water acting as a charge screening medium reduces the effective charge of H$_2$O-solvated zinc ions and effectively weakens the electrostatic interactions between intercalated Zn^{2+} and the active species. Owing to the "water-lubricating" effect, $V_2O_5\cdot nH_2O$ delivered excellent rate performance and a remarkably long lifespan

compared to V_2O_5 without structural water. Density functional theory (DFT) calculations were performed to theoretically elucidate the vital role of structural water. Choi's group investigated the possible Zn-ion diffusion paths and kinetic energy barrier for zinc ion diffusion in V_6O_{13} with and without structural water.[72] As shown in Fig. 3b, because the strong electrostatic repulsion was reduced in the hydrous structure, the migration pathway of Zn^{2+} ions along the b-axis exhibits a zigzag route. The Zn^{2+} ion moves straight forward and leans to one side in the structure without water (Fig. 3c). In addition, as shown in Fig. 3d, the structure with water shows a larger cross-sectional area (formed by V and O) than the structure without water. This is related to the larger unit cell volumes in the hydrous structure when zinc ions intercalate into the structure. The DFT results also suggest that the kinetic barrier for Zn ion diffusion in V_6O_{13} with structural water is much smaller than that of the vanadium oxide without structural water, which are 0.87 eV and 2.85 eV (Fig. 3e), respectively. This lower Zn^{2+} migration energy

19250 | *J. Mater. Chem. A*, 2021, **9**, 19245–19281

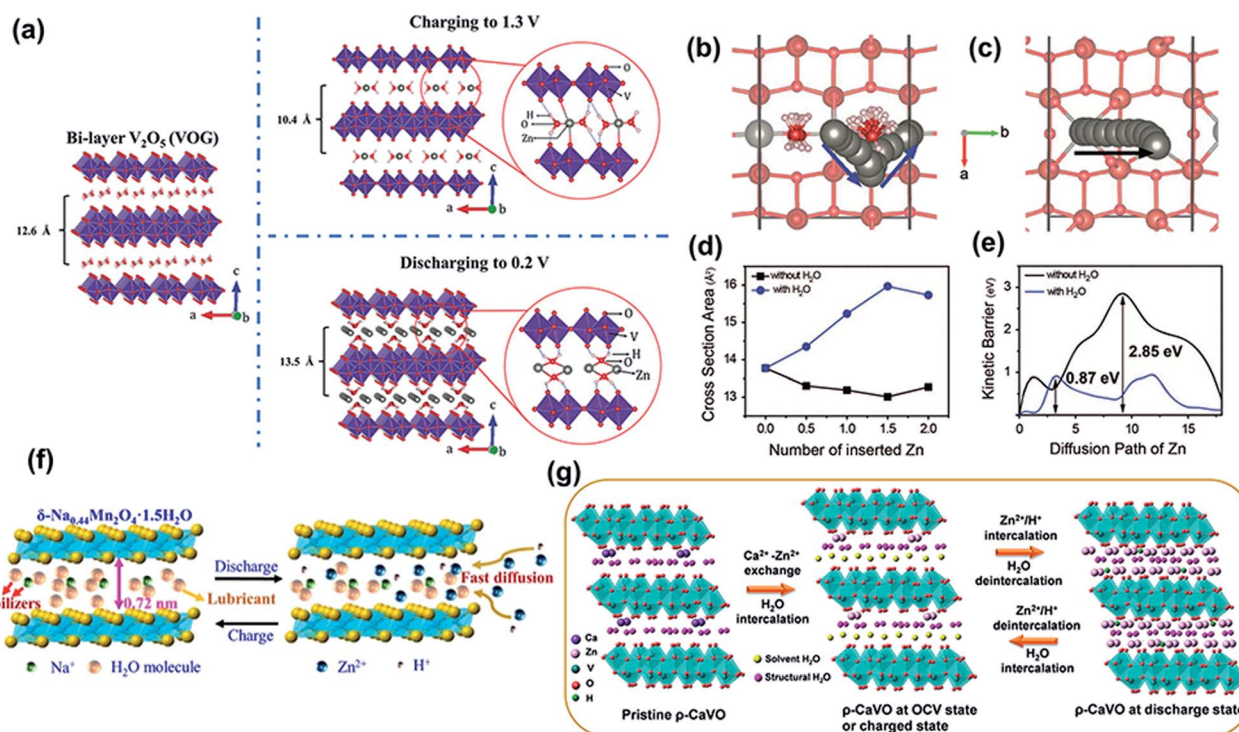This journal is © The Royal Society of Chemistry 2021

Fig. 3 (a) The proposed crystal structures of pristine $V_2O_5 \cdot nH_2O$, and $V_2O_5 \cdot nH_2O$ after charging to 1.3 V, and discharging to 0.2 V. Reproduced with permission.[47] Copyright 2017, Wiley-VCH. Diffusion paths of Zn ions (b) with and (c) without water (projected down [001]). (d) Change in the cross-sectional area of the diffusion path during Zn intercalation with and without water. (e) Calculated diffusion barriers for paths in (b) and (c). (b–e) Reproduced with permission.[72] Copyright 2019, Wiley-VCH. (f) Schematic of Na ion and water molecule pre-intercalated δ-MnO_2 for Zn ion storage. Reproduced with permission.[76] Copyright 2019, American Chemical Society. (g) Schematic illustration of the reaction mechanism of ρ-CaVO. Reproduced with permission.[78] Copyright 2019, American Chemical Society.

barrier was also verified in an inorganic open-framework (IOF) phosphovanadate cathode ($KV_2O_4PO_4 \cdot 3.2H_2O$) with abundant lattice water.[73] Benefiting from the "charge shield" of crystal water, the kinetic barrier for Zn ion diffusion in the hydrous structure is 0.66 eV along the b-axis, which is smaller than that in the structure without water (0.81 eV).

Apart from the water-lubricating effect, the structural water intercalating into the layers of the host cathode can increase the interlayer distance. For example, layered manganese oxide containing crystal water (cw-MnO_2) was proven to have a d-spacing of 7.25 Å,[74] in which the content of crystal water was up to ~10 wt%. To reveal the role of crystal water, cw-MnO_2 was heat-treated at 100 and 300 °C to obtain samples with different water contents. As expected, the sample capacity and long-term cycling performance gradually decreased with a reduced water content. Thus, it can be concluded that the improved cycling stability of the cathode is associated with appropriate interlayer spacing and a high content of crystal water, which relieves the dissolution of manganese and maintains its structural stability. Besides, water-incorporated MoS_2 nanosheets were reported. The XRD patterns showed that the diffraction peaks of the (002) plane in hydrated MoS_2 shifted to a lower angle than that of dehydrated MoS_2.[75] This revealed that the intercalated structural water led to a larger interlayer spacing, which was beneficial for reducing the Zn^{2+} diffusion resistance. According to

the electrochemical impedance spectroscopy (EIS) results, hydrated MoS_2 exhibits a much smaller R_{ct} (1.6 Ω) than dried MoS_2 (150 Ω), suggesting that the charge transfer kinetics were effectively improved. In addition, the zinc-ion diffusion coefficient of hydrated MoS_2 is three orders of magnitude higher than that of dried MoS_2. Moreover, the desolvation barrier of hydrated zinc ions in MoS_2 during the discharge process also decreased. This was attributed to the interlayer water could relay the solvation water of hydrated Zn^{2+} when the Zn^{2+} intercalated into the MoS_2.[75] Structural water incorporated with other ions can also be used to expand the interlamellar spacing. For instance, water with preintercalated Mg^{2+} into the interlayers of V_2O_5 delivers a wide interplanar spacing of 13.4 Å.[35] Besides, Na^+ ions and water molecules were cointroduced into layered δ-MnO_2 ($Na_{0.44}Mn_2O_4 \cdot H_2O$) and the interlayer spacing increased to 0.72 nm (Fig. 3f).[76] The synergy between the expanded interlayer spacing and water-lubricating effect is beneficial for reducing electrostatic interactions between the inserted zinc ions and VO framework and facilitating the diffusion of zinc ions, which endows the cathode with outstanding cycling stability and reversibility.

In addition to the preintercalated structural water in the preparation process mentioned above, water molecules in the electrolyte solution were also inserted into the interlayer of the cathode during the energy storage process. For instance, the d-

spacing of the (001) plane of $NH_4V_4O_{10}$ expands from 9.8 Å to 11.1 Å after immersion in an aqueous electrolyte,[77] which is associated with the intercalation of solvent water to enlarge the interlayer distance. In addition, the (001) plane of the cathode in the charge state was still larger than that of the original $NH_4V_4O_{10}$ powder, suggesting that the intercalated solvent water remained in the layered structure of $NH_4V_4O_{10}$ during the zinc-ion insertion/extraction process. The inserted water synergizes with NH_4^+ to maintain structural stability, effectively reducing the strong electrostatic reaction between Zn^{2+} and the VO framework. Similarly, solvent water was intercalated into the layers of $Ca_{0.67}V_8O_{20} \cdot 3.5H_2O$ (CaVO) after soaking in an aqueous electrolyte,[78] expanding d_{001} from 10.68 to 13.03 Å. The solvent water was expelled from the interlayer of CaVO after the insertion of zinc ions in the discharge state. Upon charging, the solvent water was intercalated into the interlayer again, accompanied by zinc ion extraction (Fig. 3g).

In addition to the intercalation of water molecules, organic molecules have also been successfully intercalated into layered host materials. For instance, polyaniline (PANI) was intercalated into the layers of V_2O_5 *via* an *in situ* hydrothermal reaction,[79] causing an increased interlayer distance (13.90 Å) and effectively facilitating Zn^{2+} diffusion. More importantly, the special π-conjugated structure of PANI blocked the electrostatic interactions between Zn^{2+} and O^{2-}. The DFT results show that the Fermi level is near the conduction band and that an intermediate level appears across the Fermi level after intercalating PANI, which accelerates electronic transport and zinc-ion migration. PANI was also successfully introduced into MnO_2, which reinforced the layered structure.[80] Moreover, the guest PANI synergized with nanosized (~10 nm) MnO_2 to eliminate the phase changes during cycling and maintain a stable layered structure. Thus, the cathode exhibited long-term cycling stability for 5000 cycles at a current density of 2 A g^{-1} with a capacity utilization of 40%. Additionally, poly(3,4-ethylenedioxythiophene) (PEDOT) was embedded into layered V_2O_5 near the grain surface *via in situ* polymerization,[48] triggering zinc ions to reach deeper interlayers due to the cascading effect. DFT calculations show that there are three possible Zn^{2+} diffusion pathways based on the enlarged interlayer spacing of V_2O_5@PEDOT. In contrast, V_2O_5 possessed only one suitable site for Zn absorption and the corresponding absorption energy was higher than that of V_2O_5@PEDOT. Thus, the preintercalated PEDOT promotes zinc-ion diffusion kinetics in the layered V_2O_5 framework. Moreover, the shallow-layer pillaring of PEDOT tends to suppress the dissolution of the cathode due to its hydrophobic character.

2.1.3 Introduction of dual ions/molecules. As summarized in the previous section (2.1.1), various metal ions can be used as guest ions in cathode materials. Apart from single ions, dual ions were introduced into the crystal structure to optimize the electrochemical performance. For example, a Na^+ and Ca^{2+} coinserted V_3O_8 layered structure ($NaCa_{0.6}V_6O_{16} \cdot 3H_2O$, NaCaVO) was successfully prepared (Fig. 4a).[81] The intercalated cations (Na^+/Ca^{2+}) stabilized the layered structure during long-term cycling. More importantly, the diffusion barriers of Zn^{2+} in NaCaVO were obviously decreased, suggesting that the

intercalated Na^+/Ca^{2+} could promote zinc-ion migration. However, the introduction of Na^+/Ca^{2+} into the crystal structure did not improve the conductivity of the cathode.

According to a previous report, transition metal ions enhance the conductivity,[39] resulting in the improvement of electrochemical performance. The ion transport and electronic conductivity of the cathode can be improved simultaneously through doping with different ions. Based on this, a transition metal ion and alkali metal cation were preinserted into a V_8O_{20} electrode together.[82] Preinserted Mn^{2+}/Mn^{3+} increased the electrical conductivity of the vanadium-based cathode, and preinserted Na^+ promoted zinc-ion diffusion. Notably, $(Na_{0.97},Mn_{0.02})V_8O_{20} \cdot 0.32H_2O$ (Mn1-NVO) exhibits a higher electron density near the Fermi level than NaV_8O_{20} (NVO) (Fig. 4b), indicating that the preintercalated Mn ions contribute to an enhanced electrical conductivity. In addition, NVO shows a lower energy barrier for Zn^{2+}-migration along the *b*-axis than Mn1-NVO and MnV_8O_{20} (MnVO) (Fig. 4c and d), suggesting that compared to Mn ions, Na ions play a more crucial role in boosting zinc ion diffusion. Moreover, the Mott–Schottky plots show that NaV_8O_{20} doped with transition metal (Mn, Fe, Co, and Ni) ions exhibits a higher charge carrier density than alkali metal (K and Ca) ion-intercalated NaV_8O_{20}. In addition, the Tafel curves demonstrated that the transition metal ions introduce the "catalytic effect" to accelerate the electron transfer and redox reaction.

The ionic radius of organic cations is usually larger than that of metal ions, which makes them promising candidates for interlayer intercalation. A V_8O_{20} cathode cointercalated with metal ions (Zn^{2+}) and organic ions ($[N(CH_3)_4]^+$) was prepared as a cathode for ZIBs (Fig. 4e).[42] The zinc ions cooperated with $[N(CH_3)_4]^+$ and acted as pillars to stabilize the crystal structure. More importantly, as shown in Fig. 4f and g, Zn–C exhibits a lower bond overlap population (0.18) than Zn–O (0.33, 0.28, and 0.33) based on the DFT calculated results, and Zn–C has a longer bond length (2.43 Å) than Zn–O (2.16, 2.27, and 2.16 Å). These results suggest that the intercalated zinc ions during discharge form a weaker interaction with the carbon in $[N(CH_3)_4]^+$ than with the oxygen atoms in the VO framework, which is conducive to reversible zinc-ion insertion/extraction. In addition to dual-ion cointercalation, conductive polymers cointercalated with inorganic ions have also been realized in vanadium-based host materials. For example, an NH_4^+ and PEDOT cointercalating V_3O_8 layered structure was used as a cathode for ZIBs.[83] As shown in Fig. 4h and i, the interplanar spacing of the $NH_4V_3O_8$ cathode is 7.8 Å, which is further expanded to 10.8 Å after introducing PEDOT. This enlarged spacing promoted the stability of the cathode due to the increased migration pathway for Zn^{2+} storage. Furthermore, based on DFT calculations, $NH_4V_3O_8$ with inserted PEDOT was also demonstrated to have a lower zinc-insertion energy due to a larger interlayer space. Thus, the strategy of two dual-ion insertions may combine the advantages of different ions or polymers and endow the cathode with excellent energy storage behavior.

19252 | *J. Mater. Chem. A*, 2021, **9**, 19245–19281

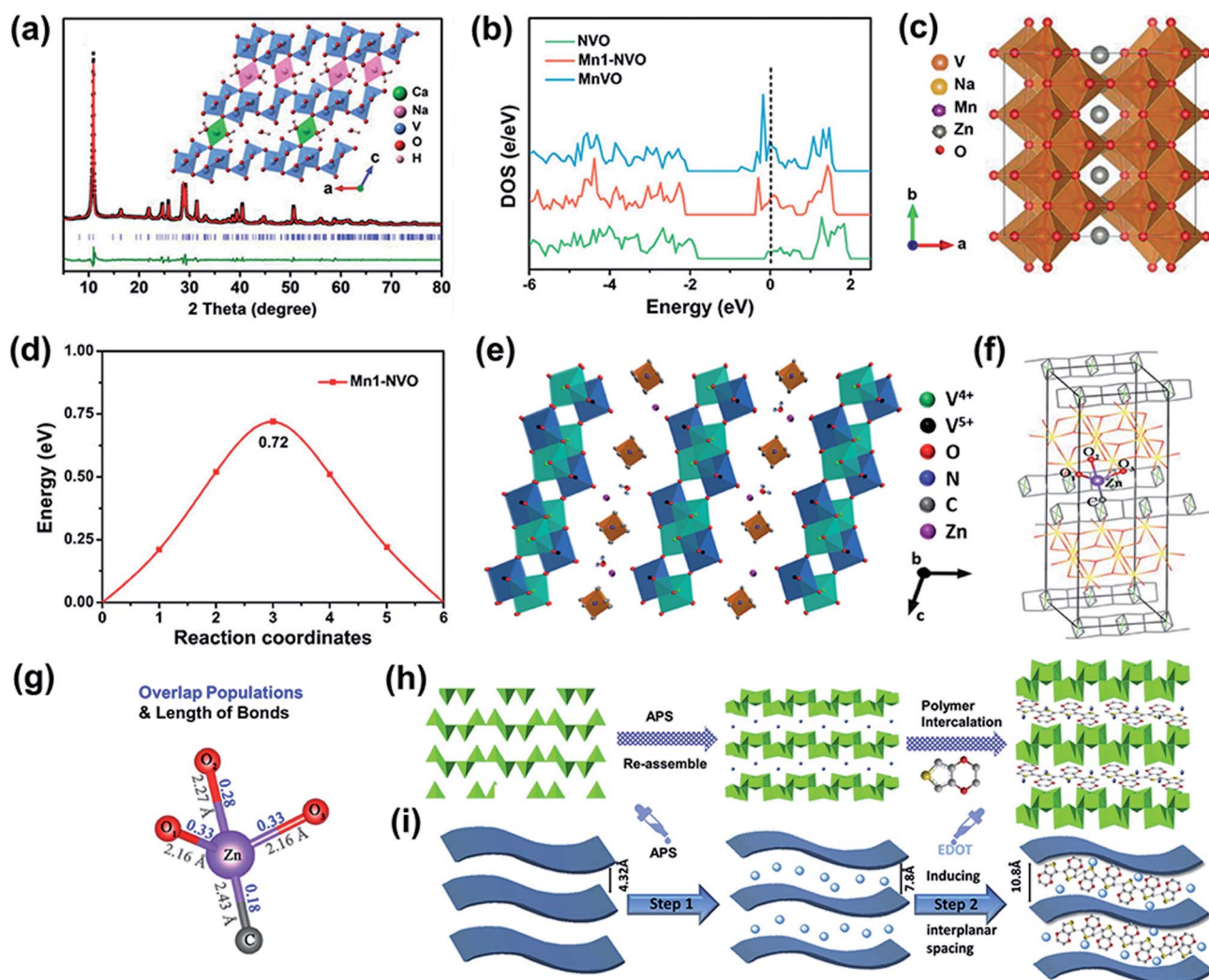This journal is © The Royal Society of Chemistry 2021

Fig. 4 (a) Experimental and Rietveld-refined XRD patterns; inset: the crystal structure of NaCaVO viewed along the *b*-axis. Reproduced with permission.[81] Copyright 2019, Wiley-VCH. (b) Density of states of NVO, Mn1-NVO, and MnVO. (c) Possible migration pathways for Zn^{2+} in Mn1-NVO. (d) Energy barriers along Zn^{2+}-migration pathways for Mn1-NVO.[82] (e) Schematic of Zn^{2+} diffusion in the discharged state in TMAVO. (f) Computation model of $[N(CH_3)_4]V_8O_{20}$. (g) Results of bond overlap populations of Zn–C and Zn–O for $[N(CH_3)_4]V_8O_{20}$. (e–g) Reproduced with permission.[42] Copyright 2020, Zhengzhou University. Schematic illustration of the preparation process of PEDOT-intercalated NVO-layered material. (h) Illustration of structural changes. (i) Description of simulation changes. (h and i) Reproduced with permission.[83] Copyright 2020, Elsevier.

2.2 Defect engineering

Defect engineering is a powerful strategy that can significantly affect the electronic and crystal structures of electrode materials. For instance, introducing vacancies has been regarded as an important strategy to optimize the electrochemical performance of the cathode for ZIBs.[84,85] Here, we summarize the strategies for introducing oxygen vacancies, sulfur vacancies, and cationic vacancies. In particular, we focus on the effect of defect engineering on Zn^{2+} storage. Defect engineering can promote the kinetics of electrode materials, form abundant active sites, and stabilize the electrode structure; these are discussed in detail below.

2.2.1 Strategies for introducing defects. Introducing anion defects is a promising strategy to modulate the electronic

properties of cathode materials.[86] Oxygen defects are the most common form of anionic defects. Introducing oxygen defects usually requires a reducing environment. One possible method involves the use of chemical reagents with strong reducibility. Because of the strong reducibility of H^- in $NaBH_4$, the use of $NaBH_4$ solution is a cost-effective and easy method to introduce oxygen defects at room temperature. For instance, $VO_2(B)$ with oxygen defects was prepared by reducing with $NaBH_4$ solution.[87] After the reduction process, oxygen defects were successfully introduced into the crystal structure and the chemical formula of $VO_2(B)$ changed to $VO_{1.88}$.

Another method is heat treatment in a reducing atmosphere. Birnessite-MnO_2 with oxygen defects was prepared through calcination with $NaBH_4$ at 400 °C.[88] A H_2 reduction atmosphere was generated *in situ* when $NaBH_4$ was heated at high

This journal is © The Royal Society of Chemistry 2021

J. Mater. Chem. A, 2021, **9**, 19245–19281 | **19253**

temperature. The reducing H_2 atmosphere could also be introduced by using a H_2/N_2 mixed gas flow. Oxygen-deficient $ZnMn_2O_4$ was successfully prepared by annealing $ZnMn_2O_4$ powder in a reducing atmosphere (H_2/N_2 mixed gas).[89] The volume ratio of H_2/N_2 was 3/1 and the flow rate was 200 sccm with a ramp rate of 2 °C min^{-1}. Apart from H_2, PH_3 and NH_3 gases could also be used to create a reducing atmosphere. Nickel cobaltite ($NiCo_2O_4$) nanosheets were annealed in the presence of $NaH_2PO_2 \cdot H_2O$ at 300 °C in a N_2 atmosphere.[90] The generated PH_3 gas from $NaH_2PO_2 \cdot H_2O$ was used to reduce $NiCo_2O_4$ and introduce oxygen vacancies into nickel cobaltite ($NiCo_2O_{4-x}$). Notably, MnO_2 easily transforms into Mn_3O_4 if the heat treatment temperature rises above 300 °C.[91] Thus, abundant oxygen defects were successfully introduced into the MnO_2 branch through a low-temperature (200 °C) treatment process with a gas flow of NH_3 for 2 h at a heating rate of 10 °C min^{-1}. Meanwhile, N was doped into MnO_2 in an atmosphere of NH_3 gas.

In addition, oxygen-deficient active materials can be obtained only through annealing at high temperatures without a reducing atmosphere. For example, $K_{0.8}Mn_8O_{16}$ with oxygen vacancies was prepared using a thermal treatment method at 800 °C in a muffle furnace.[68] The oxygen atoms easily escape from the VO framework at high temperatures, leaving oxygen defects in $K_{0.8}Mn_8O_{16}$. Apart from the oxygen defects in oxides, sulfur vacancies are ubiquitous in sulfides. Sulfur-deficient MoS_{2-x} nanosheets were prepared by sintering in an argon atmosphere at 250 °C.[92] Interestingly, when the sintering temperature was increased to 750 °C, defect-free MoS_2 with high crystallinity was obtained. Thus, the introduction of defects can be realized at appropriate calcination temperatures.

Besides calcination, the hydrothermal method is a facile technique for introducing oxygen defects. Vanadium bronzes ($NH_4V_4O_{10}$) with oxygen deficiencies (O_d-NVO·nH$_2$O) were fabricated through a one-step hydrothermal reaction.[93] Oxygen vacancies were successfully introduced into the cathode materials after increasing the amount of oxalic acid and adding extra ammonium fluoride during synthesis. The synergistic effect between the reducing reagent (oxalic acid) and NH_4F introduced oxygen defects and etched the microstructure of $NH_4V_4O_{10}$. Apart from the hydrothermal reaction, the solid diffusion process is another effective technique for introducing oxygen defects under mild conditions. For instance, tunneled α-MnO_2 with oxygen defects was synthesized through surface gradient Ti doping.[50] First, MnO_2 nanowires were prepared by the hydrothermal method, and then TiO_2 was grown on MnO_2 nanowires *via* atomic layer deposition. Owing to the substantial difference in the Fermi level between Ti^{4+} and Mn^{4+}, the Ti atoms substituted the Mn atoms in the [MnO_6] octahedra. Thus, Ti was doped into MnO_2 and was simultaneously accompanied by the generation of oxygen vacancies.

Cation vacancies have also been introduced into cathode materials to improve their electrochemical performance. Recently, cation deficient $Zn_{0.3}(NH_4)_{0.3}V_4O_{10} \cdot 0.91H_2O$ was reported as a cathode for aqueous ZIBs through a two-step hydrothermal reaction.[94] First, $NH_4V_4O_{10}$ was synthesized, followed by another hydrothermal reaction, in which Zn^{2+} was preintercalated into $NH_4V_4O_{10}$ and simultaneously created cation vacancies. Also, a cation-deficient spinel $ZnMn_2O_4$ cathode was successfully prepared through a two-step method.[95] In the synthesis process, $NH_3 \cdot H_2O$ was added to the precursor, which assisted in oxidation precipitation. The mixture was then crystallized to the spinel phase with cation redistribution after heating at 180 °C in air, and cation deficiencies were produced. Cation defects can also be produced during an electrochemical reaction process. Mn-defect MnO was fabricated through an *in situ* electrochemical extraction approach.[96] The X-ray photoelectron spectroscopy (XPS) results showed that the distance between the splitting peaks decreased after the first charging, indicating that the oxidation state of Mn increased. This was attributed to the Mn^{2+} extracted from the MnO framework into the aqueous electrolyte during the initial charge process, leaving Mn defects in the MnO host. Similarly, a disordered rocksalt vanadium oxynitride (VN_xO_y) with abundant vacancies/defects was constructed through a conversion reaction in an aqueous electrolyte during the initial charge process.[97] The abundant low-valent oxygen (O^{2-}) in the rocksalt vanadium oxynitride was substituted by high-valent anion nitrogen (N^{3-}) during the initial charge, producing abundant vacancies previously occupied by vanadium.

2.2.2 Effect of defects. Defect engineering has been increasingly demonstrated to play a significant role in boosting the energy storage performance of cathodes for aqueous ZIBs. The introduced defects in a cathode structure ameliorate the inherent deficiencies in the zinc-ion storage process, such as its sluggish kinetics, poor conductivity, unstable crystal structure, and insufficient active sites. This section discusses the critical effects of defect engineering on promoting the electrochemical performance of cathodes, including promoting kinetics, improving conductivity, and increasing active sites.

(1) Defects can promote the kinetics of electrode materials. In particular, oxygen defects are among the most powerful strategies to effectively weaken the strong interaction between intercalated zinc ions and a vanadium oxide cathode. Various vanadium-based cathode materials (V_4O_{10}, V_6O_{13}, and VO_2) with oxygen defects have been widely explored.[93,98,99] For instance, oxygen-deficient V_6O_{13} (O_d-VO) has been reported as a cathode for ZIBs.[98] Because of the extraction of electronegative oxygen atoms from the VO framework, reversible Zn^{2+} insertion/extraction is promoted during cycling. This is mainly because of the decreased interactions between the oxygen atoms and divalent Zn^{2+}. Thus, the O_d-VO cathode in the discharge and charge states exhibits much higher Zn^{2+} diffusion coefficient (D_{Zn}) values of 1.1×10^{-11} and 0.4×10^{-11} cm^2 s^{-1} respectively, than the defect-free structure. Moreover, the zinc ion diffusion pathway is usually along the a–b plane in the layered crystal structure of vanadium-based compounds.[38,58] The presence of oxygen vacancies in O_d-VO may open up the layered structure of vanadium oxide, enabling the diffusion of zinc ions along the c-axis except for the pathway along the a–b plane (Fig. 5a and b), thus promoting the reaction kinetics. A similar function of oxygen defects providing another channel for ion transport was reported for a β-MnO_2 cathode.[100] The presence of oxygen defects not only provided an extra pathway in the [MnO_6]

19254 | *J. Mater. Chem. A*, 2021, **9**, 19245–19281

This journal is © The Royal Society of Chemistry 2021

Fig. 5 Structure of (a) p-VO and (b) O_d-VO. (a and b) Reproduced with permission.[98] Copyright 2019, Wiley. (c) Calculated diffusion barriers for paths in perfect KVO and O-defective KVO. Reproduced with permission.[101] Copyright 2019, Wiley. (d) Calculated Zn ion diffusion energy barriers in VO_2 and $VO_{1.75}$. Reproduced with permission.[99] Copyright 2020, American Chemical Society. (e) The projected density of states (PDOS) and the total density of states (TDOS) of defective and perfect NVO. Reproduced with permission.[93] Copyright 2020, Royal Society of Chemistry. (f) The calculated adsorption energies for Zn^{2+} on the surfaces of perfect σ-MnO_2 and σ-MnO_2 with oxygen vacancies. Reproduced with permission.[102] Copyright 2019, Wiley. (g) Schematic illustration of interlayer expanded MoS_2. (h) Schematic illustration of hydrophilicity tuning. (g and h) Reproduced with permission.[103] Copyright 2019, American Chemical Society.

polyhedron walls for guest-ion diffusion but also provided more ion absorption sites. Benefiting from this, oxygen-deficient β-MnO_2 exhibited a higher capacity and reversibility than β-MnO_2. The capacity retention of oxygen-deficient β-MnO_2 was 94% after 300 cycles at 0.5 A g^{-1}. In comparison, the commercial β-MnO_2 cathode delivered a lower capacity retention of 78%.

In addition, oxygen defects play a crucial role in reducing the Zn-ion diffusion energy barrier to promote zinc ion diffusion, which was further analyzed through DFT calculations. As shown in Fig. 5c, oxygen-defective potassium vanadate (KVO) exhibits a significantly lower Zn^{2+} diffusion barrier (0.63 eV) than the perfect KVO structure (1.34 eV),[101] verifying that the oxygen vacancies can accelerate Zn^{2+} diffusion. Besides, the lower diffusion energy barrier in the structure with oxygen defects was also verified in a tunnel-like structure with values of 0.24–0.71 eV and 0.78 eV for $VO_{1.75}$ and VO_2 along the b tunnel,[99] respectively, as shown in Fig. 5d. Thus, oxygen defects can reduce the migration energy barrier of Zn^{2+} ions in the cathode structure and promote the reaction kinetics.

(2) Oxygen defects can improve the electronic conductivity of the active material, which is one of the most important factors affecting electron transfer and electrochemical performance. For instance, enriched oxygen defects were introduced into a hydrated $NH_4V_4O_{10}$ cathode (O_d-NVO·nH$_2$O) to regulate the electronic structures, exhibiting a higher capacity (435 mA h g^{-1}) than that of NVO (405 mA h g^{-1}).[93] This superior electrochemical performance is associated with an improvement of conductivity. As shown in Fig. 5e, the calculation results demonstrate that the defect states (gap states) of the defective NVO were closer to the Fermi level than the perfect NVO. Also, the defect states (donor) were located near the conduction band minimum (CBM) based on the results of the projected density of states (PDOS) and the total density of states (TDOS). Thus, the electrons at the donor level can be easily excited into the conduction band, leading to the improved electronic conductivity of the defective NVO and accelerating electron transport during the electrochemical reaction process. In addition, electron migration was promoted by constructing an oriented electric field in oxygen-defective α-MnO_2, which was prepared

This journal is © The Royal Society of Chemistry 2021

J. Mater. Chem. A, 2021, **9**, 19245–19281 | **19255**

through surface gradient Ti doping.[50] The substitution of Ti and derived oxygen vacancies in the crystal structure forms a depletion zone and induces a local in-plane electric field, which is beneficial for facilitating ion diffusion/electron transport. The redox reaction during the zinc ion storage process is strongly associated with the electron transport rate. Thus, the synergy between ion migration and electron transport contributed to the superior energy storage behavior of the cathode materials.

Apart from oxygen defects, cationic defects can also increase the conductivity. Mn atoms extracted from the MnO crystal structure into an electrolyte leave behind Mn cation defects ($Mn_{0.61}\square_{0.39}O$, $\square$ refers to the Mn defect) after the first charging process.[96] The charge density of MnO with Mn defects around the Fermi level was higher than that of pristine MnO, as revealed by the DOS results, which resulted in better conductivity. Moreover, the Mn cation defects induced the accumulation of electrons near the defects and attracted the intercalation of zinc ions. The introduced defects in the host structure modulate the charge distribution and enhance the conductivity, promoting the reaction kinetics during the Zn^{2+} storage/release process and improving the electrochemical performance.

(3) The presence of defects provides abundant active sites for zinc-ion storage. For example, oxygen vacancies have been successfully introduced into manganese oxide to improve the attainable capacity. The Gibbs free energy of oxygen-deficient MnO_2 for Zn^{2+} adsorption is approximately 0.05 eV around the oxygen vacancy (Fig. 5f),[102] which is very close to thermoneutral values. In contrast, pristine MnO_2 exhibits a much lower Gibbs free energy (≈ -3.31 eV). This result indicates that the adsorption/desorption of zinc ions is more reversible on oxygen-deficient MnO_2 than on pristine MnO_2. Furthermore, a renewed active surface area is available for the next adsorption, which aids in enhancing the capacity. In addition, a larger number of electrons contribute to the delocalized electron cloud, further improving the capacity of the cathode. Hence, oxygen-deficient MnO_2 exhibits a higher capacity of 345 mA h g^{-1} at a current density of 0.2 A g^{-1} than MnO_2 (270 mA h g^{-1}).

Apart from the above cathodes, defect engineering also endows the layered metal disulfides with more active sites. For example, sulfur-deficient MoS_{2-x} nanosheets,[92] which ameliorate the poor electrochemical activities of 2H-MoS_2 for Zn-ion storage. MoS_2 with introduced defects possesses many edge sites and vacancies, which offer more active sites for zinc ion storage. In addition, the increased interlayer spacing also results in the availability of more sites for zinc-ion storage and the fast diffusion of Zn^{2+} ions. Thus, the defect-rich MoS_{2-x} nanosheets delivered a high reversible capacity of 88.6 mA h g^{-1} even after 1000 cycles at 1 A g^{-1}, and exhibited a capacity retention of 87.8%. In addition to sulfur defects, the incorporation of heteroatoms into MoS_2 has also been demonstrated to provide more active sites. The inactive cathode for zinc-ion intercalation was converted into functionally active materials *via* oxygen incorporation (MoS_2–O).[103] The replacement of sulfur with oxygen atoms increased the interlayer spacing from 6.2 to 9.5 Å (Fig. 5g), which endowed the layered structure with more space to store zinc ions. In addition, the incorporation of oxygen atoms also played an important role

in enhancing the hydrophilicity of MoS_2 (Fig. 5h). Thus, the Zn^{2+} storage capacity improved 10-fold and the Zn^{2+} diffusivity of the MoS_2–O cathode increased by three orders of magnitude.

2.3 Amorphous structures

Crystal structures exhibit sluggish zinc-ion migration and often undergo phase transitions and structural collapse.[104–106] Compared with crystal materials, amorphous cathodes contain abundant defects and active sites, which enhance pseudocapacitive charge storage properties and high rate capability.[106,107] A metal–organic framework-derived composite including amorphous V_2O_5 and carbon materials (a-V_2O_5@C) was prepared using an *in situ* electrochemical induction strategy.[108] The prepared Zn/a-V_2O_5@C batteries exhibited major pseudocapacitance behavior in their capacity contribution compared with the c-V_2O_5 (crystalline V_2O_5) and a-V_2O_5 cathodes (Fig. 6a), which results in excellent rate capability. The dominant pseudocapacitance and superior rate performance can be ascribed to the amorphous structure of V_2O_5, which endows the composite cathode with more isotropic Zn^{2+} diffusion pathways and active sites. Thus, the amorphous composite of a-V_2O_5@C exhibits a high capacity of 620.2 mA h g^{-1} at 0.3 A g^{-1}. Even when the current density reaches 200 A g^{-1}, the composite displays a capacity of 72.8 mA h g^{-1}. Besides, the a-V_2O_5@C cathode shows a higher Zn^{2+} diffusion rate than c-V_2O_5 and a-V_2O_5 (Fig. 6b), confirming that the amorphous structure helps to realize fast kinetics during zinc-ion insertion/extraction. Amorphous V_2O_5 has a lower Zn^{2+} (de)intercalation energy (1.02 eV) than the corresponding crystalline phase (2.28 eV) based on first-principles calculations (Fig. 6c), further indicating that the transport of Zn^{2+} in amorphous V_2O_5 is easier than that in crystalline V_2O_5. Moreover, the electrochemical performance of the composite is further enhanced due to the porous carbon framework, which endows the cathode material with abundant electron transport pathways and ion migration channels. Thus, the cathode exhibits unprecedented cycling performance. Even after 20 000 cycles at a high current density of 40 A g^{-1}, the capacity is still up to 249.2 mA h g^{-1} and the capacity retention is 91.4%.

Recently, amorphous ternary vanadium oxide ($FeVO_4$) was calcined at 250 °C (FeVO-1) as a cathode for ZIBs and crystalline FeVO was obtained at a higher temperature of 500 °C (Fig. 6d).[109] Amorphous FeVO-1 has a high specific surface area of 80.9 m^2 g^{-1} and has abundant mesopores with an average pore width of ~15.9 nm. These pores provide more spaces for zinc-ion storage and increases the contact area between the electrolyte and cathode. The kinetic mechanism of FeVO-1 was investigated by analyzing the CV curves at different scan rates. It was demonstrated that pseudocapacitance dominates the electrochemical reaction process (Fig. 6e), especially at high current density. Moreover, the bimetallic oxide exhibits higher electronic conductivity than V_2O_5. Benefiting from these advantages, amorphous $FeVO_4$ exhibits improved zinc-ion diffusion kinetics and fast surface Zn^{2+} storage. Thus, compared to highly crystalline FeVO-1, amorphous FeVO-1 delivers a higher capacity and superior long-term cycling stability at 1 A g^{-1}.
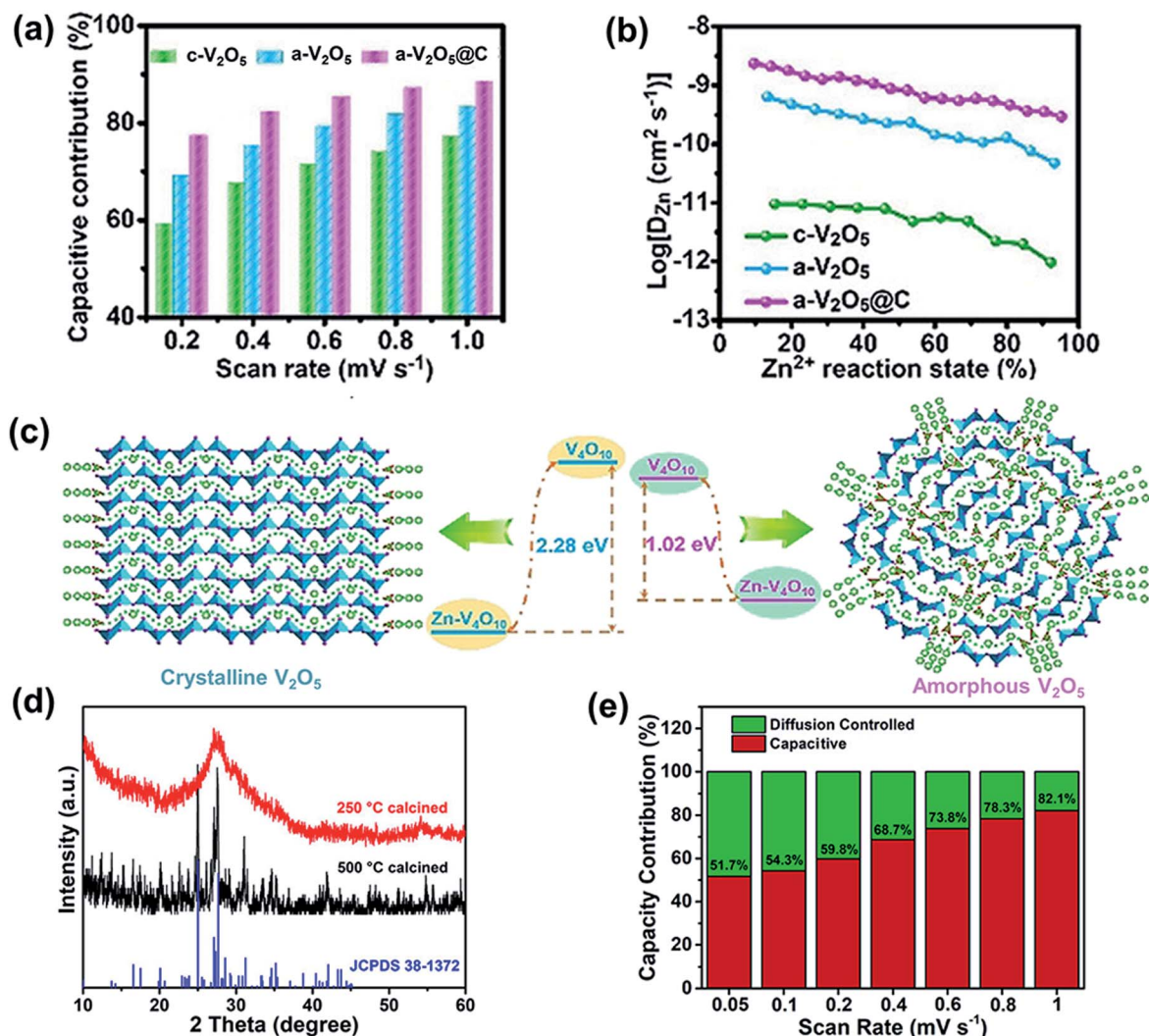
19256 | *J. Mater. Chem. A*, 2021, **9**, 19245–19281

This journal is © The Royal Society of Chemistry 2021

Fig. 6 (a) Capacitive contributions at various scan rates. (b) The Zn^{2+} diffusion coefficient during discharging. (c) Illustration of Zn^{2+} diffusion and Zn^{2+} (de)intercalation energy in crystalline and amorphous V_2O_5 from first-principles calculations. (a–c) Reproduced with permission.[108] Copyright 2020, Wiley. (d) XRD patterns of FeVO-1. (e) Percentages of pseudocapacitive contribution at different scan rates of FeVO-1. Reproduced with permission.[109] Copyright 2020, American Chemical Society.

In addition to vanadium oxide, crystalline manganese oxide as an attractive cathode for aqueous ZIBs usually suffers from phase transitions and structural collapse during cycling, leading to poor long-term cycling performance.[110,111] Thus, an amorphous manganese dioxide (A-$MnO_{2-\delta}$) was fabricated by generating short-range ordered distorted Mn–O polyhedra.[106] A-$MnO_{2-\delta}$ was verified to have a decreased Mn valence and abundant oxygen vacancies. The disordered network array provided more ion-storage active sites to enhance the capacity. In addition, the abundant structural defects endowed the cathode with a better capability to store ions, which boosted ion transfer across the interface between the A-$MnO_{2-\delta}$ cathode and electrolyte. Furthermore, the A-$MnO_{2-\delta}$ cathode exhibited a dominant pseudocapacitive contribution due to its abundant structural defects and intrinsic isotropic nature, which facilitated the reaction kinetics. As a result, the A-$MnO_{2-\delta}$ cathode exhibited a high capacity of 301 mA h g^{-1} at 0.1 A g^{-1} and a high

capacity retention of 78% after 1000 cycles at 1 A g^{-1}. In short, an amorphous framework with the unique property of intrinsic isotropic nature endows the cathode materials with abundant structural defects and active sites for zinc ion storage, which makes a significant pseudocapacitive contribution during the electrochemical reaction process and promotes the reaction kinetics.

2.4 Designing heterostructures

The strategy for designing amorphous structures shows unique advantages in developing high-performance cathode materials with fast ion intercalation and high-rate performance. Constructing a heterostructure incorporated with a unique amorphous structure is a reliable strategy to fully exploit the merits of individual compounds. For example, a 2D sandwich-like heterostructure combining amorphous vanadium pentoxide and graphene (A-V_2O_5/G) was successfully prepared through an ion

This journal is © The Royal Society of Chemistry 2021

J. Mater. Chem. A, 2021, **9**, 19245–19281 | **19257**

adsorption approach.[107] The transmission electron microscopy (TEM) image shows heterostructures with an ultrathin flat morphology (Fig. 7a). The high resolution TEM (HRTEM) image without any lattice fringes and selected area electron diffraction (SAED) without diffraction spots both confirmed the amorphous structure (Fig. 7b). The A-V$_2$O$_5$/G heterostructure exhibited an ultrahigh capacity of 489 mA h g^{-1} at 0.1 A g^{-1} and a remarkable rate capability of 123 mA h g^{-1} even at an ultrahigh current density of 70 A g^{-1}. Its outstanding energy storage behavior can be ascribed to strong synergy between the heterostructure materials. First, the amorphous structure provides abundant active sites for zinc-ion storage and tolerates the large volume variation upon cycling. Second, graphene with a high electrical conductivity accelerates electron transport. Third, the ultrathin nanosheet (~5 nm) structure shortens the ion diffusion pathway. Thus, the heterostructure combines the advantages of the amorphous V$_2$O$_5$ structure and graphene to enhance the capacitive-controlled kinetic process and improves the conductivity, thereby achieving an ultrahigh capacity and rate capability.

In addition, graphene was intercalated into the MoS$_2$ framework, forming a sandwich-like heterostructure (MoS$_2$/graphene) as a cathode for high-performance aqueous ZIBs.[112] Notably, bulk MoS$_2$ is almost purely the 2H-phase, while MoS$_2$ in the heterostructure shows a high 1T-phase content. The synergistic effect of 1T-MoS$_2$ and rGO with abundant oxygen-containing groups improved the hydrophilicity of MoS$_2$. In addition, the interlayer spacing of MoS$_2$ was 0.62 nm, which apparently enlarged to 1.16 nm after the introduction of graphene into the gallery. To investigate the diffusion dynamics of the heterostructure, the Zn^{2+} migration barriers were calculated via DFT computations. Bulk MoS$_2$ exhibited an ion migration barrier of 0.991 eV (Fig. 7c), which was much higher than that of the MoS$_2$/graphene heterostructure. Moreover, the DFT results showed that the Zn^{2+} migration barriers gradually decreased as the MoS$_2$-to-graphene distance increased (Fig. 7d). When the distance between MoS$_2$ and graphene was 4.86 Å, the Zn^{2+} migration barrier was 0.425 eV. After expanding the distance to 6.5 Å, the value of the Zn^{2+} migration barrier was reduced to 0.024 eV. The lower ion migration barriers indicate fast kinetics during the zinc-ion insertion/extraction process. DFT was also conducted to analyze the density of states (DOS) of the heterostructure and bulk MoS$_2$. As displayed in Fig. 7h, the heterostructure shows considerable states at the Fermi level, revealing
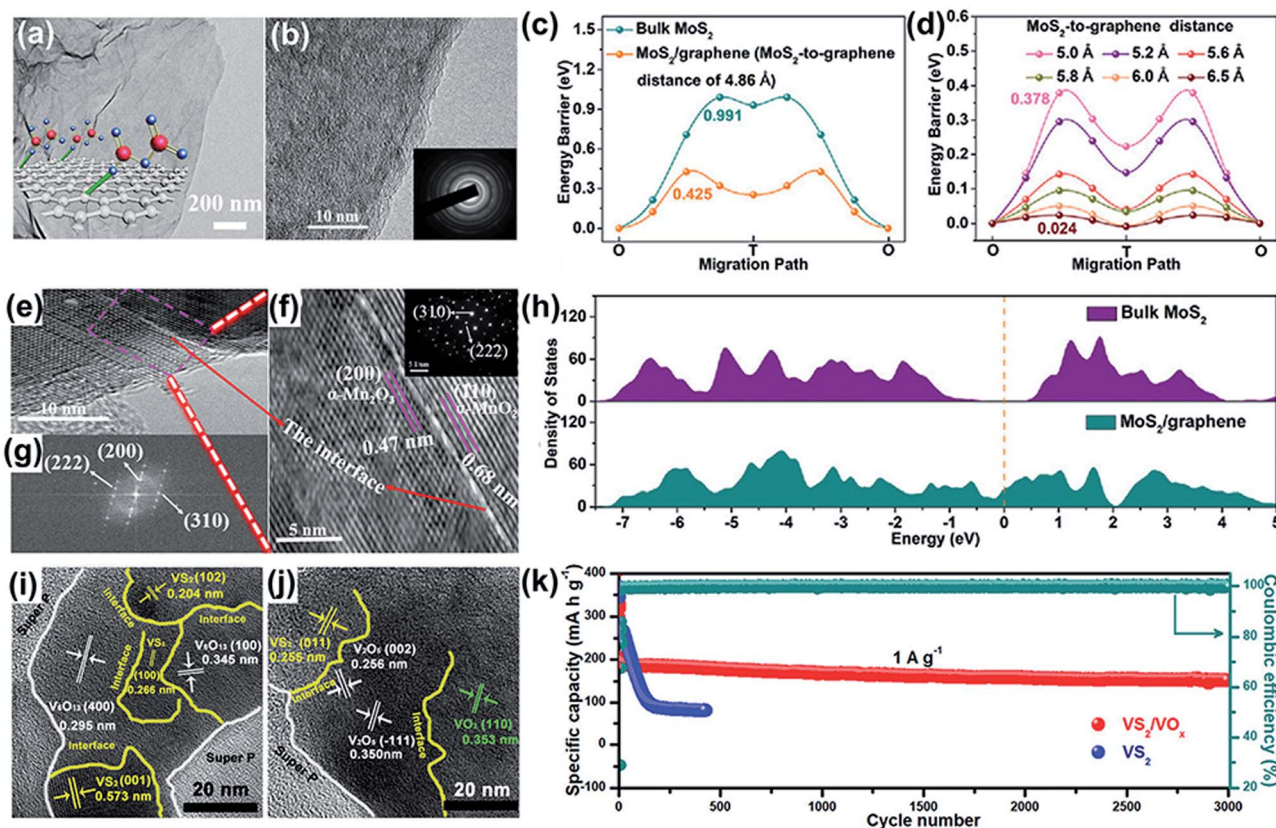

Fig. 7 (a) TEM image of A-V$_2$O$_5$/G heterostructures. (b) HRTEM image and SAED pattern (inset) of A-V$_2$O$_5$/G. Reproduced with permission.[107] Copyright 2020, Wiley. (c and d) The migration energy barriers with the variation of the MoS$_2$-to-graphene distance. (h) Density of states of bulk MoS$_2$ and MoS$_2$/graphene. (c, d and h) Reproduced with permission.[112] Copyright 2021, Wiley. Low magnification (e) and high magnification (f) HRTEM images of α-(Mn$_2$O$_3$–MnO$_2$). The inset of (f) shows the SAED pattern with diffraction spots for α-(Mn$_2$O$_3$– MnO$_2$). (g) Fast Fourier transform image in HRTEM image (e). (e–g) Reproduced with permission.[113] Copyright 2020, American Chemical Society. (i and j) The HRTEM images of VS$_2$/VO$_x$. (k) The cycling performance of VS$_2$/VO$_x$ and VS$_2$ at 1 A g^{-1}. (i–k) Reproduced with permission.[114] Copyright 2020, Wiley.

19258 | J. Mater. Chem. A, 2021, 9, 19245–19281

This journal is © The Royal Society of Chemistry 2021

the metallic properties of MoS_2/graphene with high electronic conductivity. In contrast, bulk MoS_2 is a semiconductor because it has an $\sim$0.8 eV bandgap. Therefore, benefiting from the low Zn^{2+} migration barriers and improved conductivity, the heterostructure exhibits excellent electrochemical performance.

A similar DFT result was obtained for twinborn α-(Mn_2O_3–MnO_2) heterostructures,[113] which were prepared by an *in situ* phase transformation after calcination. The HRTEM images show the coexisting lattice fringes of α-Mn_2O_3 and α-MnO_2, confirming the formation of heterojunctions (Fig. 7e–g). Mn_2O_3 and MnO_2 show obvious band gaps, revealing their insulating nature. However, the α-(Mn_2O_3–MnO_2) heterostructure shows a DOS peak crossing the Fermi level, suggesting its metallic nature. This results in improved electrical conductivity, which accelerates Zn^{2+} diffusion and promotes charge transport. Moreover, the heterostructure displays a DOS peak and its center is located at the Fermi level, indicating that the heterostructure possesses improved electronic conductivity and fast redox kinetics. Therefore, the α-(Mn_2O_3–MnO_2) heterostructure shows superior reversibility and high chemical reactivity.

In addition, a heterostructure of VS_2/VO_x was fabricated by the *in situ* oxidation of VS_2 to VO_x during the initial charging process.[114] The HRTEM images show that the VO_x in the heterostructure consists of V_6O_{13}, V_2O_5 and VO_2 (Fig. 7i and j). Owing to the electric field formed at the interfaces of the heterostructure, electronic migration is enhanced. Due to the high conductivity of VS_2 and the high chemical stability of VO_x, the heterostructure of VS_2/VO_x delivers superior long-term stability to pure VS_2 (Fig. 7k). Furthermore, the average working voltage of VS_2/VO_x is higher than that of VS_2, which is increased by 0.25 V. Thus, the heterostructure exhibits a higher energy density of 280 W h kg^{-1} compared to VS_2 (208 W h kg^{-1}) based on their similar capacities. As proven by these reports, the construction of a heterostructure is a promising strategy for producing a cathode with high electrochemical performance. The heterostructure combines the merits of both compounds to achieve high conductivity, abundant active sites, and a stable structure. As a result, the heterostructure shows the synergistic effect between them, thus enhancing the kinetics and improving capacity.

2.5 Surface coating

Generally, most active materials for ZIBs suffer from poor intrinsic conductivity, dissolution in aqueous electrolytes, and phase transition during long-term cycling, which leads to architectural collapse and capacity decay.[115,116] Surface coating is an effective strategy to modulate the surface properties of the cathode. It not only forms a protective interfacial layer to prevent the cathode from directly contacting with the electrolyte but also inhibits the continuous side reactions between the cathode and electrolyte. In this section, the current coating layer is summarized and classified into two types, inorganic and organic surface coating layers.

2.5.1 Inorganic surface coating layers. A carbon coating layer has been widely applied to various cathode materials. The conductive carbon layer coating significantly improves the

electrical conductivity of the cathode, which is beneficial for accelerating electron transfer during the redox reaction. A MnO_x nanorod coating with N-doped carbon nanowalls (MnO_x@N–C) was prepared, and a schematic of the structure is shown in Fig. 8a.[117] The porous N-doped carbon was derived from a metal–organic framework (MOF) of ZIF-8 nanoparticles through a calcination process. The porous framework of the carbon coating layer promoted the reaction kinetics. On the one hand, due to the conductive carbon network, the electronic conductivity was enhanced and the electron transport was accelerated. On the other hand, the porous structure led to abundant ion transport channels, boosting zinc-ion transport. In addition, the dissolution of Mn ions is suppressed because of the carbon coating layer on the cathode surface, which avoids direct contact with MnO_x and aqueous electrolytes. As a result of these merits of porous N-doped carbon, the MnO_x@N–C composite delivers a high capacity of 305 mA h g^{-1} after 600 cycles at 0.5 A g^{-1}. Besides, homemade waste litchi shell-derived mesoporous carbon materials (MCMs) were used to coat α-Mn_3O_4 particles.[118] MCM4 ($W_{MCMs} : W_{KOH} = 1 : 4$) with abundant mesoporous structures provides a large number of channels for zinc-ion storage. MCM4 also enhances the electronic conductivity of the MCM4@Mn_3O_4 cathode and promotes electron transfer. In addition to these composites, other active cathode material coating carbon layers have been widely investigated, including Ni_3S_2/carbon,[119] $(NH_4)_2V_3O_8$/C,[120] $ZnMn_2O_4$@C,[121] N-doped C/V_2O_3,[122] MnO@N–C,[123] and Mn_3O_4@NC.[124]

Other carbon materials, such as graphene, reduced graphene oxide (rGO), and carbon nanotubes (CNTs), have also been combined with cathodes to optimize their electrochemical performance. For example, graphene sheets were used to wrap $H_2V_3O_8$ nanowires (NWs) *via* a simple hydrothermal method and the mass loading of the cathode was approximately 1 mg cm^{-2}.[51] The graphene network intimately surrounds the random NWs (Fig. 8b and c) and provides a large contact area with $H_2V_3O_8$ NWs, which benefits the charge transport kinetics. Graphene also plays an important role in improving the surface area. As shown by the BET result, $H_2V_3O_8$ NW/graphene has a larger surface area (21.5 cm^2 g^{-1}) than pure $H_2V_3O_8$ NWs (14 cm^2 g^{-1}), which increases the contact area between the electrolyte and cathode. In addition, the high specific area of the graphene sheet enhances the capacity due to the capacitive effect. Thus, the composite cathode of $H_2V_3O_8$ NW/graphene delivers a high capacity of 394 mA h g^{-1} at 1/3C, an excellent rate performance of 270 mA h g^{-1} at 20C and outstanding cycling stability (87% capacity retention after 2000 cycles). Besides, graphene combined with CNTs forms a unique three-dimensional (3D) scaffold (rGO/CNT),[125] which was incorporated with one-dimensional (1D) $Na_xV_2O_5 \cdot nH_2O$ (NVO) nanobelts to construct a 3D cross-linked structure. The 3D rGO/CNT architecture accelerates zinc-ion diffusion because of the enhanced contact area between the electrolytes. In addition, the 3D rGO/CNT architecture provides a 3D electron pathway, leading to fast electron transport. 3D rGO/CNT also works as an elastic medium to tolerate the volume change of the active
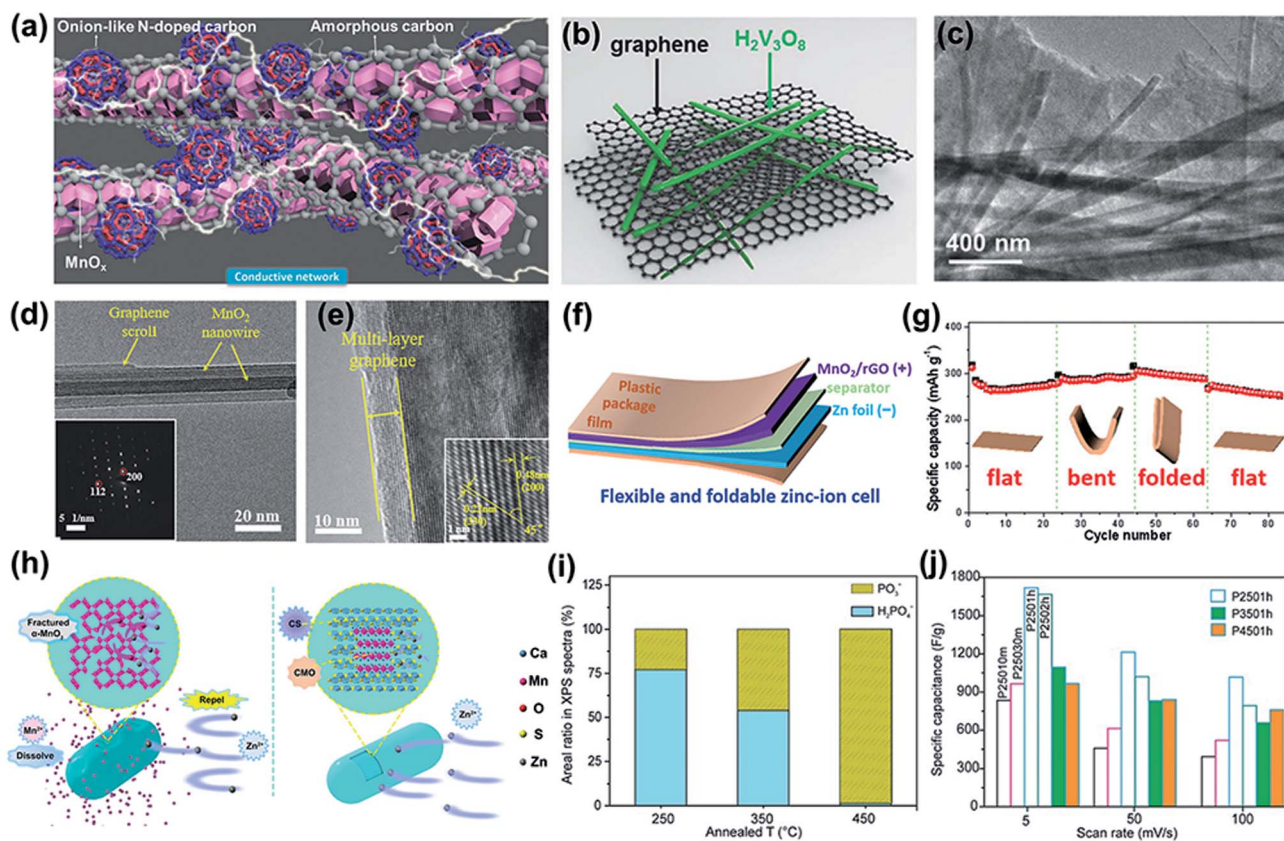
This journal is © The Royal Society of Chemistry 2021

J. Mater. Chem. A, 2021, **9**, 19245–19281 | **19259**

Fig. 8 (a) Schematic of the structure of MnO_x@N−C nanorods. Reproduced with permission.[117] Copyright 2018, Wiley. (b) Schematic illustration of the structure of $H_2V_3O_8$ NW/graphene. (c) TEM image of $H_2V_3O_8$ NWs on graphene films. (b and c) Reproduced with permission.[51] Copyright 2018, Wiley. (d) TEM images and SAED (inset) of α-MnO_2/graphene scrolls. (e) The HRTEM of α-MnO_2/graphene scrolls. (d and e) Reproduced with permission.[126] Copyright 2018, Wiley. (f) Schematic illustration of a flexible and foldable ZIB cell. (g) Cycling stability of the ZIB cell under different mechanical deformations. (f and g) Reproduced with permission.[129] Copyright 2020, Wiley. (h) The battery reaction mechanism schematic diagram of α-MnO_2 and Ca_2MnO_4. Reproduced with permission.[131] Copyright 2019, American Chemical Society. (i) Area% change of $H_2PO_4^-$ and PO_3^- at the surface of PCO as a function of annealed temperature. (j) Specific capacitances of different PCO samples prepared under various conditions as a function of scan rate. (i and j) Reproduced with permission.[132] Copyright 2016, Wiley.

material during Zn^{2+} insertion/extraction, resulting in long-term cycling stability.

Apart from vanadium-based compounds, this strategy has also been applied to manganese-based cathodes. As shown in Fig. 8d, graphene scroll-coated α-MnO_2 nanowires were successfully fabricated.[126] The HRTEM image shows that the thickness of multilayer rGO was 5 nm (Fig. 8e). On the one hand, the rGO coating layers prevent the dissolution of MnO_2 in the aqueous electrolyte during cycling. On the other hand, rGO improves the electronic conductivity of MnO_2 nanowires. Thus, the composite electrode shows an excellent long-term cycling stability (94% capacity retention after 3000 cycles at 3 A g^{-1}) and a high energy density of 406.6 W h kg^{-1} at 0.3 A g^{-1}. Due to its mechanical deformability, light weight, and high electrochemical conductivity,[127] reduced graphene oxide was hybridized with other active materials as a flexible and foldable cathode.[128] As shown in Fig. 8f, a self-standing hybrid membrane consisting of ultralong MnO_2 nanowires and graphene nanosheets was fabricated as a highly flexible and lightweight cathode for ZIBs.[129] The foldable ZIB cathodes

showed no capacity decay when the flexible cell was bent and folded (Fig. 8g).

In addition to the carbon coating layer, other inorganic compounds were also coated on the cathode surface. For instance, rose-like VS_2 nanosheets were coated with a protective layer of VOOH (VS_2@VOOH) *via* a facile hydrothermal method.[130] Hydrophilic VOOH with a thickness of 50–100 nm plays an important role in suppressing the dissolution of vanadium, which acts as a protective layer to separate VS_2 and the aqueous electrolyte. This may be related to the O–H in VOOH, which exchanges with the O–H in water during cycling and keeps the VOOH structure stable. Additionally, electrolyte is beneficial to infiltrate into cathode due to the presence of hydrophilic O–H, which promotes the efficiency of zinc-ion diffusion. Thus, the VS_2@VOOH composite delivers superior cycling stability and exhibits a 91.4 mA h g^{-1} capacity even after 400 cycles even at a high current density of 2.5 A g^{-1} and an 82% capacity retention.

The inorganic compound coating layer can also be generated through an *in situ* electrochemical method. An *in situ* formed

19260 | *J. Mater. Chem. A*, 2021, **9**, 19245–19281

This journal is © The Royal Society of Chemistry 2021

solid electrolyte interface (SEI) layer ($CaSO_4 \cdot 2H_2O$) was fabricated on the Ca_2MnO_4 cathode surface during the charging process.[131] DFT calculations were performed to analyze the properties of the SEI layer. The DOS results reveal that the SEI layer is an electron insulator because its bandgap is 7.2 eV. Moreover, the zinc-ion diffusion energy barrier is only 0.357 eV in the SEI layer, suggesting that the SEI layer also has superior ionic conductivity. As shown in Fig. 8h, the insoluble SEI layer coating on the cathode surface suppresses the dissolution of Mn ions and prevent the crystal structure of the cathode from collapsing. In short, because of the *in situ* generation of the SEI film on the cathode surface, the ion transport kinetics at the interface are improved, the activation energy for zinc ion diffusion is reduced and dissolution is inhibited. This endows the Ca_2MnO_4 cathode with excellent capability and cycling stability, which shows a capacity of 100 mA h g^{-1} and a capacity retention of 80% after 1000 cycles at a current density of 1 A g^{-1}.

Inorganic ion coating has also been exploited to improve electrochemical performance. The modified inorganic ion groups on the cathode surface play an important role in tuning the interfacial properties. For instance, surface-modified phosphate groups ($(H_2PO_4)^-$ and $(PO_3)^-$) have been demonstrated to effectively promote surface reactivity and efficient charge storage.[132] Phosphate-ion-functionalized Co_3O_4 was used for pseudocapacitors. The effect of different contents of the two phosphate groups on the pseudocapacitive performance was analyzed. With an increase in PO_3^-, the specific capacitance decreases while the rate capability increases (Fig. 8i and j). In addition, the electrode with the highest content of $(H_2PO_4)^-$ shows the smallest equivalent series resistance. It was concluded that $H_2PO_4^-$ contributes to fast electron transport and that PO_3^- promotes interfacial redox reactions. Moreover, $Co-OPO(OH)_2$ exhibits a higher degree of covalency than $Co-O$ because $Co-OPO(OH)_2$ shows a higher covalent character (67.7%) than $Co-O$ (54.4%), indicating that the electrons in the 3d orbitals of the Co atom in $Co-OPO(OH)_2$ possess higher energy. Besides, the $Co-OPO(OH)_2$ bond possesses a longer length ($\approx 2.09–2.19$ Å) than the $Co-O$ bond (≈ 1.9 Å). The longer bond and lower electronegativity weaken the attraction of electrons in the 3d orbitals of cobalt ions, which reduces the energy for electrons extracted/obtained during the redox reactions. Thus, the modified phosphate ions enhance the surface reactivity of the cathode and promote electrode kinetics, leading to fast faradaic reactions.

Similarly, cobalt molybdate ($CoMoO_4$) nanosheets with surface-modified phosphate ions ($P-CoMoO_4$) were fabricated *via* a phosphating process,[133] which also introduced oxygen vacancies in the structure and generated CoP nanoparticles on the nanosheets. Due to the modified phosphate ions on the surface, the activation energy of redox reactions is decreased and the reaction kinetics are promoted. The CoP nanoparticles generated *in situ* on the nanosheets enhance the active sites and boost the charge transfer. The electronic conductivity is also enhanced because of the presence of oxygen vacancies. Thus, the optimized $P-CoMoO_4$ cathode shows a higher capacity of 431.4 mA h g^{-1} at a current density of 10 A g^{-1} compared with

$CoMoO_4$ (157.5 mA h g^{-1}), and delivers an outstanding energy density of 679.4 W h kg^{-1} at a power density of 8.6 kW kg^{-1}.

The incorporation of inorganic compounds and inorganic ions was used to modify active materials for ZIBs. For instance, a $P-MoO_{3-x}@Al_2O_3$ cathode was prepared as a cathode for ZIBs *via* unique interfacial engineering.[134] First, α-MoO_3 nanorods were prepared through a hydrothermal method, and then Al_2O_3 was coated on the nanorod surface by atomic layer deposition (ALD) technology. Finally, phosphating treatment was performed to introduce phosphate ions and oxygen vacancies. The unique structural design optimized the electrochemical performance of the electrode. On the one hand, the coated Al_2O_3 as a protective layer suppressed the dissolution of active materials and tolerated the volume variation of the cathode during cycling, resulting in long-term cycling performance. On the other hand, the introduced phosphate ions and oxygen vacancies enhanced the electrical conductivity and promoted surface reactivity. Therefore, the $P-MoO_{3-x}@Al_2O_3$ sample exhibited the highest capacity and best cycling stability compared to the uncoated Al_2O_3 layer ($P-MoO_{3-x}$) and pure MoO_3 samples.

2.5.2 Organic surface coating. Generally, the electrical conductivity of the cathode significantly influences the electrochemical performance. The organic coating layer usually improves the electronic conductivity, but it exhibits relatively moderate ion diffusion compared to the inorganic coating layer.[135] Various polymers have been reported as coating layers on the cathode surface to optimize the electrochemical performance, such as polyfurfural,[136] polyaniline (PANI),[137] polypyrrole (PPY),[138] polydopamine (PDA),[139] poly(3,3'-dihydroxybenzidine) (DHB),[140] poly(3,4-ethylenedioxythiophene) (PEDOT),[141] and poly(styrenesulfonate) (PSS).[142]

Specifically, a V_2O_5 array grown on carbon cloth (CC) was coated with a conductive layer of PEDOT through the electrodeposition method.[141] The HRTEM image shows PEDOT coated V_2O_5 with a thickness of 5 nm (Fig. 9a). V_2O_5 with the PEDOT coating layer realizes a higher capacity retention of 65% compared to $V_2O_5@CC$ (40%) and pure V_2O_5 (7%) when the current density is increased from 0.2 to 20 A g^{-1}. In addition, the $V_2O_5@PEDOT/CC$ composite electrode shows 89% capacity retention after 1000 cycles when cycled at a current density of 5 A g^{-1} (Fig. 9b), which is much higher than the 41% and 11% for $V_2O_5@CC$ and V_2O_5, respectively. The optimized electrochemical performance of the $V_2O_5@PEDOT/CC$ cathode can be ascribed to the following reasons: first, PEDOT acts as a conductive layer to improve the electronic conductivity of V_2O_5, which is beneficial for improving the reaction kinetics. Second, PEDOT works as an active material to improve the capacity of the composite cathode.

In addition to a single polymer, two different kinds of polymers have been used to optimize the electrochemical performance of the cathode material. A PEDOT:PSS film with the addition of 1-ethyl-3-methylimidazolium-hexafluorophosphate ionic liquid ([EMIM]PF$_6$) was coated on a Bi_2S_3 electrode to construct a high-performance zinc-ion battery.[142] The unique film performs several functions in improving the electrochemical performance. First, the PEDOT:PSS film greatly
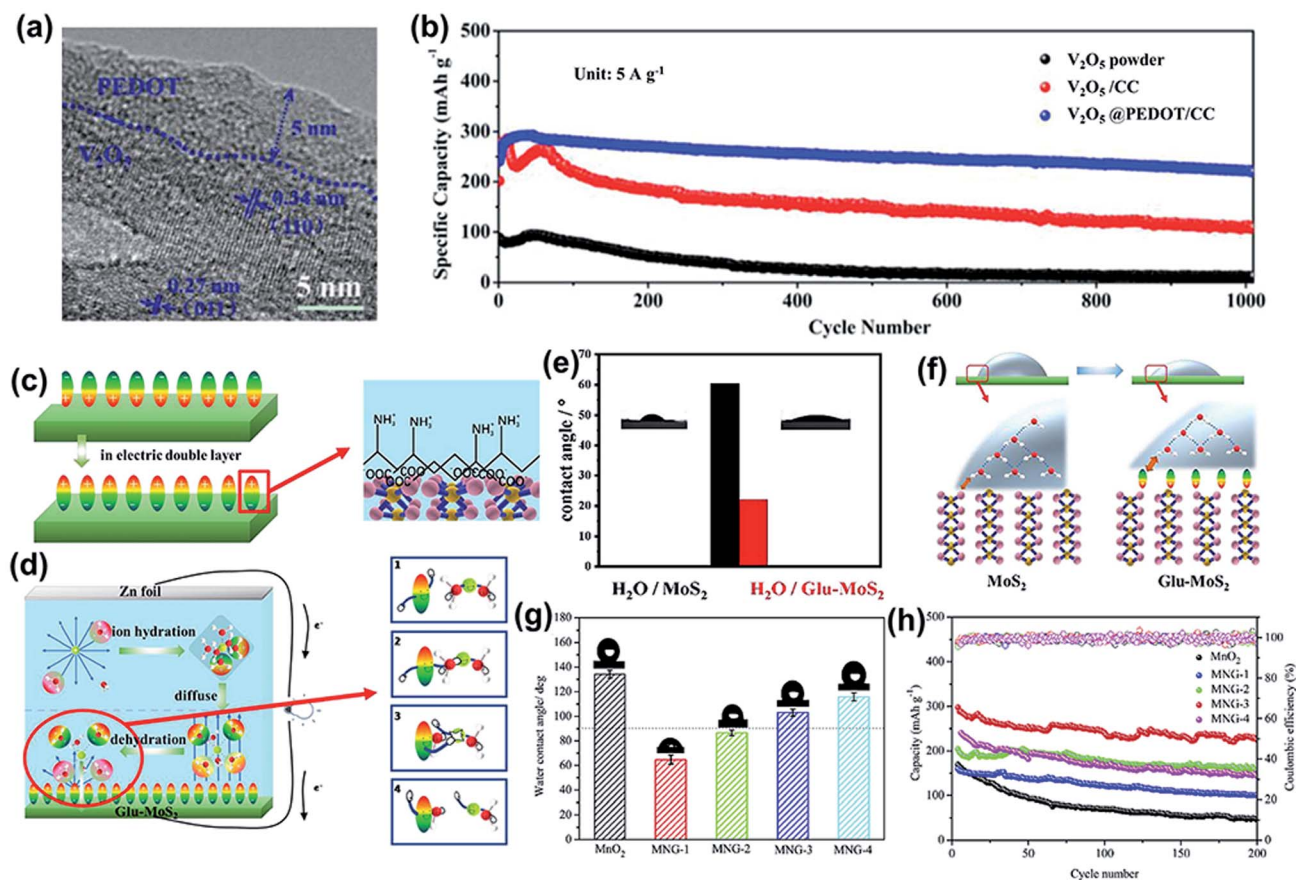
This journal is © The Royal Society of Chemistry 2021

J. Mater. Chem. A, 2021, **9**, 19245–19281 | **19261**

Fig. 9 (a) TEM image of the as-prepared V_2O_5@PEDOT nanosheet arrays. (b) Cycling performances of V_2O_5@PEDOT/CC, V_2O_5/CC, and V_2O_5 powders at 5 A g^{-1} for 1000 cycles. Reproduced with permission.[141] Copyright 2018 Wiley. (c) Schematic diagram of the polar direction of glutamate adsorbed on MoS_2 when the electric double layer is formed. (d) Schematic diagram of zinc-ion hydration, migration and dehydration in a zinc-ion battery using Glu-MoS_2. (e) Water contact angle test of the MoS_2 film and Glu-MoS_2 film. (f) Interfacial tension diagram of MoS_2 and Glu-MoS_2 with water. (c–f) Reproduced with permission.[143] Copyright 2020, Elsevier. (g) Water contact angles of MnO_2 and MNG cathodes before cycling. (h) Cycling performance and corresponding coulombic efficiency of MnO_2 and MNGs at 5C after the activation process at 0.5C. (g and h) Reproduced with permission.[144] Copyright 2020, Elsevier.

increases the cathode conductivity, resulting in accelerated electron transfer upon reaction. Second, the polymer layer prevents the inner Bi_2S_3 grains from pulverizing and alleviates the dissolution of sulfur. Benefiting from the versatile [EMIM] PF$_6$–PEDOT:PSS polymer layer, the modified Bi_2S_3 cathode shows a reversible capacity of 275 mA h g^{-1} at 0.3 A g^{-1}, and excellent long-term cycling stability (95.3% capacity retention for over 5300 cycles).

Apart from the aforementioned polymer layers, another organic coating layer plays a unique role in modulating the dehydration process and improving the wettability between the electrode and electrolyte. Hydrated zinc ions ([$Zn(H_2O)_6$]$^{2+}$) in an aqueous electrolyte hardly intercalate into the host structure because of their large size of 5.5 Å.[103] This means that hydrated zinc ions undergo dehydration during intercalation into the cathode framework. Thus, accelerating the dehydration process is a key factor for boosting the ion migration kinetics. Glutamate possesses –NH_3^+, which can trigger interfacial polarization to catalyze the dehydration of hydrated zinc ions, leading to fast Zn^{2+} intercalation. Thus, glutamate was adsorbed on the

MoS_2 surface (Glu-MoS_2) to improve the electrochemical performance.[143] As displayed in Fig. 9c, there is an electric double layer between the cathode and electrolyte after the cathode and anode form a closed circuit. On the one hand, the –NH_3^+ in glutamate bonds with oxygen ions in hydrated zinc ions (Fig. 9d), pulling water over and accelerating the dehydration process. On the other hand, the electric field of –NH_3^+ weakens the bond between Zn^{2+} and H_2O and reduces the activation energy. The wetting properties of Glu-MoS_2 in water are improved, which shows smaller contact angles than MoS_2 (Fig. 9e and f). This higher hydrophilicity endows the cathode surface with good contact with the electrolyte. Thus, Glu-MoS_2 exhibits a 2.5 times higher specific capacity than pure MoS_2.

In addition to glutamate, cellulose was also applied to modulate the wettability of the electrode. Cellulose nanowhiskers (CNWs) and graphene coated on MnO_2 nanowires were used to investigate the influence of electrode wettability on electrochemical performance.[144] It is difficult for water molecules to infiltrate graphene due to its hydrophobicity. CNWs are amphiphilic compounds, which can be hybridized with

graphene in water. The hydrophobic face of CNWs interacts with the π-conjugated system of graphene, forming a CH–π interaction. As a result, the hydrophilic face of CNWs with many hydroxyl groups is in contact with water. The wettability of the composite cathode can be further turned through changing the ratio of graphene to CNWs. As shown in Fig. 9g, with a decrease in the CNW content from 37.50% (MNG-1) to 16.67% (MNG-2) and then to 6.25% (MNG-3) and 3.85% (MNG-4), the hydrophobicity of the cathode is enhanced. The cycling performance initially increases with an increase in hydrophobicity (Fig. 9h). It was explained that the hydrophobic surface accelerated the desolvation of hydrated Zn^{2+}, promoting the zinc-ion diffusion kinetics. However, the electrochemical performance decreased with a further increase in hydrophobicity, which led to slow zinc-ion transportation and charge transfer.

3. Metal Zn anode

3.1 Issues for the Zn anode

As mentioned above, intensive study efforts have been made on cathode materials *via* structural and defect engineering for high-performance rechargeable aqueous ZIBs.[145–147] Compared with cathodes, Zn metal anodes have attracted increasing attention in the last two years. Although Zn metal anodes can mitigate negative issues to some extent in acidic or neutral electrolytes compared to alkaline electrolytes, they are still plagued by unsatisfactory stability, poor reversibility and a low coulombic efficiency (CE).[7,14] This is mainly caused by the formation of Zn dendrites and water-induced side reactions (including hydrogen evolution and Zn metal corrosion). To achieve high-performance ZIBs, it is essential to construct a stable Zn metal anode. In this section, we concisely summarize the problems with Zn anodes, from the aspects of dendrite formation and side reactions.

3.1.1 Zn dendrite growth.
Zinc dendrite growth is considered the primary challenge for the development of high-performance Zn metal anodes. Zn dendrites inevitably form and grow rapidly in alkaline electrolytes during cycling, which severely reduces the electrochemical performance of ZIBs. Although the growth of dendrites can be moderated to some extent in mild electrolytes, this remains a challenge that cannot be ignored.[148] The reaction mechanisms of Zn metal anodes for ZIBs with neutral aqueous electrolytes such as $ZnSO_4$ involve the reversible deposition/stripping of Zn^{2+}, which can be summarized as follows:

$$Zn \leftrightarrow Zn^{2+} + 2e^-$$
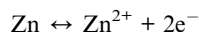
Unfortunately, this process is usually inhomogeneous, mainly related to the uneven current density distribution on the electrode surface. In addition, it is acknowledged that diffusion plays a dominant role during plating. Specifically, Zn^{2+} is primarily adsorbed on the surface of the electrode through two-dimensional (2D) diffusion to accumulate at preferential nucleation sites and form the initial bulge, which increases the partial Zn^{2+} concentration and aggravates the

uneven electric field distribution of the electrode.[149] Subsequent Zn^{2+} tends to reduce at the existing bulge because of the higher curvature and larger surface energy, leading to bulge growth and ultimately evolving into Zn dendrites; this process is recognized as the "tip effect".[148] The "tip effect" induced aggregation of ions drastically reduces the number of nucleation sites, further aggravating the inhomogeneous plating of Zn ions. Thus, the key factors affecting the dendrites are mainly related to the uneven electric field distribution, heterogeneous concentration gradient and unhindered 2D diffusion of Zn^{2+}. To suppress dendrites, reasonable structural engineering of zinc metal anodes has been accomplished, which might shed light on realizing practical rechargeable aqueous zinc-ion batteries.

3.1.2 Water-induced side reactions.
Apart from the growth of zinc dendrites, side reactions have also severely obstructed the electrochemical performance of ZIBs. Side reactions, including Zn metal corrosion and hydrogen evolution, are induced mainly by water molecules in mild electrolytes. The constantly generated hydrogen leads to a low CE and an elevation of internal pressure or even battery explosion. Furthermore, the anode and electrolytes are continuously depleted, leading to unsatisfactory stability and the poor reversibility of ZIBs. In contrast to investigations on Zn dendrite growth, research on the problem of side reactions is still in its initial stages.

Considering that numerous free water molecules are the root cause of corrosion, a thorough understanding of zinc in electrolytes is important to comprehend side reactions. Generally, Zn^{2+} cations are coordinated by six H_2O molecules in neutral aqueous electrolytes, in which Zn ions generally exist in the form of solvated $(Zn(OH_2)_6)^{2+}$ because of the high availability of H_2O molecules.[150] Such cation–solvent interactions have a profound effect on the pH of the resultant solution. The increase in the OH^- concentration owing to H_2 evolution corrosion leads to a local pH increase. Therefore, as the local pH increases, indissoluble by-products, such as ZnO and $Zn(OH)_2$, are formed on the surface of the Zn electrode. In addition, some new reports have shown that by-products are related to the Zn corrosion reaction by generating Zn-based basic salts such as sulfate hydroxide hydrate $(Zn_4SO_4(OH)_6 \cdot xH_2O)$.[151] Different from the compact SEI layer on the Li metal anode, the SEI layer on the zinc anode is loose and unable to effectively prevent the electrolyte from contacting with the surface of the zinc anode. Thus, this loose layer cannot end the corrosion reactions by passivating the anode, so this reaction continues to damage the surface of the Zn electrode and wastes the electrolyte, resulting in an enhanced interphase resistance and limited cycling stability. Another side reaction that plagues the zinc metal anode is the hydrogen evolution reaction. It was discovered that immersing the zinc electrode in the electrolyte without an applied voltage will spontaneously produce hydrogen, and this can be summarized as the following reaction:

$$Zn + H_2O + ZnSO_4 \leftrightarrow Zn_4SO_4(OH)_6 \cdot xH_2O + H_2$$
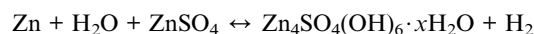
In addition, based on the Pourbaix diagram for Zn in an aqueous environment, the standard reduction potential of Zn/Zn^{2+} (-0.76 V $vs.$ SHE) is much lower than the value of the hydrogen evolution potential (-0.41 V $vs.$ SHE) in a mild neutral electrolyte, illustrating that H_2 evolution is thermodynamically preferred.[152,153] Despite this, the kinetic factors for the hydrogen evolution reaction (HER) should be accounted for when considering HER repression in practical ZIBs, which can be explained by the Tafel equation:

$$\eta = b \log i + \alpha,$$

where η is the overpotential for H_2 evolution, b is a constant called the Tafel slope, and i is the current density. For different metals, b has an almost identical value (~ 0.12 V). Therefore, the overpotential for H_2 evolution is determined mainly by the constant α. Zinc metal has a high H_2 overpotential and a high value of constant α, leading to the inhibition of H_2 evolution on the zinc metal surface under practical circumstances. In addition, the H_2 overpotential is also influenced by other factors, such as the interfacial roughness of the electrode, operating environment and temperature, and zinc ion concentration.

3.2 Current research progress

Significant efforts have been devoted to solving the above-mentioned problems of zinc anodes, and some effective strategies have been developed. In this section, we summarize the significant progress of Zn anodes from a structural engineering point of view. This has been divided into three main categories: surface modification, structural design, and electrolyte optimization.

3.2.1 Surface modification. Planar zinc foil, owing to its easy processing, has become the most widely used zinc anode. However, planar zinc foil has some shortcomings, such as zinc dendrite growth, corrosion and the HER. To alleviate side reactions and inhibit Zn dendrite growth, constructing stable artificial interface layers on zinc electrodes via structural engineering is essential. This is mainly because a stable artificial interface can restrict the direct contact of the electrolyte with Zn metal. Therefore, surface modification strategies are extensively utilized to mediate the zinc interface, accordingly promoting homogeneous deposition and the growth of Zn while inhibiting side reactions. Many materials can be used as modified surface layers, and we have classified them into three categories: metal-modified layers, carbon-based decorated layers, and stable nonconductive layers.

Owing to their strong affinity for zinc and high electronic conductivity, numerous metals can increase the number of nucleation sites to reduce the energy barrier and uniform surface electric field for Zn plating. Many metals possess negative bonding energies with Zn, such as nickel, which exhibits a binding energy of -2.09 eV, and copper, which exhibits a binding energy of -1.58 eV.[154] Thus, Zn atoms preferentially adsorb and bond with metal atoms. These metals can provide uniform nucleation sites for Zn deposition upon cycling. For example, through a facile and easy sputtering strategy, Au nanoparticles coat zinc anodes to induce the

homogeneous deposition of Zn-flake arrays.[155] The Au nanoparticles were uniformly plated on the zinc electrode and served as additional nucleation sites for zinc plating (Fig. 10a and b). The scanning electron microscopy (SEM) images showed that a compact, homogeneous, and flake-like Zn structure was generated on the Au-decorated zinc surface compared to the loose Zn structure on the bare Zn surface. Therefore, the symmetric cell based on the Au-decorated Zn electrode exhibited a much smaller polarization voltage for zinc plating and increased the cycling stability up to 2000 h (Fig. 10c and d). Considering the cost and methods, many reports have focused on nonnoble materials to modify the surface of zinc. For example, indium (In) has been indicated to be a valid coating material for improving the performance of zinc anodes.[151] By a spontaneous replacement reaction, the In layer can be constructed in $situ$ on the surface of Zn foil (Fig. 10e). Owing to In metal having a high HER overpotential and weak chemical activity (-0.338 V $vs.$ the standard hydrogen electrode), it can serve as a corrosion inhibitor. In addition, similar to the Au-decorated Zn layer, Zn atoms will preferentially be deposited on the In layer. That is mainly because In has higher adsorption energy for Zn atoms. The effect of the In layer is that it can inhibit the formation of by-products ($Zn_4SO_4(OH)_6 \cdot 3H_2O$) and guide the homogeneous deposition of Zn. As a result, the symmetric cell using the In-decorated anode can stably cycle for 500 h at a current density of 1 mA cm^{-2}, and for 1500 h at a current density of 0.2 mA cm^{-2}.

Apart from the metal-modified layer, other conductive carbon-based materials, such as rGO,[156] carbon black,[157] MXenes[158] and graphite,[159] have been applied as protective layers. In contrast to the rigid metal layer, the carbon-based layer provides a flexible interface for zinc anodes. Thus, the volume change and surface deformation during Zn plating/stripping can be alleviated. In addition, the large specific surface area of carbon-based materials is conducive to homogeneous zinc plating. Therefore, layer-by-layer rGO on a zinc anode can conspicuously alleviate the growth of Zn dendrites, displaying outstanding cycling reversibility, owing to its large electrochemically active area and reduced local current density.[160] In addition, a simple strategy using pencil drawing graphite on Zn was recently reported (Fig. 10f).[161] The soft graphite interface provides the zinc electrode with a high ionic conductivity and a low Young's modulus, thereby presenting a low polarization voltage, homogeneous electric field distribution and satisfactory durability (Fig. 10g). Therefore, a full cell based on a Zn anode with graphite exhibited prominently enhanced stability for over 200 h with a small polarization voltage of 28 mV and a dendrite-free structure, showing superiority to that of the pure Zn anode.

Constructing a stable nonconductive layer is another likely structural engineering strategy to regulate the electrode interface. Various nonconductive layers, such as $CaCO_3$,[162] TiO_2,[163] ZrO_2,[164] ZnO,[165] ZnF_2,[166] and ZnS[167] have been reported in recent years. For instance, Zhou et al.[165] in $situ$ constructed a 3D nanoporous ZnO layer on a zinc anode through a solution phase deposition strategy. The geometrically optimized oxygen element can induce extra charge density at the interface which
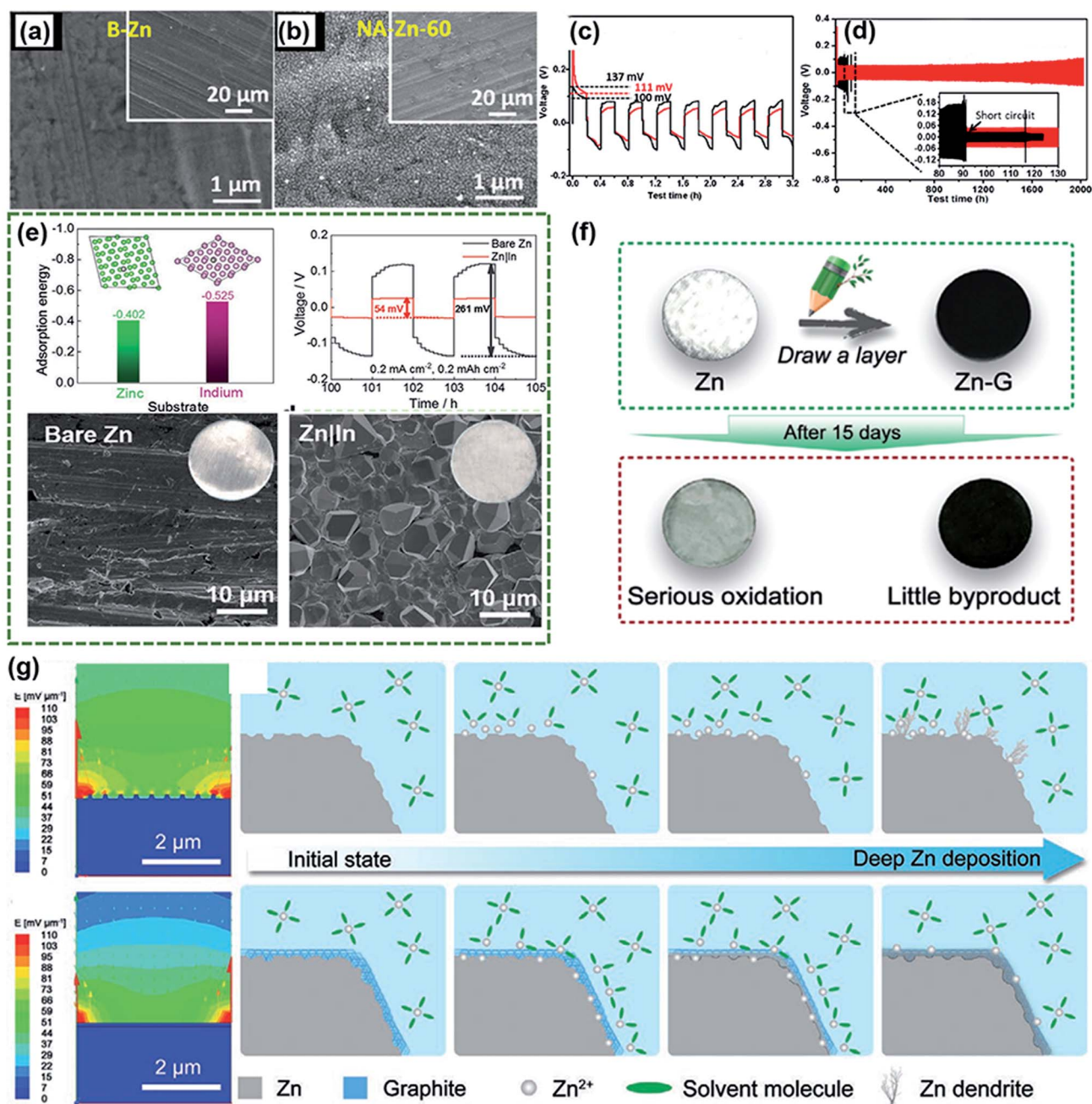
Fig. 10 Typical SEM images of (a) B–Zn and (b) NA-Zn-60; initial (c) and long-term (d) galvanostatic discharge/charge profiles of Zn–Zn symmetrical cells with B–Zn (black lines) or NA-Zn-60 electrodes (red lines). Reproduced with permission.[154] Copyright 2020 American Chemical Society. (e) Adsorption energy of a Zn atom on Zn and In substrates, detailed voltage profiles of bare Zn and Zn|In symmetric cells at cycling times of 100–105 h, and SEM images of bare Zn and Zn|In. Reproduced with permission.[150] Copyright 2020 Wiley-VCH. (f) Schematic illustration of the modification process and the stability in a 2 mol L^{-1} ZnSO$_4$ electrolyte of Zn and Zn–G anodes. (g) The electric field distributions for Zn and Zn–G electrodes. Brief illustration of Zn deposition on Zn and Zn–G electrodes. Reproduced with permission.[160] Copyright 2020 Wiley-VCH.

is proven by DFT calculations (Fig. 11a); moreover, the Zn^{2+} insertion energy barrier for bare Zn is much higher than that for Zn with a ZnO protective layer. The ZnO layer is conducive to electrostatic attraction of zinc ions rather than the solvated zinc ions in the electric double layers, thereby ensuring faster kinetics for Zn^{2+} plating and efficiently impeding hydrogen

evolution. Therefore, the symmetric cell based on the ZnO coated Zn anode shows a zinc utilization of 99.55% and an ultralong cycle life. Additionally, a polyamide (PA) coating was designed to control Zn deposition behavior.[149] The intrinsic dissolved gas and free H$_2$O molecules in the aqueous electrolyte can be effectively restrained, thus prominently impeding zinc

This journal is © The Royal Society of Chemistry 2021

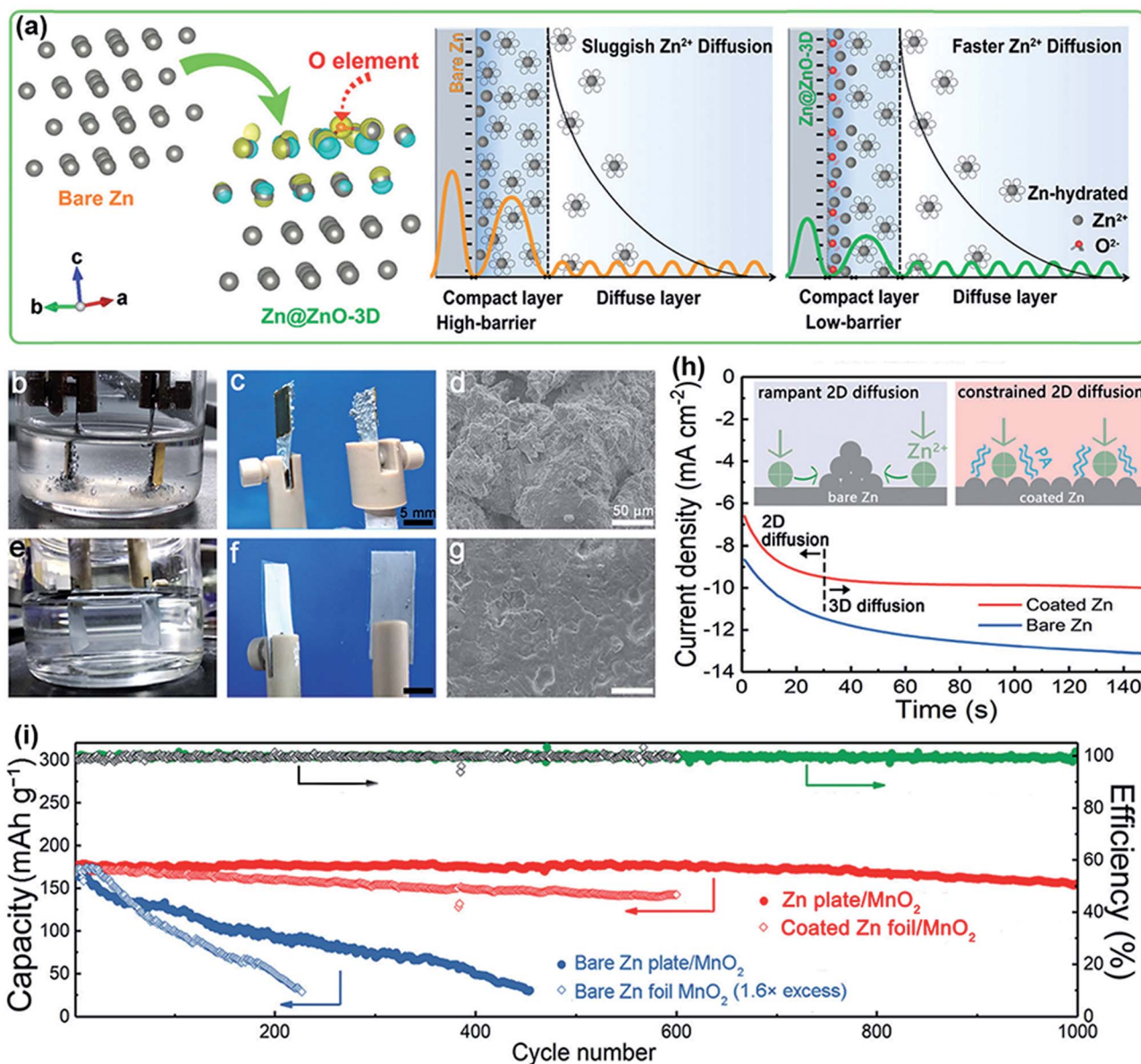J. Mater. Chem. A, 2021, **9**, 19245–19281 | **19265**

Fig. 11 (a) Differential charge density distribution of Zn@ZnO-3D calculated by first-principles calculations. Electric double layer structure in the vicinity of the anode and the corresponding energy barrier. Reproduced with permission.[164] Copyright 2020, Royal Society of Chemistry. Symmetrical Zn cells with (b) bare Zn plates and (e) coated Zn plates assembled in transparent tanks representing the side reactions visually during continuous Zn plating/stripping at a current density of 0.5 mA cm^{-2}. The surface morphology of (c and d) a bare Zn plate and (f and g) a coated Zn plate after 100 cycles. (h) Chronoamperograms (CAs) of bare Zn and coated Zn at a −150 mV overpotential. (i) Cycling performance at a current density of 2C. Reproduced with permission.[148] Copyright 2020, Royal Society of Chemistry.

corrosion and by-product generation. The SEM images and digital photographs show numerous dendrites on the surface of bare Zn after zinc plating, while the Zn with the PA-decorated layer remained smooth and flat (Fig. 11b–g). This is because the two-dimensional (2D) diffusion of zinc ions on the PA-decorated layer is inhibited, resulting in an increase in the number of nucleation sites, which can finally enable a homogeneous zinc deposition (Fig. 11h). Owing to its strong coordination with Zn and an abundant hydrogen bond network, the PA coating layer can effectively protect the Zn anode. The cell based on the PA-coating anode exhibits a CE of 99% and

a capacity retention rate of 88% after 1000 cycles (Fig. 11i). Apart from coating PA on zinc anodes, poly(vinyl butyral) (PVB),[168] polyacrylonitrile (PAN)[169] and Nafion–Zn–X polymer[170] layers can also alleviate the growth of Zn dendrites and inhibit side reactions. Benefiting from the cyano groups (–CN) of PAN and the abundant polar functional groups of PVB, these insulating polymers show high ionic conductivity and good hydrophilicity, resulting in excellent electrochemical performance.

Based on the above discussion, the surface-modifying materials should have the following features. (1) To maintain the integrity of the surface-modifying materials, sufficient

19266 | *J. Mater. Chem. A*, 2021, **9**, 19245–19281

This journal is © The Royal Society of Chemistry 2021

mechanical and physical strength and strong adhesion of the coating layer with Zn foil are indispensable. (2) Surface-modifying materials should exhibit low electrical conductivity and good ionic conductivity to induce Zn plating underneath the modifying layer. Metal materials have a relatively high electrical conductivity, which can easily cause Zn deposition on the upper surface. Thus, conductive metal nanoparticles or layers with porous structures might be essential to induce the homogeneous deposition of zinc ions upon long-term cycling. (3) Surface-modifying materials should regulate interfacial diffusion behavior. For homogeneous electrodeposition, the diffusion of zinc ions at the surface plays a critical role. Notably, 2D random diffusion causes the preferred plating protuber-ance, strengthens the heterogeneous distribution of Zn ions, and eventually causes severe dendrite growth. From this point of view, a stable nonconductive layer can serve as a protective layer to restrict zinc-ion diffusion on the surface. (4) Hydro-phobicity and electrochemical inactivity should be considered to suppress side reactions and limit the direct contact between the electrolyte and Zn anode. Stable nonconductive protective layers have a compact structure that can serve as a physical shield to avoid water molecule close to the electrode/electrolyte interface, and thereby reduce the number of active H_2O mole-cules at the interface. It can be discovered that different surface modification layers can effectively enhance zinc anode proper-ties especially the long-term lifespan. However, most of the surface modification research stays at the small-scale prepara-tion stage. Given the complex synthesis methods and their limited compatibility with existing production processes, surface modification strategies are hardly, at present, applicable on a large scale. Therefore, achieving a simple synthesis method and reducing cost are the next to be focused on.

3.2.2 Structural design. Commercial Zn foil has been widely adopted as an anode in most ZIBs, in which the Zn foil is also directly adopted as a current collector. However, the side reactions of the electrode and electrolyte, as well as the dendrite formation, can cause the ZIBs to experience capacity decay. Rationally designing the internal structure of the Zn electrode is another effective strategy for constructing high-performance zinc anodes. The structural optimization of zinc electrodes can be classified into two categories: 3D zinc anodes and zinc alloy anodes.

Designing a 3D porous structure to increase the surface area of the zinc anode is an effective strategy for mitigating the problems of zinc electrodes. For example, a 3D monolithic zinc sponge anode was constructed to reduce the local current density. However, this type of pure zinc skeleton structure may eventually wear out and collapse during cycling owing to the lack of a collector.[171] Therefore, to improve the stability of the 3D skeleton, the selection of a current collector is of great importance, given the significance of the energy and power density in the industrial application of ZIBs. Metal materials (e.g. Cu mesh,[154] Cu foam,[172] and porous Cu skeleton[173]), carbon-based materials (e.g. carbon cloth (CC)[174] and graphene foam[175]), and metal–organic framework (MOF)-based materials (ZIF-8)[176] can serve as collectors for building 3D zinc electrodes. These current collectors are promising because of their

excellent physical and electrochemical stability, high ionic and electronic conductivity, strong mechanical strength to adapt plating, and strong affinity for zinc deposition. For instance, a 3D Cu mesh was utilized as a skeleton to support zinc (Fig. 12a–c).[154] The 3D Cu mesh supported zinc anode enables homogeneous Zn plating/stripping, resulting in outstanding cycling stability, decreased voltage hysteresis, and nearly 100% CE. In addition, a carbon nanotube (CNT) structure for zinc plating has been constructed,[174] and the flexible 3D Zn/CNT electrode enables a low polarization voltage (27 mV) and stable cycling performance with a high coulombic efficiency of 97.9%. This is because of the uniformly distributed electric field and the low nucleation overpotential (Fig. 12d). Although a pure carbon cloth collector can provide a 3D porous skeleton, a conspicuous weakness of the carbon collector is the weak binding interaction with Zn, which is not conducive to the plating kinetics and homogeneously distributed electric field. Therefore, optimizing the zincophilicity of carbon-based mate-rials is a promising strategy. A tin (Sn)-modified 3D carbon felt host (SH) was reported for Zn deposition (Fig. 12e).[177] The Sn component can be regarded as an extra nucleation site and provide a lower nucleation overpotential for zinc plating, thereby inducing the homogeneous plating of zinc. In addition, Sn can provide a higher hydrogen evolution overpotential owing to the good chemical inactivity of Sn metal. Furthermore, DFT calculations show that Sn has a stronger adsorption energy for Zn atoms than Ti, Ag, and C (Fig. 12f), resulting in a reduced plating overpotential of Zn, an increased HER overpotential and an improved cycle life at different current densities. In addition to current carbon-based current collectors, ZIF-8, in which ZnN_4 tetrahedral units are bridged through imidazolate linkers to form a 3D structure with large cages interconnected via small six-membered ring apertures, has been illustrated as a collector for highly reversible and highly stable Zn deposition.[176] After heat treatment, the inherent porous structure was well main-tained without change and the Zn^{2+} in the framework is con-verted into Zn^0 with a homogeneous distribution. Note that the trace amount of Zn^0 provides homogeneous nucleation sites for zinc deposition, and the high overpotential for the HER restricts the consumption of electrolytes during cycling. The zinc plating morphology on the ZIF-8 is consistently glossy and compact, even at a higher current density and areal capacity. The zinc deposition mechanism is illustrated in Fig. 12g, where the initial Zn deposition occurs in and on the vacancies of ZIF-8 and the uniform zinc nucleation center results in subsequent dendrite-free deposition.

Another way to optimize the zinc structure is to fabricate zinc alloys. Zinc corrosion is controlled mainly by the HER process, and zinc alloys have a higher hydrogen evolution overpotential, which can generally improve corrosion resistance. In addition, the electrochemical activity of zinc can be improved by alloying. Various zinc-alloyed metals, such as Zn–Cr,[178] Zn–Ni,[179] Zn–Hg,[180] Zn–Pb,[181] Zn–Sn,[182] and Zn–Cu,[183] have been reported. For example, zinc–aluminum (Zn–Al) alloys have been reported to optimize zinc anode performance.[184] Zn–Al alloys with a lamellar structure are prepared by a facile metallurgical procedure, and the components of the alloy can be

This journal is © The Royal Society of Chemistry 2021

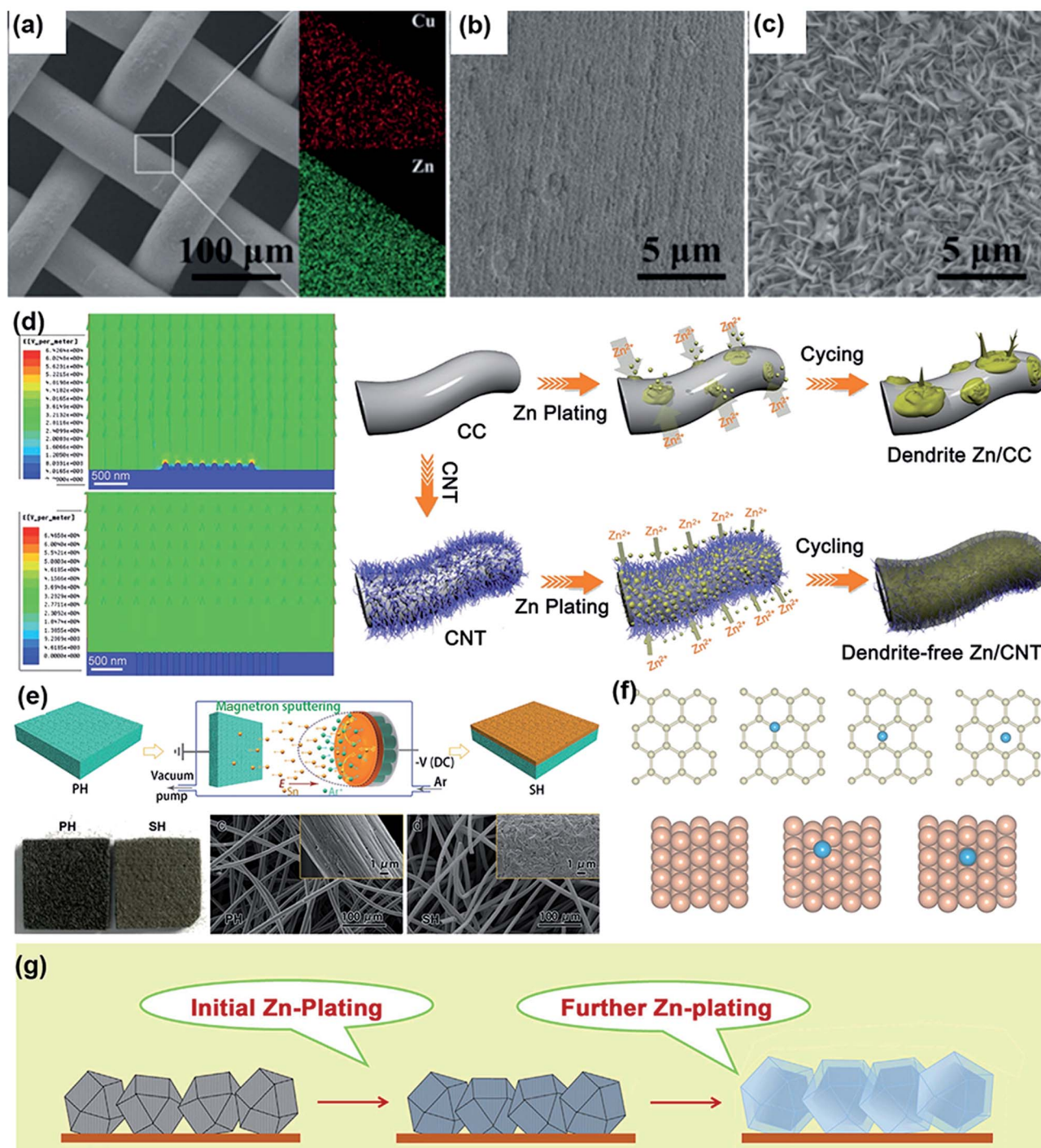*J. Mater. Chem. A*, 2021, **9**, 19245–19281 | **19267**

Fig. 12 (a) SEM image and the corresponding EDX mapping of the three-dimensional dendrite-free zinc anode. Morphology comparison of the zinc anodes synthesized (b) with PAM and (c) without PAM. Reproduced with permission.[153] Copyright 2020 Wiley-VCH. (d) Models of the electric field distributions for a Zn/CC electrode and a Zn/CNT electrode after Zn nuclei formation and the schematic illustrations of Zn deposition on CC and CNT electrodes. Reproduced with permission.[173] Copyright 2020 Wiley-VCH. (e) Schematic illustration of the fabrication process of SH and the digital photograph and SEM images of the morphology of PH and SH. (f) Adsorption energy of carbon and Sn. Reproduced with permission.[176] Copyright 2020 Wiley-VCH. (g) Schematic illustration of the Zn plating. Reproduced with permission.[175] Copyright 2020 Elsevier.

manipulated. The appropriate content of Al not only *in situ* forms stable interlamellar Al/Al$_2$O$_3$ during Zn stripping and conversely induces the subsequent growth of Zn but also ensures that the Zn lamellae do not transform to irreversible by-products such as ZnO and Zn(OH)$_2$. As a result, the eutectic Zn$_{88}$Al$_{12}$ (at%) alloy anode displays excellent electrochemical performance, with ultra-long cycling stability, a small polarization voltage and a high CE. Moreover, the full cell based on

19268 | *J. Mater. Chem. A*, 2021, **9**, 19245–19281

This journal is © The Royal Society of Chemistry 2021

eutectic alloys with the K_xMnO_2 cathode exhibits a capacity retention of almost 100% after 200 cycles and presents an energy density of 230 W h kg^{-1}. The remarkable electrochemical performance of the eutectic $Zn_{88}Al_{12}$ alloy electrode demonstrates that the rational manipulation of the zinc alloy component and interlayer structure is important for obtaining desirable effects. In addition, Zn–Ni alloys with strong zinc affinity were proven to be effective in restraining the growth of Zn dendrites by guiding the form of deposition.[179] This alloy was formed by adding a certain amount of nickel bi(trifluoromethylsulfonate) (Ni(TfO)$_2$) into a Zn(TfO)$_2$ electrolyte, which thoroughly changed the hexagonal nanosheet morphology into a nanoparticle morphology in the deposition process. Besides, a 3D Zn–Cu alloy with a regulated porous structure was constructed by a simple electrochemical treatment.[183] The 3D porous structure ensures quick electron transfer and ion transport, which are conducive to homogeneous deposition/stripping behavior and thereby increase the reversibility and stability of batteries.

Structural engineering can effectively reduce the local current density and optimize the zinc plating morphology. However, 3D substrates are likely to collapse or be damaged in practical applications; furthermore, their increased production costs and difficult preparation process may reduce their production efficiency. In addition, 3D substrates with high surface areas may reduce the overpotential and facilitate the hydrogen evolution reaction. Therefore, in the next step of structural design engineering, these are the key points that need to be focused on.

3.2.3 Electrolyte optimization.

Interface chemistry plays a vital role in determining the electrochemical features and ion transport kinetics in ZIBs. The *in situ* formed interface on a Zn anode is largely related to the reaction between the electrolyte and Zn surface. A perfect electrolyte is expected to display a stable electrochemical window within the operating voltage range and accomplish a reversible Zn deposition/stripping. Therefore, in addition to zinc anodes, aqueous electrolytes are another vital element to be discussed. Since the emergence of rechargeable ZIBs, most anodes have been studied in the $ZnSO_4$ electrolyte. However, ZIBs using the $ZnSO_4$ electrolyte are insufficient for satisfying practical requirements, because zinc anodes suffer from serious irreversibility problems. From this point of view, it is highly acceptable to optimize the present electrolyte to solve the issues that have continuously bothered zinc anodes. In this section, we discuss and review the optimized electrolytes that have been reported to date in regard to two aspects: electrolyte additives and high-concentration electrolytes.

The effect of a variety of electrolyte additives on zinc plating behavior, such as metal cations, has been extensively investigated. It has been indicated that adding an adequate amount of $MnSO_4$ into the $ZnSO_4$ electrolyte not only is conducive to forming a stable electrolyte interface but also inhibits the dissolution of the MnO_2 cathode.[63] Similarly, the addition of Na_2SO_4 can suppress the dissolution of the NaV_3O_8 cathode and induce a dendrite-free zinc deposition layer (Fig. 13a–c).[185] During zinc plating, Na$^+$, which has a lower reduction potential

than Zn^{2+}, tends to form a positively charged electrostatic shield layer, prompting zinc ions to be absorbed in the adjacent areas rather than at the initial bulge. In addition, some polar organic solvents can be adsorbed on the zinc electrode surface and modify the interfacial electrochemical process. For example, an appropriate amount of diethyl ether (Et$_2$O) additive is introduced into a 3 M Zn(CF$_3$SO$_3$)$_2$ electrolyte to improve the cycling stability of ZIBs. When 2 vol% Et$_2$O is applied to a 3 M Zn(CF$_3$SO$_3$)$_2$ electrolyte, the polar Et$_2$O molecules tend to be adsorbed on the initial peaks of the bulge. Therefore, the electrostatic shield works as a protective layer and guides zinc ion diffusion to the uniform surface which are obscured by adsorbed Et$_2$O.[186] As a result, the tip effect is extremely undermined, forming a smooth zinc deposition surface (Fig. 13d). Besides, the addition of an ethylene glycol (EG) additive, a representative dihydric alcohol, was adopted to stabilize Zn electrochemistry.[187] The Zn^{2+} coordination environment was adjusted with different EG concentrations in the H$_2$O/EG hybrid electrolyte. High-EG-content electrolytes inhibit the diffusion of Zn^{2+} and occurrence of side reactions during cycling and enhance the overpotential for Zn deposition (Fig. 13e).

Furthermore, unlike the compact SEI layer on the lithium metal anode, the SEI layer between the Zn anode and electrolyte is loose and unable to effectively prevent the electrolyte from contacting with the surface of the zinc anode. Thus, this loose layer is unable to end the corrosion reactions by passivating the anode. Therefore, through a reasonable electrolyte design strategy, constructing a stable SEI layer on the anode surface is a valid strategy to enhance the properties of ZIBs. Recently, by simply adding a trace amount of Zn(H$_2$PO$_4$)$_2$ salt into the Zn(CF$_3$SO$_3$)$_2$ electrolyte, a strong and highly Zn^{2+}-conductive hopeite SEI layer was constructed *in situ* (Fig. 13f).[188] Through directing uniform zinc deposition/stripping and inhibiting the persistent consumption of the electrolyte and electrode during cycling, this conductive SEI layer can provide a stabilized interface. In addition, the conductive SEI layer can also conspicuously enhance the cycling stability of full batteries under practical conditions, including a lean electrolyte, and limited zinc excess. Additionally, by introducing a 20 mM Zn(NO$_3$)$_2$ additive into an aqueous 3 M Zn(OTF)$_2$ electrolyte, a strong inorganic ZnF$_2$–Zn$_5$(CO$_3$)$_2$(OH)$_6$–organic SEI layer was chemically formed (Fig. 13g).[189] First, a thin and dense Zn$_5$(OH)$_8$(NO$_3$)$_2\cdot$2H$_2$O passivation layer upon contact with Zn and the electrolyte was formed. Then, the Zn$_5$(OH)$_8$(NO$_3$)$_2\cdot$2H$_2$O passivation layer gradually converts into a more stabilized zinc-ion conductive Zn$_5$(CO$_3$)$_2$(OH)$_6$ layer *via* a metathesis reaction. Meanwhile Zn^{2+}-conductive organic and ZnF$_2$ layers were constructed from the reaction between (CF$_3$SO$_3$)$^-$ and NO$_3^-$ in the outer and inner parts respectively. The extremely soft organic layer prevents the SEI from cracking because of charge transfer and promotes the migration of solvated Zn ions. The hydrophobic ZnF$_2$ inner layer further removes active water molecules and inhibits the decomposition of H$_2$O and formation of zinc dendrites by avoiding the direct contact of zinc with water. This unique SEI increases the zinc anode deposition/stripping CE to 99.8%, and the full cell coupled with MnO$_2$ exhibits high cycling stability with an almost 100% capacity retention rate for 700
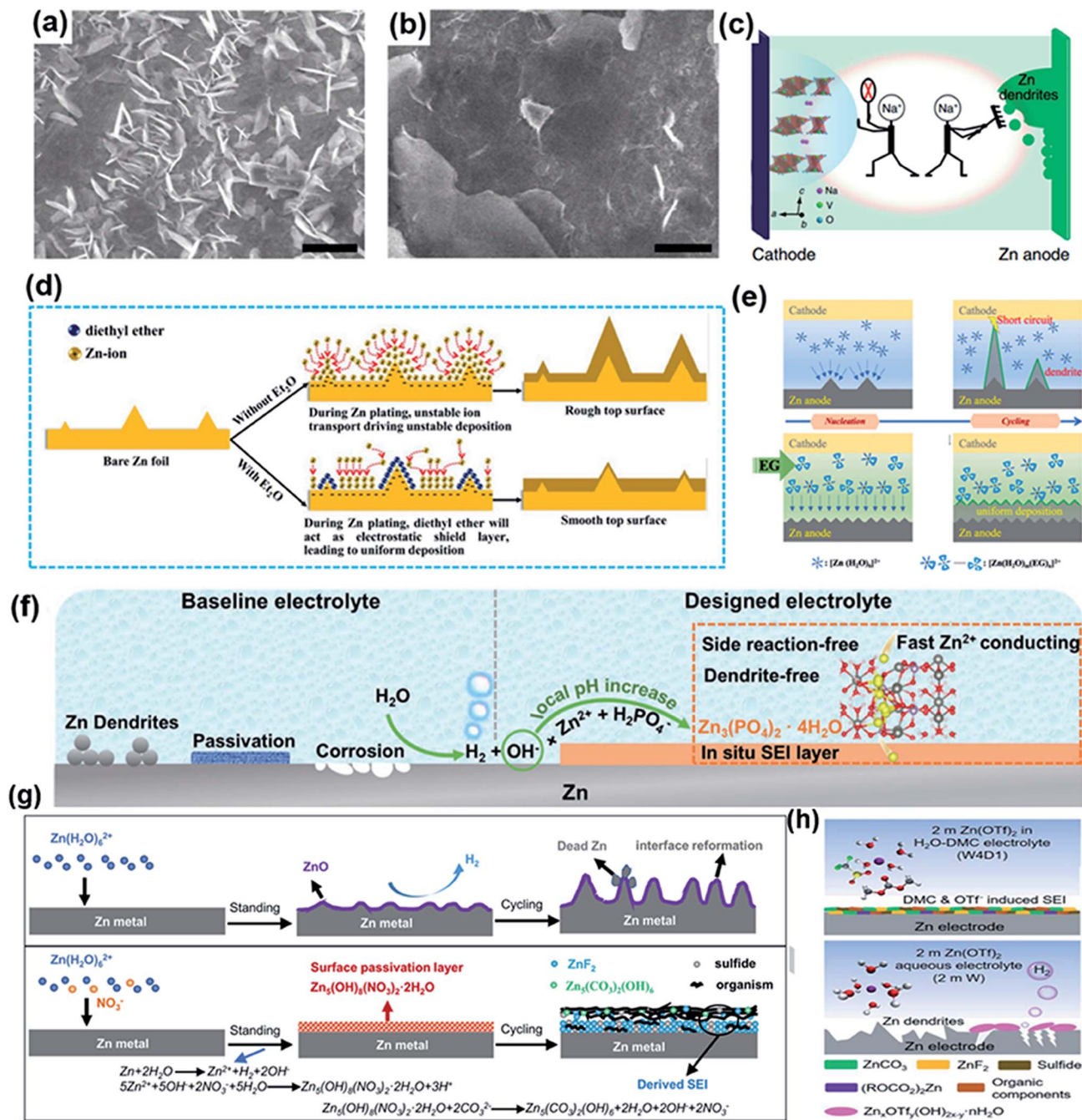
This journal is © The Royal Society of Chemistry 2021

J. Mater. Chem. A, 2021, **9**, 19245–19281 | **19269**

Fig. 13 SEM images of the Zn anode surface after 500 cycles in (a) ZnSO$_4$ and (b) ZnSO$_4$/Na$_2$SO$_4$ electrolytes. (c) Schematic diagram: Na$_2$SO$_4$ additive suppresses the dissolution of NVO nanobelts and the formation of Zn dendrites. Reproduced with permission.[184] Copyright 2018 Nature Publishing Group. (d) Schematics of morphology evolution for Zn anodes in a mild aqueous electrolyte with and without the Et$_2$O additive during Zn stripping/plating cycling. Reproduced with permission.[185] Copyright 2019 Elsevier. (e) Schematic illustration of dendrite inhibition of H$_2$O/EG hybrid electrolytes. Reproduced with permission.[186] Copyright 2021 Elsevier. (f) Schematic illustration of Zn surface evolution and the SEI formation mechanism. Reproduced with permission.[187] Copyright 2021 Wiley-VCH. (g) Illustration of the surface evolution mechanism. Reproduced with permission.[188] Copyright 2021 Wiley-VCH. (h) Schematic illustration of the surface chemistry on the Zn electrode in W4D1 and 2 m W electrolytes. Reproduced with permission.[189] Copyright 2021, Royal Society of Chemistry.

cycles. Furthermore, the addition of an organic dimethyl carbonate (DMC) in Zn(OTf)$_2$ allowed the formation of a ZnF$_2$–ZnCO$_3$-rich SEI layer,[190] and adding dimethyl sulfoxide (DMSO) to the ZnCl$_2$ electrolyte can *in situ* form a compact and self-repaired Zn$_{12}$(SO$_4$)$_3$Cl$_3$(OH)$_{15}$·5H$_2$O–ZnSO$_3$–ZnS SEI on the

surface of zinc electrodes (Fig. 13h).[191] Compared with the loose Zn$_4$(OH)$_6$SO$_4$·xH$_2$O by-product layer formed by Zn corrosion, these dense SEI layers can effectively end the corrosion process by reacting with the fresh surface through the passivated layer. However, excess additives tend to increase the polarization

19270 | *J. Mater. Chem. A*, 2021, 9, 19245–19281

This journal is © The Royal Society of Chemistry 2021

voltage and interfacial resistance, resulting in reduced electrical conductivity of the anode. Therefore, a balance must be found between the additive content and electrode conductivity.

In addition to the addition of electrolyte additives, another effective method is to construct highly concentrated electrolytes. The solvation-sheath structure of the Zn^{2+} ion closely determines the cycling stability and reversibility of the Zn electrode. In neutral aqueous electrolytes, solvated $(Zn(OH_2)_6)^{2+}$ is formed by zinc ions interacting with six H_2O molecules, resulting in a high energy barrier for the desolvation of solvated $(Zn(OH_2)_6)^{2+}$ during zinc deposition. Enhancing the concentration of the electrolyte is a significant strategy to mitigate the solvation effect by decreasing the number of water molecules around zinc ions. Besides, the active water molecules on the surface of the Zn electrode are the decisive cause of side reactions. Thus, to increase the depth of discharge (DOD) and CE of the Zn anode, the strategy of constructing highly concentrated electrolytes is widely adopted. The first inspiring report of ZIBs with high-concentrated electrolyte was constructed by 1 M $Zn(TFSI)_2$ and 20 M LiTFSI.[192] As shown in Fig. 14a, molecular dynamics studies have verified that a highly concentrated electrolyte can transform the solvation sheath structure of zinc ions. In a dilute electrolyte, the zinc ions are coordinated with six H_2O molecules. When the LiTFSI concentration is increased to 20 M, H_2O molecules are entirely replaced by $TFSI^-$ ions. This special structure effectively mitigates the growth of dendrites and alleviates water-induced side reactions, thereby promoting excellent cycling stability and an almost 100% CE. The highly concentrated electrolyte benefits from this solvation sheath structure in battery systems, accelerating the progress of aqueous ZIBs for industrial applications. Inspired by this breakthrough, Ji *et al.* employed this method with a $ZnCl_2$ electrolyte.[193] A similar solvation structure can reasonably explain the increased cycling stability and plating/stripping reversibility of the Zn anode. However, considering the issues of cost, high concentration electrolytes are severely limited in their practical application. Therefore, through reasonable structural design, constructing a high-concentration electrolyte on an electrode surface may solve this problem. Recently, a MOF material was coating on the surface of a zinc anode to construct a super-saturated electrolyte.[194] Owing to the unique and regular structure of the MOF (size of approximately 2.94), the $ZnSO_4$ electrolyte presents a super-saturated coordination structure by removing H_2O molecules inside the MOF channels (Fig. 14b and c), which is impossible to form in a saturated electrolyte. Owing to the super-saturated configuration, the symmetric Zn–Zn cells based on a MOF-coated Zn anode provided a long-term cycling stability up to 3000 h at 0.5 mA cm^{-2}, and the full cell coupled with a MnO_2 cathode maintained a reversible capacity of 180.3 mA h g^{-1} after 600 cycles. In addition, a well-tailored nanopore structure on the Zn anode can also enable the local increase of the concentration of the electrolyte (Fig. 14d).[195] The interface-localized concentrated electrolyte could be achieved *via* the space charge effect in the accurately constructed nanopore. Therefore, the symmetric Zn–Zn cell using the nanopore Zn anode exhibited an ultra-long term cycling stability and a high reversibility for 750 h, and

the full cell coupled with $NaVO_3$ enabled an essentially stable cycling stability.

By optimizing the electrolyte, the growth of dendrites and gas evolution can be alleviated at the molecular level, thus realizing a Zn anode with a long lifespan. However, the current research on electrolyte optimization strategies is still in its infancy, and many of the reaction mechanisms and the solvation structures are still indistinct. Furthermore, the relatively low zinc ion conductivity caused by additives is a severe challenge. Therefore, designing novel electrolytes and investigating more electrolyte additive types are the trends of future electrolyte optimization.

4.   Characterization techniques

Advanced characterization techniques are of great significance for conducting a multidimensional analysis of aqueous ZIBs, such as the morphological structure, phase transition, crystal structure evolution, and chemical composition. Comprehensive characterization analyses contribute to the understanding of the reaction process and guide the design of advanced ZIBs. In this section, the characterization techniques for investigating the structure and morphology of ZIBs at multilength scales are summarized.

4.1   *Ex situ* structural characterization techniques

The techniques used to investigate the detailed structural evolution upon cycling are of great significance in deeply understanding the energy storage mechanisms and optimizing the structural design. The characterization of structural changes in cathode materials during repetitive ion insertion and extraction helps clarify the factors influencing the electrochemical performance, such as the volume variation, phase evolution, and side reactions. Besides, monitoring the structural evolution of the anode surface is essential to investigate the growth of dendrites during Zn deposition and exfoliation processes.

4.1.1   Conventional XRD, Raman spectroscopy and XPS techniques. Cathode materials and Zn anodes are usually chemically stable in an air atmosphere. Thus, it is more convenient to characterize structural changes with fewer restrictions. XRD, established on the constructive interference of monochromatic X-rays and crystalline samples, is a powerful tool to investigate the phase composition and crystal structure transformation. For example, the structural changes (interlayer spacing or phase evolution) of cathode materials after the intercalation of guest ions or defects into their crystal structure can be studied using XRD. Raman spectroscopy is a common technique to analyze the chemical environment of materials, which is based on the Raman effect between the incident monochromatic laser and the bonds of molecules in the sample. The different Raman shifts correspond to certain vibrational modes of the molecules or crystals. Thus, the structural changes of the electrodes during electrochemical cycling can be revealed by Raman spectroscopy. XPS analysis is an effective technique to analyze surface chemical
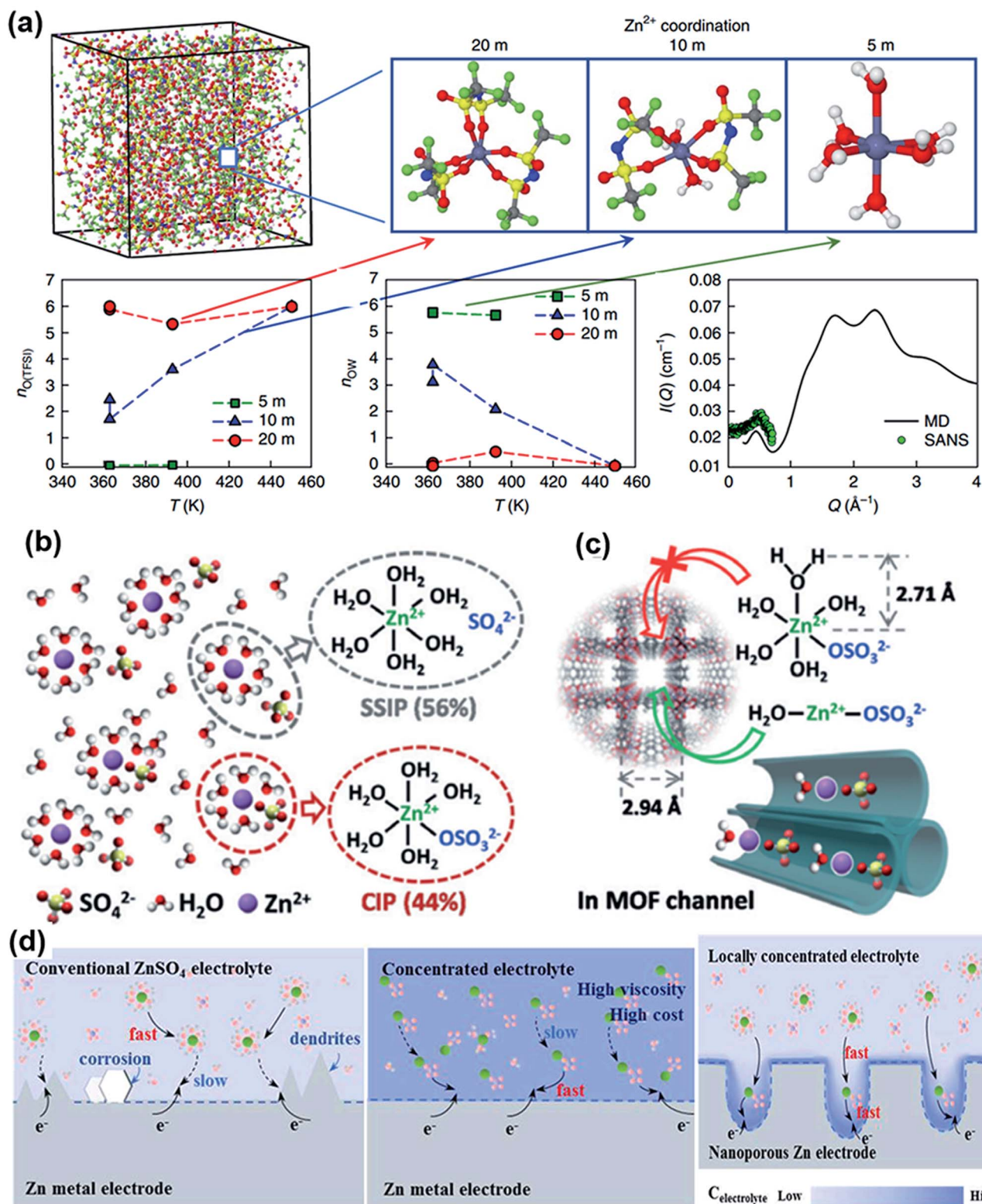
This journal is © The Royal Society of Chemistry 2021

J. Mater. Chem. A, 2021, **9**, 19245–19281 | **19271**

Fig. 14 (a) MD studies of the Zn^{2+}-solvation structure. Reproduced with permission.[191] Copyright 2018 Nature Publishing Group. (b) Two solvation structures in saturated (3.3 m) $ZnSO_4$ aqueous solutions; (c) schematic illustration of highly coordinated ion complexes of $H_2O–Zn^{2+}\cdot OSO_3^{2-}$ migrating through MOF channels. Reproduced with permission.[193] Copyright 2020 Wiley-VCH. (d) Schematic illustration of Zn plating processes on a Zn metal electrode with a conventional $ZnSO_4$ electrolyte, a Zn metal electrode with a concentrated electrolyte, and a nanoporous Zn electrode with an interface-localized concentrated electrolyte. Reproduced with permission.[194] Copyright 2021 Elsevier.

environments, including the valence state of elements and the elemental content. The valence of cathode materials changes during the redox reaction process. Thus, it is essential to analyze the elemental valence of the cathode and further clarify the mechanism of zinc-ion (de)intercalation.

4.1.2 X-ray absorption fine structure spectroscopy (XAFS). Compared with XPS, XAFS has a better accuracy. XAFS is a powerful method for structural analysis at the atomic and molecular scales and includes two parts: X-ray absorption near-edge structure (XANES) and extended X-ray absorption fine-structure spectroscopy (EXAFS). Recently, XAFS has been applied to study the localized chemical information and electronic structure of electrodes for aqueous ZIBs. For example, porous δ-$Ni_{0.25}V_2O_5 \cdot nH_2O$ has been reported as a cathode for high-performance aqueous ZIBs.[189] XAFS was performed to analyze the local chemical and electronic environment during the zinc-ion insertion/extraction process. The Ni L-edge near edge X-ray absorption fine structure (NEXAFS) spectra showed two absorption peaks corresponding to spin–orbital splitting, as shown in Fig. 15a. Peak B shifted toward a higher energy in the discharge state, suggesting that the p–d charge transfer energy Δ increased and the d–p hybridization strength decreased. This is related to the insertion of zinc ions, which bonded with oxygen atoms and withdrew the electrons of O. In addition, as shown in Fig. 15b, the two peaks at 515–520 eV and 520–528 eV are ascribed to V $2p_{3/2}$ and V $2p_{1/2}$, and the peak at 527 eV corresponds to the O K-edge. The absorption features of V $2p_{3/2}$ in the discharged state are weaker than those of the pristine and charged samples, indicating that vanadium was reduced during the discharging process. Besides, there was a small peak at 511.2 eV in the discharged sample, which was related to the second-order absorption feature of the Zn L_3-edge. These results demonstrated the successful intercalation of zinc ions.

XAFS analysis was also successfully applied to investigate Zn dendrite deposition and dissolution through the surface-induced effect of porous silicon structures. The XANES and EXAFS spectra of Zn both showed that at pH = 3, 4, and 5 the chemical state of the deposits at early deposition times (20 s) could not be assigned to ZnO or Zn.[196] To investigate the evolution of Zn deposition at different pH and deposition times, the Fourier transform (FT) of the EXAFS spectra was analyzed. Regardless of the pH value, the content of metallic Zn increased as the deposition time increased. The content of ZnO decreased as the pH value increased, and the content was negligible if the value was 5. In addition, the content of ZnO was the highest at the lowest pH and shortest deposition time.

4.2 *In situ* structural characterization techniques

In situ characterization techniques, which do not require the disassembly of cells, can more reliably reveal the structural evolution of the electrode in real time. Besides, the *in situ* characterization means that it is conducted when the cell is in operation. Thus, these techniques can precisely investigate the relationship between the electrode and electrolyte environment.

4.2.1 In situ XRD. Compared with *ex situ* XRD, *in situ* XRD can monitor the crystal structure evolution of the running

cathode in real time. Fig. 15c shows the *in situ* XRD patterns of α-MnO_2 and the corresponding galvanostatic discharge/charge profile during the first cycle.[197] Some new diffraction peaks at approximately 8.1°, 16.3°, 24.4°, 26.2°, and 33.1° appeared and gradually strengthened when fully discharged to 0.9 V. The results indicate that a new phase is generated during the discharge process, which corresponds to zinc hydroxide sulfate ($[Zn(OH)_2]_3ZnSO_4 \cdot 5H_2O$). However, the intensity of these new diffraction peaks continuously weakened and disappeared when charged back to 1.8 V, suggesting that the generated new phase is reversible during cycling. In addition, *operando* synchrotron XRD was also applied to analyze the phase transition of the NaV_3O_8 cathode during zinc ion insertion/extraction (Fig. 15d).[198] The peaks of the NaV_3O_8 cathode shifted to lower angles when Zn^{2+} was intercalated into the crystal structure. The peaks completely recovered to those of the original cathode structure after Zn^{2+} extraction. Besides, the crystal structure maintained high reversibility during the second cycle. Some new peaks corresponding to $Zn_5(OH)_8(CF_3SO_3)_2 \cdot xH_2O$ appeared after discharging to 0.3 V and disappeared after charging to 1.5 V, suggesting that the new phase was reversibly deposited and dissolved during cycling.

In addition to the cathode, *in situ* XRD characterization techniques were also used to monitor the evolution of the Zn anode. The peak intensity map of the XRD patterns shows two obvious diffraction peaks corresponding to the (112) and (201) crystal planes of Zn metal during the first reduction process, which gradually weaken and disappear after the first oxidation.[199] Furthermore, the (210), (114), (212) and (105) diffractions of ZnO are generated. In the subsequent secondary reduction process, the ZnO peaks disappear, accompanied by the appearance of metallic Zn. These results indicate that residual ZnO not only exhibits high reactivity but also acts as a reservoir to supply zincate anions when the subsequent reduction process occurs.

4.2.2 In situ Raman spectroscopy. The *operando* Raman spectra with 2D maps clearly show the distribution of chemical bonds. *In situ* Raman spectroscopy was carried out to demonstrate the excellent cycling stability of the $Zn@ZnF_2//V_2O_5$ cell.[200] The peaks at 279, 403, 475, 520, 694, and 991 cm^{-1} correspond to the active material (V_2O_5), as shown in Fig. 15e. All these peaks were observed during cycling and without additional peaks, suggesting that the crystal structure of V_2O_5 remained after zinc-ion insertion/extraction. Thus, the V_2O_5 cathode with the anode of $Zn@ZnF_2$ maintains high reversibility and stability upon cycling, revealing that the transport kinetics of Zn^{2+} ions are effectively regulated after the electrodeposition of the ZnF_2 matrix on the Zn anode. In addition, the two peaks at 694 and 991 cm^{-1} blueshift during the discharge process. This may be associated with intercalated zinc ions, which affect the vibrational bands. The reversible structural evolution of V_2O_5 was further demonstrated because all peaks returned to their original positions after charging, confirming the excellent stability of the $Zn@ZnF_2//V_2O_5$ cell.

Operando Raman spectroscopy was applied to investigate the chemical composition of the cathode during cycling. As displayed in Fig. 15f, the 2D map of the *operando* Raman spectra
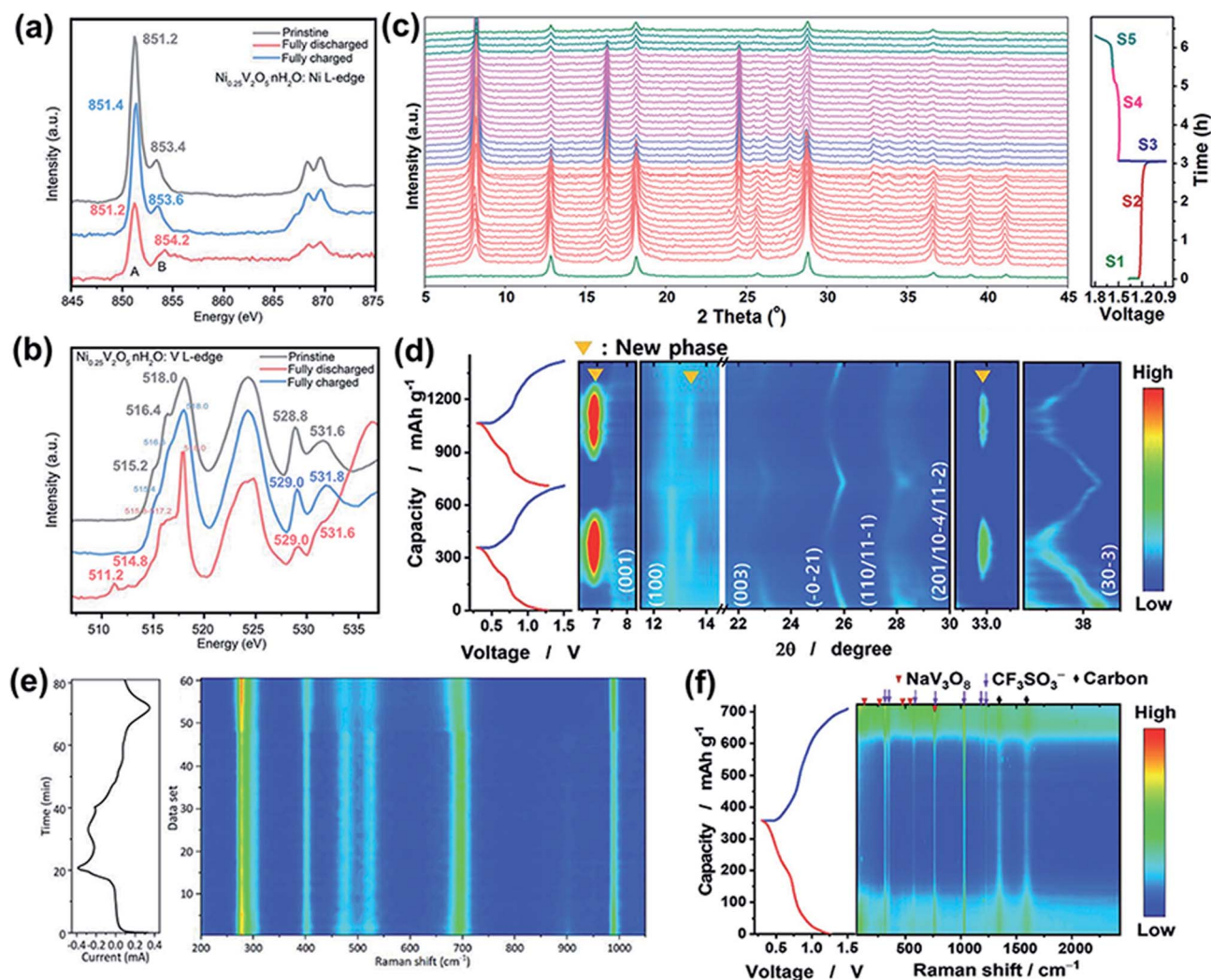
This journal is © The Royal Society of Chemistry 2021

J. Mater. Chem. A, 2021, **9**, 19245–19281 | **19273**

Fig. 15 (a) Ni and (b) V L-edge NEXAFS spectra of fresh, 20th cycle discharged and 20th cycle charged $Ni_{0.25}V_2O_5 \cdot nH_2O$. Reproduced with permission.[189] Copyright 2020, Wiley. (c) *In situ* XRD patterns of the α-MnO_2 membrane cathode and corresponding discharge/charge profile during the initial cycle. Reproduced with permission.[197] Copyright 2020, Wiley. (d) *Operando*-SXRD results of NaV_3O_8 during two cycles. Reproduced with permission.[198] Copyright 2020, Wiley. (e) *In situ* Raman spectra of the V_2O_5 cathode cycled with the Zn@ZnF_2 electrode as an anode. Reproduced with permission.[200] Copyright 2021, Wiley. (f) 2D map of the *operando* Raman spectra of the NaV_3O_8-based cathode material in 1 M $Zn(CF_3SO_3)_2$ solutions. Reproduced with permission.[198] Copyright 2020, Wiley.

presents the Raman shifts of NaV_3O_8 during cycling.[198] There were five peaks below 800 cm^{-1}, which originated from the NaV_3O_8 active material. In addition, the Raman spectra also show the signals of the triflate ($CF_3SO_3^-$) anion. The peaks of NaV_3O_8 decrease during discharge and disappear below 0.8 V. The signals appear over 0.8 V in the charged state. The disappearance of the NaV_3O_8 active material signal is related to the generation of a new phase $(Zn_5(OH)_8(CF_3SO_3)_2 \cdot xH_2O)$ on the cathode surface, which prevents the cathode surface from being exposed to the incident light.

4.3 Visualization techniques for morphology characterization

Visualization techniques are powerful techniques for monitoring the growth of Zn dendrites and the morphology evolution

of cathodes clearly and vividly, which is of great value for obtaining an in-depth insight into the reaction mechanisms. Morphology characterization techniques, such as TEM, SEM, X-ray microcomputed tomography (CT), and optical microscopy, present the morphology evolution of the cathode and anode in various dimensions and scales.

TEM is an essential tool to characterize active materials at the nanometer scale and even at the atomic scale. It can be applied to distinguish the crystalline or amorphous phases of electrodes by the lattice fringe and diffraction rings of selected area electron diffraction (SAED). Another generally used application in aqueous cathodes is to confirm the structure and phase evolution, such as the lattice spacing, defects, and coated layers. The SEM image shows a lower spatial resolution than TEM, but it provides the surface morphology at a larger scale
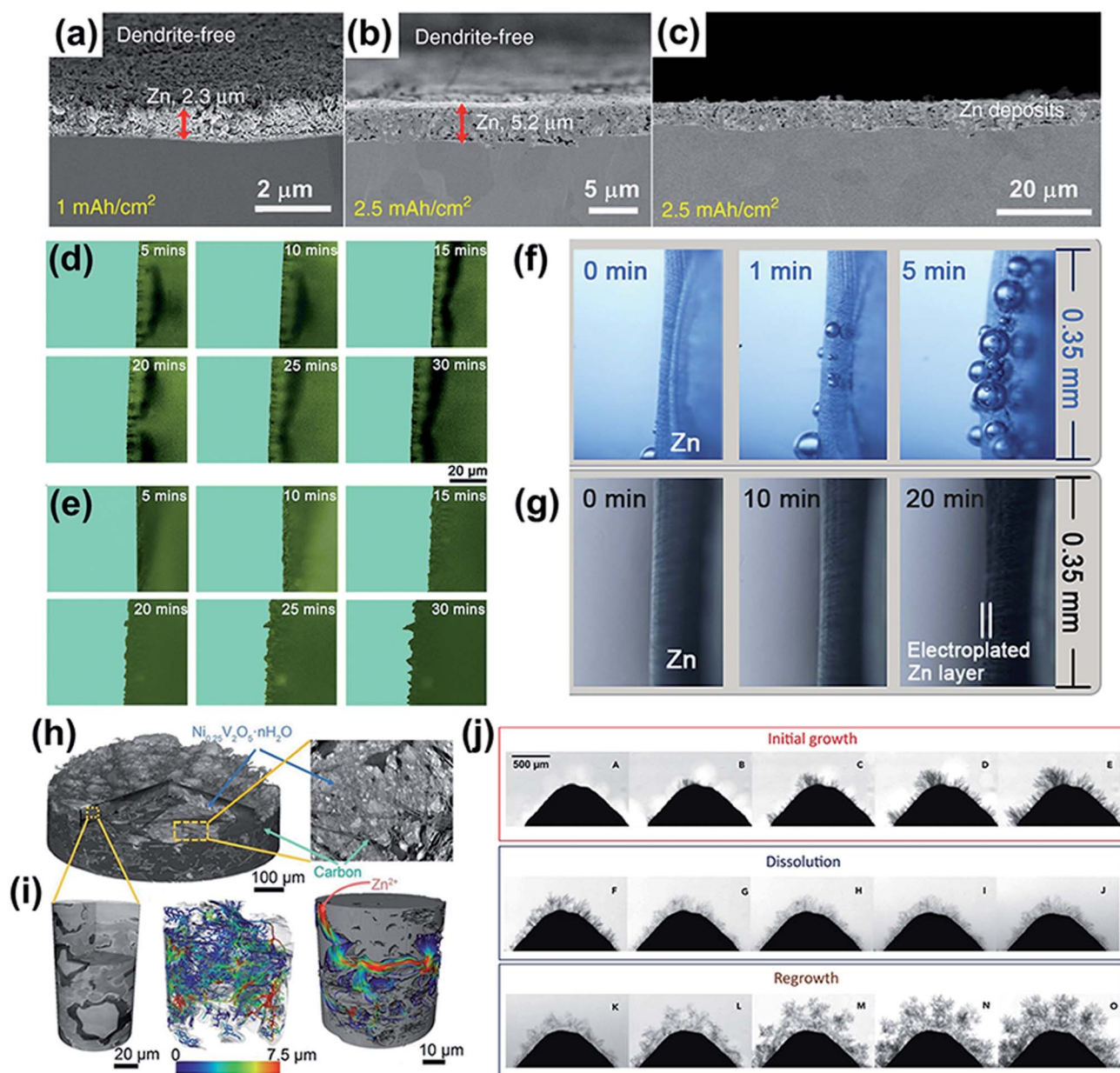
19274 | *J. Mater. Chem. A*, 2021, **9**, 19245–19281

This journal is © The Royal Society of Chemistry 2021

Fig. 16 Cross-sectional SEM images of Zn deposits which were obtained in a Zn(TFSI)$_2$-based eutectic solvent with 1 mA h cm^{-2} (0.25 mA cm^{-2}) (a) and 2.5 mA h cm^{-2} (0.5 mA cm^{-2}) (b) Zn on a Zn substrate, respectively. (c) A lower-magnification image of panel (b) showing a large area of uniform deposition.[201] Cross-sectional Zn deposition morphology on (d) a coated Zn plate in a symmetrical Zn cell at a current density of 10 mA cm^{-2} obtained using an *in situ* optical microscope and (e) a bare Zn plate. Reproduced with permission.[149] Copyright 2019, Royal Society of Chemistry. *In situ* optical microscopy images of the Zn electrodeposition process in (f) 0.5 M LiTFSI + 0.5 M Zn(TFSI)$_2$ and (g) water-in-deep eutectic solvent at 0.2 mA cm^{-2}. Reproduced with permission.[202] Copyright 2018, Elsevier. (h) 3D volume rendering of the reconstructed electrode obtained by X-ray micro-CT of the fabricated Ni$_{0.25}$V$_2$O$_5$·nH$_2$O electrode. (i) 3D volume rendering of the electrode reconstructed by X-ray nano-CT. (h and i) Reproduced with permission.[189] Copyright 2020, Wiley. (j) Zinc dendrite growth. Reproduced with permission.[203] Copyright 2018, Elsevier.

than TEM. The morphology evolution of the cathode during cycling was investigated by using SEM images to further understand the reaction process. In addition, it was also applied to monitor the morphology evolution and thickness of Zn dendrites during the zinc ion deposition and dissolution process (Fig. 16a–c).[201]

4.3.1 *Operando* optical microscopy. Optical microscopy is easy to operate and can be applied *in situ* to present the evolution of the morphology at the micrometer scale. For instance, PA has been reported as a protective layer coating on Zn anodes to realize high reversibility and inhibit dendrite formation.[149] *Operando* optical microscopy was used to observe the Zn plating/stripping process to investigate the influence of PA on

This journal is © The Royal Society of Chemistry 2021

J. Mater. Chem. A, 2021, **9**, 19245–19281 | **19275**

the evolution of Zn dendrites. As displayed in Fig. 16d, Zn dendrites did not appear on the coated anode surface during the plating process for 30 min and the anode maintained a smooth surface. However, the Zn anode without the PA layer showed obvious dendrites after 15 min of deposition (Fig. 16e).

In addition to monitoring the Zn dendrites, *operando* optical microscopy was also used to observe gas evolution during the Zn corrosion reaction. The "water-in-deep eutectic solvent (water-in-DES)" electrolyte was reported as an efficient strategy to keep the Zn anode stable and reversible.[202] Furthermore, *operando* optical microscopy was used to observe the H_2 generation. Apparently, bubbles were generated on the anode surface of the metallic Zn in a dilute aqueous electrolyte (0.5 M LiTFSI + 0.5 M $Zn(TFSI)_2$), as shown in Fig. 16f. In contrast, no bubbles were produced on the metallic Zn surface even after 20 min at 0.2 mA cm^{-2} in a water-in-DES electrolyte (Fig. 16g), suggesting that the reactivity to water was effectively inhibited in the eutectic solvent electrolyte.

4.3.2 X-ray microscopy. X-ray microscopy is another powerful technique with a high spatial resolution to study the microstructures of anode/cathode materials. For instance, X-ray micro-CT was performed to analyze the 3D morphology of $Ni_{0.25}V_2O_5 \cdot nH_2O$ cathode materials during zinc-ion insertion/extraction.[189] The $Ni_{0.25}V_2O_5 \cdot nH_2O$ active materials were coated on hydrophilic carbon paper to observe the 3D morphology, as shown in Fig. 16h. To provide a finer structure of the electrode, a higher resolution nano-CT was conducted (Fig. 16i) to show the 3D structure of the electrode and pore size distribution. In addition, the streamlines of the diffusion flux were simulated and the electrode possesses a porosity of 0.18 and a tortuosity factor of 2.57, endowing the cathode with an effective diffusion coefficient of 0.07.

In addition to cathode materials, X-ray microscopy has also been successfully applied to investigate the dendrite evolution of zinc anodes. For example, the growth, dissolution and regrowth of Zn dendrites were observed by synchrotron X-ray computed tomography (SXCT).[203] As shown in Fig. 16j, dendrites were generated on the tip of the Zn anode after deposition for 214 s at a negative current density of 30 mA cm^{-2} and covered the anode surface as continuous deposition. After a period of deposition, new dendrites gradually grew on the primary dendrites, forming secondary dendrites and ternary dendrites. The process of Zn dendrite dissolution was also recorded in radiographic mode. The dendrites became thin and dissolved from the ternary dendrites to the primary dendrites, which is in contrast to the formation of dendrites. After 15 min of dissolution, the branches of the dendrites became thin and were retained on the tip of the Zn anode. In the subsequent regrowth process, the newly generated dendrites were connected with the dendrites formed in the first cycle, generating a dense and tortuous 3D region. Additionally, new dendrites would not be generated on the tip of the Zn anode due to the hindrance of the denser network. Thus, the tortuous dendrite networks on the zinc metal surface gradually increased after each cycle, finally leading to the degradation and failure of the battery. Visual analyses of Zn dendrite formation and dissolution provide a dynamic understanding of dendrite behavior.

5. Conclusions and prospects

Aqueous ZIBs have been deemed an alternative candidate for large-scale applications because of their low cost, inherent safety, and environmental friendliness. However, the further development and application of ZIBs are notably obstructed by many severe problems, such as their poor electronic conductivity, sluggish kinetics, structural collapse, active material dissolution, the irreversible phase transition of the cathode, the formation of Zn dendrites and the water-induced side reactions of Zn anodes. From the above analysis, structural and defect engineering strategies open a feasible and efficient avenue to handle the abovementioned problems. In this review, various structural and defect engineering strategies for the cathode materials and zinc anodes of aqueous ZIBs are systematically summarized. Nonetheless, the development of aqueous ZIBs is still in the infancy stage and many fundamental issues need to be urgently settled to satisfy future industrial applications.

First, most of the reported cathodes were fabricated with a low areal mass loading (approximately 1–2 mg cm^{-2}).[48,66] The specific capacity of the cathode cannot match well with that of Zn anodes. It is essential for the practical ZIBs to develop cathodes with a high loading to realize cell-level energy and power density. However, a higher mass loading may lead to a lower specific capacity because not all active materials participate in electrochemical reactions. Thus, to realize their practical application, designing cathodes with a high loading and excellent electrochemical performance should be considered. The energy density is another key factor to meet the demand for practical applications. Taking vanadium oxide as an example, it dominates other kinds of cathodes in capacity, but its operating voltage (usually below 1 V) needs to be further improved. The introduction of extra redox pairs such as Mn^{4+}/Mn^{3+}/Mn^{2+} into the VO framework might be feasible for improving the voltage. Additionally, the voltage can be further increased *via* the inductive effect from polyanions such as SO_4^{2-} and PO_4^{3-}. To improve the rate performance and long-term cycling of cathodes, they need to be composited with conductive materials to boost electron transport. Designing a conductive network both internally and externally is necessary for active materials. In addition, the dissolution of the cathode in aqueous electrolytes is the main reason for capacity fade, which seriously restricts the practical application of ZIBs. Surface coating is a common strategy to avoid direct contact with electrolytes, but the influence of the coated protective layer on the ion diffusion, electron transport and wettability should be considered. Carbon-based materials have been successfully used as coating layers. In terms of graphene, research on methods to realize uniform and whole coatings on active materials is limited. Moreover, considerable attention should be focused on the stability of the protective layer on the cathode upon cycling.

Second, structural and defect engineering has been rationally proposed to modulate the electrochemical properties of cathode materials. Defects have been demonstrated to be successfully introduced into the cathode structure and play

19276 | *J. Mater. Chem. A*, 2021, **9**, 19245–19281

This journal is © The Royal Society of Chemistry 2021

a positive role in optimizing the electrochemical performance. However, whether defects still stably exist in the structure during cycling is unknown; furthermore, it's worth exploring the optimal concentration of defects in the structure for zinc-ion storage. Thus, *in situ* characterization techniques are necessary to synthetically reveal the evolution of the cathode structure with defects during long-term cycling and investigate the relationship between defect concentrations and electrochemical performance. Besides, the structural stability of cathode materials needs to be further investigated. The irreversible phase transition and side reactions that occur during cycling lead to damaged structures and poor electrochemical performance. Some electronegative functional groups can be considered to modify the cathode surface. Due to the repulsive force between functional groups and OH^-, the gathering of OH^- around the interface between the cathode and electrolyte is inhibited. Therefore, the design of an interfacial modification appears to be a rational strategy to alleviate the phase transition arising from the reaction of the cathode and OH^-. Additionally, it is still necessary to analyze the mechanisms for the phase transition and side reactions and design practical cathodes with high performance for aqueous ZIBs.

Third, the types, concentrations, pH values and additives of electrolytes play a decisive role in realizing aqueous ZIBs with high performance. The capacity of the battery rapidly decays in a $ZnSO_4$ electrolyte but remains relatively stable in a much more expensive $Zn(CF_3SO_3)_2$ electrolyte. The different electrolytes are closely related to the dissolution of active materials, occurrence of side reactions, and growth of Zn dendrites. Thus, optimizing electrolyte compatibility should be given more attention. Besides, to realize the practical application of ZIBs, it is necessary to exploit an electrolyte with an affordable price and wide stability window when triggering the high operating voltage of the cathode. Considering the application environment, the aqueous zinc ion battery should operate well at low temperatures. Thus, it is of great significance to develop a novel electrolyte and electrolyte additive that is beneficial for the ionic conductivity of electrolytes at low temperatures.

Fourth, the DOD of the Zn anode reveals the percentage of the Zn anode that takes part in the actual reaction, which is highly associated with the cost and energy density of practical ZIBs. However, most of the current research has ignored this important parameter. Thus, the DOD of the Zn anode should be considered in follow-up studies. Additionally, most aqueous electrolytes are mildly acidic solutions and the corrosion of Zn anodes is inevitable. Therefore, more effort should be devoted to fundamental research to clarify the factors that affect Zn corrosion in aqueous electrolytes. In addition, analyzing the evolution process of the anode interface plays a vital role in completely solving the dendrite problem. Thus, advanced characterization techniques, such as *operando*/*in situ* XRD, FTIR spectroscopy, Raman spectroscopy, XPS, and XAFS, should be further adopted to investigate the evolution process. Besides, the remaining challenge of increasing the working life to satisfy the demands of applications before battery failure needs additional work. The mechanism is not well understood, especially after the battery is enlarged to the cell level. There is

a significant difference between laboratory studies and commercial products. Therefore, more research needs to be accomplished from laboratory studies using coin-type batteries to commercial-sized products.

Conflicts of interest

There are no conflicts to declare.

Acknowledgements

References

1 Y. Liang, H. Dong, D. Aurbach and Y. Yao, *Nat. Energy*, 2020, **5**, 646–656.

2 J. Ming, J. Guo, C. Xia, W. Wang and H. N. Alshareef, *Mater. Sci. Eng., R*, 2019, **135**, 58–84.

3 L. Zhang, Y. Pan, Y. Chen, M. Li, P. Liu, C. Wang, P. Wang and H. Lu, *Chem. Commun.*, 2019, **55**, 4258–4261.

4 O. Ellabban, H. Abu-Rub and F. Blaabjerg, *Renewable Sustainable Energy Rev.*, 2014, **39**, 748–764.

5 D. Lin, Y. Liu and Y. Cui, *Nat. Nanotechnol.*, 2017, **12**, 194–206.

6 D. Larcher and J. M. Tarascon, *Nat. Chem.*, 2015, **7**, 19–29.

7 J. Hao, X. Li, X. Zeng, D. Li, J. Mao and Z. Guo, *Energy Environ. Sci.*, 2020, **13**, 3917–3949.

8 L. E. Blanc, D. Kundu and L. F. Nazar, *Joule*, 2020, **4**, 771–799.

9 P. He, Q. Chen, M. Yan, X. Xu, L. Zhou, L. Mai and C.-W. Nan, *EnergyChem*, 2019, **1**, 100022.

10 T. Wang, C. Li, X. Xie, B. Lu, Z. He, S. Liang and J. Zhou, *ACS Nano*, 2020, **14**, 16321–16347.

11 M. Armand and J. M. Tarascon, *Nature*, 2008, **451**, 652–657.

12 V. Etacheri, R. Marom, R. Elazari, G. Salitra and D. Aurbach, *Energy Environ. Sci.*, 2011, **4**, 3243–3262.

13 J. M. Tarascon and M. Armand, *Nature*, 2001, **414**, 359–367.

14 S. Huang, J. Zhu, J. Tian and Z. Niu, *Chem.–Eur. J.*, 2019, **25**, 14480–14494.

15 M. Rashad, M. Asif, Y. Wang, Z. He and I. Ahmed, *Energy Storage Mater.*, 2020, **25**, 342–375.

16 C. Xu, B. Li, H. Du and F. Kang, *Angew. Chem., Int. Ed.*, 2012, **51**, 933–935.

17 M.-C. Lin, M. Gong, B. Lu, Y. Wu, D.-Y. Wang, M. Guan, M. Angell, C. Chen, J. Yang, B.-J. Hwang and H. Dai, *Nature*, 2015, **520**, 324–328.

18 M. Mao, T. Gao, S. Hou and C. Wang, *Chem. Soc. Rev.*, 2018, **47**, 8804–8841.

This journal is © The Royal Society of Chemistry 2021

J. Mater. Chem. A, 2021, **9**, 19245–19281 | **19277**

19 B. Tang, L. Shan, S. Liang and J. Zhou, *Energy Environ. Sci.*, 2019, **12**, 3288–3304.

20 E. Hu and X.-Q. Yang, *Nat. Mater.*, 2018, **17**, 480–481.

21 K. Wang, P. Pei, Z. Ma, H. Chen, H. Xu, D. Chen and X. Wang, *J. Mater. Chem. A*, 2015, **3**, 22648–22655.

22 W. Lu, C. Xie, H. Zhang and X. Li, *ChemSusChem*, 2018, **11**, 3996–4006.

23 L. Chen, Y. Ruan, G. Zhang, Q. Wei, Y. Jiang, T. Xiong, P. He, W. Yang, M. Yan, Q. An and L. Mai, *Chem. Mater.*, 2019, **31**, 699–706.

24 J. Li, K. McColl, X. Lu, S. Sathasivam, H. Dong, L. Kang, Z. Li, S. Zhao, A. G. Kafizas, R. Wang, D. J. L. Brett, P. R. Shearing, F. Corà, G. He, C. J. Carmalt and I. P. Parkin, *Adv. Energy Mater.*, 2020, **10**, 2000058.

25 T. Liu, X. Cheng, H. Yu, H. Zhu, N. Peng, R. Zheng, J. Zhang, M. Shui, Y. Cui and J. Shu, *Energy Storage Mater.*, 2019, **18**, 68–91.

26 N. Zhang, F. Cheng, Y. Liu, Q. Zhao, K. Lei, C. Chen, X. Liu and J. Chen, *J. Am. Chem. Soc.*, 2016, **138**, 12894–12901.

27 Q. Yang, Q. Li, Z. Liu, D. Wang, Y. Guo, X. Li, Y. Tang, H. Li, B. Dong and C. Zhi, *Adv. Mater.*, 2020, **32**, 2001854.

28 W. Ling, P. Wang, Z. Chen, H. Wang, J. Wang, Z. Ji, J. Fei, Z. Ma, N. He and Y. Huang, *ChemElectroChem*, 2020, **7**, 2957–2978.

29 T. C. Li, D. Fang, J. Zhang, M. E. Pam, Z. Y. Leong, J. Yu, X. L. Li, D. Yan and H. Y. Yang, *J. Mater. Chem. A*, 2021, **9**, 6013–6028.

30 G. Fang, J. Zhou, A. Pan and S. Liang, *ACS Energy Lett.*, 2018, **3**, 2480–2501.

31 H. Li, L. Ma, C. Han, Z. Wang, Z. Liu, Z. Tang and C. Zhi, *Nano Energy*, 2019, **62**, 550–587.

32 Y. Yang, Y. Tang, G. Fang, L. Shan, J. Guo, W. Zhang, C. Wang, L. Wang, J. Zhou and S. Liang, *Energy Environ. Sci.*, 2018, **11**, 3157–3162.

33 P. He, G. Zhang, X. Liao, M. Yan, X. Xu, Q. An, J. Liu and L. Mai, *Adv. Energy Mater.*, 2018, **8**, 1702463.

34 B. Tang, G. Fang, J. Zhou, L. Wang, Y. Lei, C. Wang, T. Lin, Y. Tang and S. Liang, *Nano Energy*, 2018, **51**, 579–587.

35 F. Ming, H. Liang, Y. Lei, S. Kandambeth, M. Eddaoudi and H. N. Alshareef, *ACS Energy Lett.*, 2018, **3**, 2602–2609.

36 C. Xia, J. Guo, P. Li, X. Zhang and H. N. Alshareef, *Angew. Chem., Int. Ed.*, 2018, **57**, 3943–3948.

37 X. Wang, B. Xi, X. Ma, Z. Feng, Y. Jia, J. Feng, Y. Qian and S. Xiong, *Nano Lett.*, 2020, **20**, 2899–2906.

38 D. Kundu, B. D. Adams, V. Duffort, S. H. Vajargah and L. F. Nazar, *Nat. Energy*, 2016, **1**, 16119.

39 Y. Yang, Y. Tang, S. Liang, Z. Wu, G. Fang, X. Cao, C. Wang, T. Lin, A. Pan and J. Zhou, *Nano Energy*, 2019, **61**, 617–625.

40 J. Zheng, C. Liu, M. Tian, X. Jia, E. P. Jahrman, G. T. Seidler, S. Zhang, Y. Liu, Y. Zhang, C. Meng and G. Cao, *Nano Energy*, 2020, **70**, 104519.

41 W. Dong, M. Du, F. Zhang, X. Zhang, Z. Miao, H. Li, Y. Sang, J. J. Wang, H. Liu and S. Wang, *ACS Appl. Mater. Interfaces*, 2021, **13**, 5034–5043.

42 F. Zhang, X. Sun, M. Du, X. Zhang, W. Dong, Y. Sang, J. Wang, Y. Li, H. Liu and S. Wang, *Energy Environ. Mater.*, 2020, DOI: 10.1002/eem2.12145.

43 S. Guo, G. Fang, S. Liang, M. Chen, X. Wu and J. Zhou, *Acta Mater.*, 2019, **180**, 51–59.

44 J. He, X. Liu, H. Zhang, Z. Yang, X. Shi, Q. Liu and X. Lu, *ChemSusChem*, 2020, **13**, 1568–1574.

45 L. Wang and J. Zheng, *Mater. Today Adv.*, 2020, **7**, 100078.

46 N. Zhang, Y. Dong, M. Jia, X. Bian, Y. Wang, M. Qiu, J. Xu, Y. Liu, L. Jiao and F. Cheng, *ACS Energy Lett.*, 2018, **3**, 1366–1372.

47 M. Yan, P. He, Y. Chen, S. Wang, Q. Wei, K. Zhao, X. Xu, Q. An, Y. Shuang, Y. Shao, K. T. Mueller, L. Mai, J. Liu and J. Yang, *Adv. Mater.*, 2018, **30**, 1703725.

48 Z. Yao, Q. Wu, K. Chen, J. Liu and C. Li, *Energy Environ. Sci.*, 2020, **13**, 3149–3163.

49 V. Verma, S. Kumar, W. Manalastas, J. Zhao, R. Chua, S. Meng, P. Kidkhunthod and M. Srinivasan, *ACS Appl. Energy Mater.*, 2019, **2**, 8667–8674.

50 S. Lian, C. Sun, W. Xu, W. Huo, Y. Luo, K. Zhao, G. Yao, W. Xu, Y. Zhang, Z. Li, K. Yu, H. Zhao, H. Cheng, J. Zhang and L. Mai, *Nano Energy*, 2019, **62**, 79–84.

51 Q. Pang, C. Sun, Y. Yu, K. Zhao, Z. Zhang, P. M. Voyles, G. Chen, Y. Wei and X. Wang, *Adv. Energy Mater.*, 2018, **8**, 1800144.

52 W. Zhang, C. Zuo, C. Tang, W. Tang, B. Lan, X. Fu, S. Dong and P. Luo, *Energy Technol.*, 2021, **9**, 2000789.

53 L. Chen, Q. An and L. Mai, *Adv. Mater. Interfaces*, 2019, **6**, 1900387.

54 F. Wan, L. Zhang, X. Dai, X. Wang, Z. Niu and J. Chen, *Nat. Commun.*, 2018, **9**, 1656.

55 Y.-R. Luo, *Comprehensive Handbook of Chemical Bond Energies*, CRC Press, 2007.

56 M. Du, F. Zhang, X. Zhang, W. Dong, Y. Sang, J. Wang, H. Liu and S. Wang, *Sci. China: Chem.*, 2020, **63**, 1767–1776.

57 H. Geng, M. Cheng, B. Wang, Y. Yang, Y. Zhang and C. C. Li, *Adv. Funct. Mater.*, 2019, **30**, 1907684.

58 L. Ma, N. Li, C. Long, B. Dong, D. Fang, Z. Liu, Y. Zhao, X. Li, J. Fan, S. Chen, S. Zhang and C. Zhi, *Adv. Funct. Mater.*, 2019, **29**, 1906142.

59 Q. Li, X. Rui, D. Chen, Y. Feng, N. Xiao, L. Gan, Q. Zhang, Y. Yu and S. Huang, *Nano-Micro Lett.*, 2020, **12**, 67.

60 C. Wei, C. Xu, B. Li, H. Du and F. Kang, *J. Phys. Chem. Solids*, 2012, **73**, 1487–1491.

61 C. Zhu, G. Fang, J. Zhou, J. Guo, Z. Wang, C. Wang, J. Li, Y. Tang and S. Liang, *J. Mater. Chem. A*, 2018, **6**, 9677–9683.

62 B. Jiang, C. Xu, C. Wu, L. Dong, J. Li and F. Kang, *Electrochim. Acta*, 2017, **229**, 422–428.

63 H. Pan, Y. Shao, P. Yan, Y. Cheng, K. S. Han, Z. Nie, C. Wang, J. Yang, X. Li, P. Bhattacharya, K. T. Mueller and J. Liu, *Nat. Energy*, 2016, **1**, 16039.

64 C. Guo, H. Liu, J. Li, Z. Hou, J. Liang, J. Zhou, Y. Zhu and Y. Qian, *Electrochim. Acta*, 2019, **304**, 370–377.

65 J. Wang, J.-G. Wang, H. Liu, C. Wei and F. Kang, *J. Mater. Chem. A*, 2019, **7**, 13727–13735.

66 T. Sun, Q. Nian, S. Zheng, J. Shi and Z. Tao, *Small*, 2020, **16**, 2000597.

67 G. G. Yadav, J. W. Gallaway, D. E. Turney, M. Nyce, J. Huang, X. Wei and S. Banerjee, *Nat. Commun.*, 2017, **8**, 14424.

68 G. Fang, C. Zhu, M. Chen, J. Zhou, B. Tang, X. Cao, X. Zheng, A. Pan and S. Liang, *Adv. Funct. Mater.*, 2019, **29**, 1808375.

69 C. Liu, Z. Neale, J. Zheng, X. Jia, J. Huang, M. Yan, M. Tian, M. Wang, J. Yang and G. Cao, *Energy Environ. Sci.*, 2019, **12**, 2273–2285.

70 J. Ji, H. Wan, B. Zhang, C. Wang, Y. Gan, Q. Tan, N. Wang, J. Yao, Z. Zheng, P. Liang, J. Zhang, H. Wang, L. Tao, Y. Wang, D. Chao and H. Wang, *Adv. Energy Mater.*, 2020, **11**, 2003203.

71 Z. Peng, Q. Wei, S. Tan, P. He, W. Luo, Q. An and L. Mai, *Chem. Commun.*, 2018, **54**, 4041–4044.

72 J. Shin, D. S. Choi, H. J. Lee, Y. Jung and J. W. Choi, *Adv. Energy Mater.*, 2019, **9**, 1900083.

73 X. Yang, W. Deng, M. Chen, Y. Wang and C. F. Sun, *Adv. Mater.*, 2020, **32**, 2003592.

74 K. W. Nam, H. Kim, J. H. Choi and J. W. Choi, *Energy Environ. Sci.*, 2019, **12**, 1999–2009.

75 H. Liu, J.-G. Wang, W. Hua, Z. You, Z. Hou, J. Yang, C. Wei and F. Kang, *Energy Storage Mater.*, 2021, **35**, 731–738.

76 D. Wang, L. Wang, G. Liang, H. Li, Z. Liu, Z. Tang, J. Liang and C. Zhi, *ACS Nano*, 2019, **13**, 10643–10652.

77 B. Tang, J. Zhou, G. Fang, F. Liu, C. Zhu, C. Wang, A. Pan and S. Liang, *J. Mater. Chem. A*, 2019, **7**, 940–945.

78 K. Zhu, T. Wu and K. Huang, *ACS Nano*, 2019, **13**, 14447–14458.

79 S. Liu, H. Zhu, B. Zhang, G. Li, H. Zhu, Y. Ren, H. Geng, Y. Yang, Q. Liu and C. C. Li, *Adv. Mater.*, 2020, **32**, 2001113.

80 J. Huang, Z. Wang, M. Hou, X. Dong, Y. Liu, Y. Wang and Y. Xia, *Nat. Commun.*, 2018, **9**, 2906.

81 K. Zhu, T. Wu and K. Huang, *Adv. Energy Mater.*, 2019, **9**, 1901968.

82 M. Du, C. Liu, F. Zhang, W. Dong, X. Zhang, Y. Sang, J. J. Wang, Y. G. Guo, H. Liu and S. Wang, *Adv. Sci.*, 2020, **7**, 2000083.

83 D. Bin, W. Huo, Y. Yuan, J. Huang, Y. Liu, Y. Zhang, F. Dong, Y. Wang and Y. Xia, *Chem*, 2020, **6**, 968–984.

84 Y. Zhang, L. Tao, C. Xie, D. Wang, Y. Zou, R. Chen, Y. Wang, C. Jia and S. Wang, *Adv. Mater.*, 2020, **32**, 1905923.

85 T. Xiong, Y. Zhang, W. S. V. Lee and J. Xue, *Adv. Energy Mater.*, 2020, **10**, 2001769.

86 Y. Zhang, J. Xu, Y. Long, L. Tao, M. Ding and C. Jia, *ChemNanoMat*, 2020, **6**, 1589–1600.

87 W. Zhang, Y. Xiao, C. Zuo, W. Tang, G. Liu, S. Wang, W. Cai, S. Dong and P. Luo, *ChemSusChem*, 2021, **14**, 971–978.

88 Z. W. J. Ang, T. Xiong, W. S. V. Lee and J. Xue, *ChemNanoMat*, 2020, **6**, 1357–1364.

89 H. Zhang, J. Wang, Q. Liu, W. He, Z. Lai, X. Zhang, M. Yu, Y. Tong and X. Lu, *Energy Storage Mater.*, 2019, **21**, 154–161.

90 Y. Zeng, Z. Lai, Y. Han, H. Zhang, S. Xie and X. Lu, *Adv. Mater.*, 2018, **30**, 1802396.

91 Y. Zhang, S. Deng, M. Luo, G. Pan, Y. Zeng, X. Lu, C. Ai, Q. Liu, Q. Xiong, X. Wang, X. Xia and J. Tu, *Small*, 2019, **15**, 1905452.

92 W. Xu, C. Sun, K. Zhao, X. Cheng, S. Rawal, Y. Xu and Y. Wang, *Energy Storage Mater.*, 2019, **16**, 527–534.

93 J. Li, N. Luo, F. Wan, S. Zhao, Z. Li, W. Li, J. Guo, P. R. Shearing, D. J. L. Brett, C. J. Carmalt, G. Chai, G. He and I. P. Parkin, *Nanoscale*, 2020, **12**, 20638–20648.

94 T. He, S. Weng, Y. Ye, J. Cheng, X. Wang, X. Wang and B. Wang, *Energy Storage Mater.*, 2021, **38**, 389–396.

95 N. Zhang, F. Cheng, Y. Liu, Q. Zhao, K. Lei, C. Chen, X. Liu and J. Chen, *J. Am. Chem. Soc.*, 2016, **138**, 12894–12901.

96 C. Zhu, G. Fang, S. Liang, Z. Chen, Z. Wang, J. Ma, H. Wang, B. Tang, X. Zheng and J. Zhou, *Energy Storage Mater.*, 2020, **24**, 394–401.

97 J. Ding, Z. Du, B. Li, L. Wang, S. Wang, Y. Gong and S. Yang, *Adv. Mater.*, 2019, **31**, 1904369.

98 M. Liao, J. Wang, L. Ye, H. Sun, Y. Wen, C. Wang, X. Sun, B. Wang and H. Peng, *Angew. Chem., Int. Ed.*, 2020, **59**, 2273–2278.

99 Z. Li, Y. Ren, L. Mo, C. Liu, K. Hsu, Y. Ding, X. Zhang, X. Li, L. Hu, D. Ji and G. Cao, *ACS Nano*, 2020, **14**, 5581–5589.

100 M. Han, J. Huang, S. Liang, L. Shan, X. Xie, Z. Yi, Y. Wang, S. Guo and J. Zhou, *iScience*, 2020, **23**, 100797.

101 W. Yang, L. Dong, W. Yang, C. Xu, G. Shao and G. Wang, *Small Methods*, 2019, **4**, 1900670.

102 T. Xiong, Z. G. Yu, H. Wu, Y. Du, Q. Xie, J. Chen, Y. W. Zhang, S. J. Pennycook, W. S. V. Lee and J. Xue, *Adv. Energy Mater.*, 2019, **9**, 1803815.

103 H. Liang, Z. Cao, F. Ming, W. Zhang, D. H. Anjum, Y. Cui, L. Cavallo and H. N. Alshareef, *Nano Lett.*, 2019, **19**, 3199–3206.

104 L. Shan, Y. Yang, W. Zhang, H. Chen, G. Fang, J. Zhou and S. Liang, *Energy Storage Mater.*, 2019, **18**, 10–14.

105 L. Qian, T. Wei, K. Ma, G. Yang and C. Wang, *ACS Appl. Mater. Interfaces*, 2019, **11**, 20888–20894.

106 Y. Cai, R. Chua, S. Huang, H. Ren and M. Srinivasan, *Chem. Eng. J.*, 2020, **396**, 125221.

107 X. Wang, Y. Li, S. Wang, F. Zhou, P. Das, C. Sun, S. Zheng and Z. S. Wu, *Adv. Energy Mater.*, 2020, **10**, 2000081.

108 S. Deng, Z. Yuan, Z. Tie, C. Wang, L. Song and Z. Niu, *Angew. Chem., Int. Ed.*, 2020, **59**, 22002–22006.

109 Y. Luo, L. Wei, H. Geng, Y. Zhang, Y. Yang and C. C. Li, *ACS Appl. Mater. Interfaces*, 2020, **12**, 11753–11760.

110 M. Song, H. Tan, D. Chao and H. J. Fan, *Adv. Funct. Mater.*, 2018, **28**, 1802564.

111 N. Zhang, F. Cheng, J. Liu, L. Wang, X. Long, X. Liu, F. Li and J. Chen, *Nat. Commun.*, 2017, **8**, 405.

112 S. Li, Y. Liu, X. Zhao, Q. Shen, W. Zhao, Q. Tan, N. Zhang, P. Li, L. Jiao and X. Qu, *Adv. Mater.*, 2021, **33**, 2007480.

113 J. Long, F. Yang, J. Cuan, J. Wu, Z. Yang, H. Jiang, R. Song, W. Song, J. Mao and Z. Guo, *ACS Appl. Mater. Interfaces*, 2020, **12**, 32526–32535.

114 D. Yu, Z. Wei, X. Zhang, Y. Zeng, C. Wang, G. Chen, Z. X. Shen and F. Du, *Adv. Funct. Mater.*, 2020, **31**, 2008743.

115 X. Wang, Y. Li, P. Das, S. Zheng, F. Zhou and Z.-S. Wu, *Energy Storage Mater.*, 2020, **31**, 156–163.

116 C. Liu, M. Tian, M. Wang, J. Zheng, S. Wang, M. Yan, Z. Wang, Z. Yin, J. Yang and G. Cao, *J. Mater. Chem. A*, 2020, **8**, 7713–7723.

This journal is © The Royal Society of Chemistry 2021

J. Mater. Chem. A, 2021, **9**, 19245–19281 | **19279**

117 Y. Fu, Q. Wei, G. Zhang, X. Wang, J. Zhang, Y. Hu, D. Wang, L. Zuin, T. Zhou, Y. Wu and S. Sun, *Adv. Energy Mater.*, 2018, **8**, 1801445.

118 Q.-L. Gao, D.-S. Li, X.-M. Liu, Y.-F. Wang, W.-L. Liu, M.-M. Ren, F.-G. Kong, S.-J. Wang and R.-C. Zhou, *Electrochim. Acta*, 2020, **335**, 135642.

119 X. Xiao, H. Zhang, W. Wu, C. Wang, S. Wu, G. Zhong, K. Xu, J. Zeng, W. Su and X. Lu, *Part. Part. Syst. Charact.*, 2019, **36**, 1900183.

120 H. Jiang, Y. Zhang, L. Xu, Z. Gao, J. Zheng, Q. Wang, C. Meng and J. Wang, *Chem. Eng. J.*, 2020, **382**, 122844.

121 S. Wang, S. Zhang, X. Chen, G. Yuan, B. Wang, J. Bai, H. Wang and G. Wang, *J. Colloid Interface Sci.*, 2020, **580**, 528–539.

122 H. Zhang, Z. Yao, D. Lan, Y. Liu, L. Ma and J. Cui, *J. Alloys Compd.*, 2021, **861**, 158560.

123 F. Tang, T. He, H. Zhang, X. Wu, Y. Li, F. Long, Y. Xiang, L. Zhu, J. Wu and X. Wu, *J. Electroanal. Chem.*, 2020, **873**, 114368.

124 M. Sun, D. S. Li, Y. F. Wang, W. L. Liu, M. M. Ren, F. G. Kong, S. J. Wang, Y. Z. Guo and Y. M. Liu, *ChemElectroChem*, 2019, **6**, 2510–2516.

125 G. Xu, X. Liu, S. Huang, L. Li, X. Wei, J. Cao, L. Yang and P. K. Chu, *ACS Appl. Mater. Interfaces*, 2020, **12**, 706–716.

126 B. Wu, G. Zhang, M. Yan, T. Xiong, P. He, L. He, X. Xu and L. Mai, *Small*, 2018, **14**, 1703850.

127 H. Luo, B. Wang, C. Wang, F. Wu, F. Jin, B. Cong, Y. Ning, Y. Zhou, D. Wang, H. Liu and S. Dou, *Energy Storage Mater.*, 2020, **33**, 390–398.

128 X. Dai, F. Wan, L. Zhang, H. Cao and Z. Niu, *Energy Storage Mater.*, 2019, **17**, 143–150.

129 J. Wang, J. G. Wang, H. Liu, Z. You, Z. Li, F. Kang and B. Wei, *Adv. Funct. Mater.*, 2020, 2007397.

130 X. Pu, T. Song, L. Tang, Y. Tao, T. Cao, Q. Xu, H. Liu, Y. Wang and Y. Xia, *J. Power Sources*, 2019, **437**, 226917.

131 S. Guo, S. Liang, B. Zhang, G. Fang, D. Ma and J. Zhou, *ACS Nano*, 2019, **13**, 13456–13464.

132 T. Zhai, L. Wan, S. Sun, Q. Chen, J. Sun, Q. Xia and H. Xia, *Adv. Mater.*, 2017, **29**, 1604167.

133 Y. Shen, Z. Li, Z. Cui, K. Zhang, R. Zou, F. Yang and K. Xu, *J. Mater. Chem. A*, 2020, **8**, 21044–21052.

134 Y. Liu, J. Wang, Y. Zeng, J. Liu, X. Liu and X. Lu, *Small*, 2020, **16**, 1907458.

135 B. Yong, D. Ma, Y. Wang, H. Mi, C. He and P. Zhang, *Adv. Energy Mater.*, 2020, **10**, 2002354.

136 Q. Zhao, X. Huang, M. Zhou, Z. Ju, X. Sun, Y. Sun, Z. Huang, H. Li and T. Ma, *ACS Appl. Mater. Interfaces*, 2020, **12**, 36072–36081.

137 J. Huang, J. Tu, Y. Lv, Y. Liu, H. Huang, L. Li and J. Yao, *Synth. Met.*, 2020, **266**, 116438.

138 J. Huang, X. Tang, K. Liu, G. Fang, Z. He and Z. Li, *Mater. Today Energy*, 2020, **17**, 100475.

139 X. Yue, H. Liu and P. Liu, *Chem. Commun.*, 2019, **55**, 1647–1650.

140 N. Wang, T. Xin, Y. Zhao, Q. Li, M. Hu and J. Liu, *ACS Sustainable Chem. Eng.*, 2019, **7**, 14195–14202.

141 D. Xu, H. Wang, F. Li, Z. Guan, R. Wang, B. He, Y. Gong and X. Hu, *Adv. Mater. Interfaces*, 2019, **6**, 1801506.

142 Y. Zhao, L. Ma, Y. Zhu, P. Qin, H. Li, F. Mo, D. Wang, G. Liang, Q. Yang, W. Liu and C. Zhi, *ACS Nano*, 2019, **13**, 7270–7280.

143 Y. Q. Jin, H. Chen, L. Peng, Z. Chen, L. Cheng, J. Song, H. Zhang, J. Chen, F. Xie, Y. Jin, J. Shi and H. Meng, *Chem. Eng. J.*, 2020, **416**, 127704.

144 X. Zhang, J. Li, H. Ao, D. Liu, L. Shi, C. Wang, Y. Zhu and Y. Qian, *Energy Storage Mater.*, 2020, **30**, 337–345.

145 M. E. Pam, D. Yan, J. Yu, D. Fang, L. Guo, X. L. Li, T. C. Li, X. Lu, L. K. Ang, R. Amal, Z. Han and H. Y. Yang, *Adv. Sci.*, 2021, **8**, 2002722.

146 S. Liu, L. Kang, J. M. Kim, Y. T. Chun, J. Zhang and S. C. Jun, *Adv. Energy Mater.*, 2020, **10**, 2000477.

147 B. Yong, D. Ma, Y. Wang, H. Mi, C. He and P. Zhang, *Adv. Energy Mater.*, 2020, **10**, 2002354.

148 Q. Yang, G. Liang, Y. Guo, Z. Liu, B. Yan, D. Wang, Z. Huang, X. Li, J. Fan and C. Zhi, *Adv. Mater.*, 2019, **31**, 1903778.

149 Z. Zhao, J. Zhao, Z. Hu, J. Li, J. Li, Y. Zhang, C. Wang and G. Cui, *Energy Environ. Sci.*, 2019, **12**, 1938–1949.

150 L. Ma, M. A. Schroeder, O. Borodin, T. P. Pollard, M. S. Ding, C. Wang and K. Xu, *Nat. Energy*, 2020, **5**, 743–749.

151 D. Han, S. Wu, S. Zhang, Y. Deng, C. Cui, L. Zhang, Y. Long, H. Li, Y. Tao, Z. Weng, Q.-H. Yang and F. Kang, *Small*, 2020, **16**, 2001736.

152 R. Woods, R. H. Yoon and C. A. Young, *Int. J. Miner. Process.*, 1987, **20**, 109–120.

153 B. Beverskog and I. Puigdomenech, *Corros. Sci.*, 1997, **39**, 107–114.

154 Q. Zhang, J. Luan, L. Fu, S. Wu, Y. Tang, X. Ji and H. Wang, *Angew. Chem., Int. Ed.*, 2019, **58**, 15841–15847.

155 M. Cui, Y. Xiao, L. Kang, W. Du, Y. Gao, X. Sun, Y. Zhou, X. Li, H. Li, F. Jiang and C. Zhi, *ACS Appl. Energy Mater.*, 2019, **2**, 6490–6496.

156 C. Shen, X. Li, N. Li, K. Xie, J.-g. Wang, X. Liu and B. Wei, *ACS Appl. Mater. Interfaces*, 2018, **10**, 25446–25453.

157 W. Li, K. Wang, M. Zhou, H. Zhan, S. Cheng and K. Jiang, *ACS Appl. Mater. Interfaces*, 2018, **10**, 22059–22066.

158 N. Zhang, S. Huang, Z. Yuan, J. Zhu, Z. Zhao and Z. Niu, *Angew. Chem., Int. Ed.*, 2021, **60**, 2861–2865.

159 X. Zhang, J. Li, D. Liu, M. Liu, T. Zhou, K. Qi, L. Shi, Y. Zhu and Y. Qian, *Energy Environ. Sci.*, 2021, **14**, 3120–3129.

160 A. Xia, X. Pu, Y. Tao, H. Liu and Y. Wang, *Appl. Surf. Sci.*, 2019, **481**, 852–859.

161 Z. Li, Z. Wu, S. Dong, T. Xu, S. Li, Y. An, J. Jiang and X. Zhang, *Adv. Funct. Mater.*, 2021, **31**, 2006495.

162 L. Kang, M. Cui, F. Jiang, Y. Gao, H. Luo, J. Liu, W. Liang and C. Zhi, *Adv. Energy Mater.*, 2018, **8**, 1801090.

163 Q. Zhang, J. Luan, X. Huang, Q. Wang, D. Sun, Y. Tang, X. Ji and H. Wang, *Nat. Commun.*, 2020, **11**, 3961.

164 P. Liang, J. Yi, X. Liu, K. Wu, Z. Wang, J. Cui, Y. Liu, Y. Wang, Y. Xia and J. Zhang, *Adv. Funct. Mater.*, 2020, **30**, 1908528.

19280 | *J. Mater. Chem. A*, 2021, **9**, 19245–19281

This journal is © The Royal Society of Chemistry 2021

165 X. Xie, S. Liang, J. Gao, S. Guo, J. Guo, C. Wang, G. Xu, X. Wu, G. Chen and J. Zhou, *Energy Environ. Sci.*, 2020, **13**, 503–510.

166 L. Ma, Q. Li, Y. Ying, F. Ma, S. Chen, Y. Li, H. Huang and C. Zhi, *Adv. Mater.*, 2021, **33**, 2007406.

167 J. Hao, B. Li, X. Li, X. Zeng, S. Zhang, F. Yang, S. Liu, D. Li, C. Wu and Z. Guo, *Adv. Mater.*, 2020, **32**, 2003021.

168 J. Hao, X. Li, S. Zhang, F. Yang, X. Zeng, S. Zhang, G. Bo, C. Wang and Z. Guo, *Adv. Funct. Mater.*, 2020, **30**, 2001263.

169 P. Chen, X. Yuan, Y. Xia, Y. Zhang, L. Fu, L. Liu, N. Yu, Q. Huang, B. Wang, X. Hu, Y. Wu and T. van Ree, *Adv. Sci.*, 2021, **8**, 2100309.

170 Y. Cui, Q. Zhao, X. Wu, X. Chen, J. Yang, Y. Wang, R. Qin, S. Ding, Y. Song, J. Wu, K. Yang, Z. Wang, Z. Mei, Z. Song, H. Wu, Z. Jiang, G. Qian, L. Yang and F. Pan, *Angew. Chem., Int. Ed.*, 2020, **59**, 16594–16601.

171 J. F. Parker, C. N. Chervin, I. R. Pala, M. Machler, M. F. Burz, J. W. Long and D. R. Rolison, *Science*, 2017, **356**, 415–418.

172 X. Shi, G. Xu, S. Liang, C. Li, S. Guo, X. Xie, X. Ma and J. Zhou, *ACS Sustainable Chem. Eng.*, 2019, **7**, 17737–17746.

173 Z. Kang, C. Wu, L. Dong, W. Liu, J. Mou, J. Zhang, Z. Chang, B. Jiang, G. Wang, F. Kang and C. Xu, *ACS Sustainable Chem. Eng.*, 2019, **7**, 3364–3371.

174 Y. Zeng, X. Zhang, R. Qin, X. Liu, P. Fang, D. Zheng, Y. Tong and X. Lu, *Adv. Mater.*, 2019, **31**, 1903675.

175 D. Chao, C. Zhu, M. Song, P. Liang, X. Zhang, N. H. Tiep, H. Zhao, J. Wang, R. Wang, H. Zhang and H. J. Fan, *Adv. Mater.*, 2018, **30**, 1803181.

176 Z. Wang, J. Huang, Z. Guo, X. Dong, Y. Liu, Y. Wang and Y. Xia, *Joule*, 2019, **3**, 1289–1300.

177 Y. Yin, S. Wang, Q. Zhang, Y. Song, N. Chang, Y. Pan, H. Zhang and X. Li, *Adv. Mater.*, 2020, **32**, 1906803.

178 V. Chakarova, T. Boiadjieva-Scherzer, D. Kovacheva, H. Kronberger and M. Monev, *Corros. Sci.*, 2018, **140**, 73–78.

179 Z. Liu, T. Cui, G. Pulletikurthi, A. Lahiri, T. Carstens, M. Olschewski and F. Endres, *Angew. Chem., Int. Ed.*, 2016, **55**, 2889–2893.

180 M. Yano, S. Fujitani, K. Nishio, Y. Akai and M. Kurimura, *J. Power Sources*, 1998, **74**, 129–134.

181 C. W. Lee, S. W. Eom, K. Sathiyanarayanan and M. S. Yun, *Electrochim. Acta*, 2006, **52**, 1588–1591.

182 S. Fashu, C. D. Gu, J. L. Zhang, W. Q. Bai, X. L. Wang and J. P. Tu, *Surf. Interface Anal.*, 2015, **47**, 403–412.

183 Z. Cai, Y. Ou, J. Wang, R. Xiao, L. Fu, Z. Yuan, R. Zhan and Y. Sun, *Energy Storage Mater.*, 2020, **27**, 205–211.

184 S.-B. Wang, Q. Ran, R.-Q. Yao, H. Shi, Z. Wen, M. Zhao, X.-Y. Lang and Q. Jiang, *Nat. Commun.*, 2020, **11**, 1634.

185 F. Wan, L. Zhang, X. Dai, X. Wang, Z. Niu and J. Chen, *Nat. Commun.*, 2018, **9**, 1656.

186 W. Xu, K. Zhao, W. Huo, Y. Wang, G. Yao, X. Gu, H. Cheng, L. Mai, C. Hu and X. Wang, *Nano Energy*, 2019, **62**, 275–281.

187 R. Qin, Y. Wang, M. Zhang, Y. Wang, S. Ding, A. Song, H. Yi, L. Yang, Y. Song, Y. Cui, J. Liu, Z. Wang, S. Li, Q. Zhao and F. Pan, *Nano Energy*, 2021, **80**, 105478.

188 X. Zeng, J. Mao, J. Hao, J. Liu, S. Liu, Z. Wang, Y. Wang, S. Zhang, T. Zheng, J. Liu, P. Rao and Z. Guo, *Adv. Mater.*, 2021, **33**, 2007416.

189 J. Li, K. McColl, X. Lu, S. Sathasivam, H. Dong, L. Kang, Z. Li, S. Zhao, A. G. Kafizas, R. Wang, D. J. L. Brett, P. R. Shearing, F. Corà, G. He, C. J. Carmalt and I. P. Parkin, *Adv. Energy Mater.*, 2020, **10**, 2000058.

190 Y. Dong, L. Miao, G. Ma, S. Di, Y. Wang, L. Wang, J. Xu and N. Zhang, *Chem. Sci.*, 2021, **12**, 5843–5852.

191 L. Cao, D. Li, E. Hu, J. Xu, T. Deng, L. Ma, Y. Wang, X.-Q. Yang and C. Wang, *J. Am. Chem. Soc.*, 2020, **142**, 21404–21409.

192 F. Wang, O. Borodin, T. Gao, X. Fan, W. Sun, F. Han, A. Faraone, J. A. Dura, K. Xu and C. Wang, *Nat. Mater.*, 2018, **17**, 543–549.

193 C. Zhang, J. Holoubek, X. Wu, A. Daniyar, L. Zhu, C. Chen, D. P. Leonard, I. A. Rodríguez-Pérez, J.-X. Jiang, C. Fang and X. Ji, *Chem. Commun.*, 2018, **54**, 14097–14099.

194 H. Yang, Z. Chang, Y. Qiao, H. Deng, X. Mu, P. He and H. Zhou, *Angew. Chem., Int. Ed.*, 2020, **59**, 9377–9381.

195 R. Xiao, Z. Cai, R. Zhan, J. Wang, Y. Ou, Z. Yuan, L. Wang, Z. Lu and Y. Sun, *Chem. Eng. J.*, 2021, **420**, 129642.

196 Á. Muñoz-Noval, K. Fukami, A. Koyama, T. Kuruma, A. Kitada, K. Murase, T. Abe, T. Sakka and S. Hayakawa, *J. Phys. Chem. C*, 2017, **121**, 18047–18056.

197 X. Gao, H. Wu, W. Li, Y. Tian, Y. Zhang, H. Wu, L. Yang, G. Zou, H. Hou and X. Ji, *Small*, 2020, **16**, 1905842.

198 J. H. Jo, Y. Aniskevich, J. Kim, J. U. Choi, H. J. Kim, Y. H. Jung, D. Ahn, T. Y. Jeon, K. S. Lee, S. H. Song, H. Kim, G. Ragoisha, A. Mazanik, E. Streltsov and S. T. Myung, *Adv. Energy Mater.*, 2020, **10**, 2001595.

199 A. Nakata, H. Murayama, K. Fukuda, T. Yamane, H. Arai, T. Hirai, Y. Uchimoto, J.-i. Yamaki and Z. Ogumi, *Electrochim. Acta*, 2015, **166**, 82–87.

200 Y. Yang, C. Liu, Z. Lv, H. Yang, Y. Zhang, M. Ye, L. Chen, J. Zhao and C. C. Li, *Adv. Mater.*, 2021, 2007388.

201 H. Qiu, X. Du, J. Zhao, Y. Wang, J. Ju, Z. Chen, Z. Hu, D. Yan, X. Zhou and G. Cui, *Nat. Commun.*, 2019, **10**, 5374.

202 J. Zhao, J. Zhang, W. Yang, B. Chen, Z. Zhao, H. Qiu, S. Dong, X. Zhou, G. Cui and L. Chen, *Nano Energy*, 2019, **57**, 625–634.

203 V. Yufit, F. Tariq, D. S. Eastwood, M. Biton, B. Wu, P. D. Lee and N. P. Brandon, *Joule*, 2019, **3**, 485–502.

This journal is © The Royal Society of Chemistry 2021

J. Mater. Chem. A, 2021, **9**, 19245–19281 | **19281**